PASSIVE RADAR ON MOVING PLATFORMS EXPLOITING DVB-T TRANSMITTERS OF OPPORTUNITY

by

Philipp Maximilian Wojaczek

A thesis submitted in partial fulfilment of the requirements for the degree of Doctor of Philosophy in Information and Communication Engineering

at

Sapienza University of Rome

February 2019

Cycle XXXI

Author .....

Department of Information Engineering, Electronics and Telecommunications

Certified by .....

Pierfrancesco Lombardo
Professor
Thesis Supervisor

This thesis was evaluated by the two following external referees:

Maria Pilar Jarabo Amores, Professor, University of Alcalá, Madrid, Spain

Chris Baker, Professor, University of Birmingham, Birmingham, United Kingdom

The time and effort of the external referees in evaluating this thesis, as well as their valuable and constructive suggestions, are very much appreciated and greatly acknowledged.

Abstract

The work, effort, and research put into passive radar for stationary receivers have shown significant developments and progress in recent years.
The next challenge is mounting a passive radar on moving platforms for the purpose of target detection and ground imaging, e.g. for covert border control. A passive radar on a moving platform has many advantages and offers many benefits, however there is also a considerable drawback that has limited its application so far. Due to the movement the clutter returns are spread in Doppler and may overlap moving targets, which are then difficult to detect. While this problem is common for an active radar as well, with a passive radar a further problem arises: It is impossible to control the exploited time-varying waveform emitted from a telecommunication transmitter. A conventional processing approach is ineffective as the time-varying waveform leads to residuals all over the processed data. Therefore a dedicated clutter cancellation method, e.g. the displaced phase centre antenna (DPCA) approach, does not have the ability to completely remove the clutter, so that target detection is considerably limited.
The aim must be therefore to overcome this limitation by exploiting a processing technique, which is able to remove these residuals in order to cope with the clutter returns thus making target detection feasible.
The findings of this research and thesis show that a reciprocal filtering based stage is able to provide a time-invariant impulse response similar to the transmissions of an active radar. Due to this benefit it is possible to achieve an overall complete clutter removal together with a dedicated DPCA stage, so that moving target detection is considerably improved, making it possible in the first place. Based on mathematical analysis and on simulations it is proven, that by exploiting this processing in principle an infinite clutter cancellation can be achieved. This result shows that the reciprocal filter is an essential processing stage. Applications on real data acquired from two different measurement campaigns prove these results. By the proposed approach, the limiting factor (i.e. the time-varying waveform) for target detection is negotiated, and in principle any clutter cancellation technique known from active radar can be applied. Therefore this analysis and the results provide a substantial contribution to the passive radar research community and enables it to address the next questions.

Acknowledgements

The following papers were published as a result of this PhD research:

P. Wojaczek and D. Cristallini, "Optimal trajectories for range resolution improvement in multi-PCL SAR," AEU – International Journal of Electronics and Communications, vol. 73, pp. 173 – 182, 2017.

P. Wojaczek, F. Colone, D. Cristallini, P. Lombardo and H. Kuschel, "The application of the reciprocal filter and DPCA for GMTI in DVB-T - PCL," International Conference on Radar Systems (Radar 2017), Belfast, 2017, pp. 1-5. doi: 10.1049/cp.2017.0478

P. Wojaczek, A. Summers and D. Cristallini, "Preliminary experimental results of STAP for passive radar on a moving platform," 2018 22nd International Microwave and Radar Conference (MIKON), Poznan, 2018, pp. 589-592. doi: 10.23919/MIKON.2018.8405294

P. Wojaczek and D. Cristallini, "The Influence of Channel Errors in Mobile Passive Radar using DVB-T Illuminators of Opportunity," 2018 19th International Radar Symposium (IRS), Bonn, 2018, pp. 1-10. doi: 10.23919/IRS.2018.8447912

P. Wojaczek, A. Summers, D. Cristallini, I. Walterscheid, P. Lombardo, and F. Colone, "Results of airborne PCL under CCI conditions using DVB-T illuminators of opportunity," in International Conference on Radar (Radar2018), Aug 2018.

P. Wojaczek, F. Colone, D. Cristallini and P. Lombardo, "Reciprocal Filter-based STAP for Passive Radar on moving platforms," in IEEE Transactions on Aerospace and Electronic Systems. doi: 10.1109/TAES.2018.2867688

To following publications was contributed during this PhD research:

C. Underwood, M. Cherniakov, M. Antoniou, M. Gashinova, A. Stove, S. Hristov, G. Atkinson, H. Kuschel, P. Wojaczek, and D. Cristallini, "PASSAT: Passive imaging radar constellation for near-persistent earth observation," in 68th International Astronautical Congress (IAC), Sep 2017, pp. 1–11.

The results described in
I. Walterscheid, P. Wojaczek, D. Cristallini and A. Summers, "Challenges and first results of an airborne passive SAR experiment using a DVB-T transmitter," EUSAR 2018; 12th European Conference on Synthetic Aperture Radar, Aachen, Germany, 2018, pp. 1-4.
were presented as a poster and have won the Best Poster Award at the conference.

M. Antoniou, A. G. Stove, H. Ma, H. Kuschel, D. Cristallini, P. Wojaczek, C. I. Underwood, A. Moccia, A. Renga, G. Fasano, and M. Cherniakov, to be published: "Passive SAR satellite constellation for near-persistent earth observation: Prospective and issues," in IEEE Aerospace and Electronics Systems Magazine, 2018.

Contents

List of Figures

List of Tables

Nomenclature

B_W	Bandwidth of the transmitted signal [Hz]
B_L	Baseline = Distance between receiver and transmitter [m]
β	Bistatic angle
c_0	Speed of light: $c_0 = 3 \cdot 10^8\,\mathrm{m/s}$
Δ_R	Bistatic range resolution [m]
H_R	Altitude of receiver [m]
N_S	Number of pulses in one coherent processing interval
N_A	Number of antenna elements
N_{CP}	Number of clutter patches
N_{RC}	Number of range cells
N_G	Number of targets
f_T	Transmit/carrier frequency [Hz]
f_S	Sampling frequency [Hz]
$\lambda_T = c_0/f_T$	Wavelength of centre frequency of one DVB-T channel [m]
R_R	Range from target to receiver [m]
R_T	Range from target to transmitter [m]
R_B	Bistatic range [m]
ρ_T	Angle between velocity vector of receiver and direction to transmitter
ρ_G	Angle between velocity vector of receiver and direction to scatterer/target
γ_T	Angle between velocity vector of target and direction to transmitter
γ_G	Angle between velocity vector of target and direction to receiver
$\mathbf{G} = [x_G, y_G, z_G]^T$	Position of target [m]
$\mathbf{T} = [x_T, y_T, z_T]^T$	Position of transmitter [m]
$\mathbf{R} = [x_R, y_R, z_R]^T$	Position of receiver [m]

$\hat{\mathbf{u}}_{RG} = [\hat{u}_{RG,x}, \hat{u}_{RG,y}, \hat{u}_{RG,z}]$	Unit vector pointing from receiver to target
$\hat{\mathbf{u}}_{RT} = [\hat{u}_{RT,x}, \hat{u}_{RT,y}, \hat{u}_{RT,z}]$	Unit vector pointing from receiver to transmitter
$\hat{\mathbf{u}}_{GR} = [\hat{u}_{GR,x}, \hat{u}_{GR,y}, \hat{u}_{GR,z}]$	Unit vector pointing from target to receiver
$\hat{\mathbf{u}}_{GT} = [\hat{u}_{GT,x}, \hat{u}_{GT,y}, \hat{u}_{GT,z}]$	Unit vector pointing from target to transmitter
$\mathbf{v}_G = [v_{G,x}, v_{G,y}, v_{G,z}]^T$	Velocity vector of target [m/s]
$\mathbf{v}_R = [v_{R,x}, v_{R,y}, v_{R,z}]^T$	Velocity vector of receiver [m/s]
$v_R = \lvert\mathbf{v}_R\rvert$	Absolute value of receiver velocity [m/s]
$\mathrm{T_U}$	Duration of the useful part of one DVB-T symbol [s]
$\mathrm{T_{CP}}$	Duration of the cyclic prefix of one DVB-T symbol [s]
$\mathrm{T_S} = \mathrm{T_U} + \mathrm{T_{CP}}$	Duration of one complete DVB-T symbol [s]

Chapter 1

Introduction

1.1 Overview and Motivation

A passive radar system is a special type of bistatic radar, which does not emit any signals. Instead it uses non-cooperative broadcast or communication transmitters as Illuminator Of Opportunity (IO). As it operates covertly, its usage is very appealing for military applications, but it is also advantageous for civilian applications, due to its low cost operation, as no dedicated transmitter needs to be maintained. It is as well efficient in spectrum usage, as no dedicated spectrum needs to be allocated, therefore further reducing cost.
Passive radar for stationary applications has reached a stage of maturity in recent years, so that it can be purchased for military applications[1], but as well being employed for improved air traffic safety e.g. in the vicinity of wind parks[2].
Passive radar on moving platforms has not reached this stage of operational capability. The proof of concept of an air-borne passive radar for imaging and target detection was given, together with a number of advantages that make passive radar on moving platforms very attractive for different kind of applications. No transmitter needs to be maintained, and for the receiving system common hardware, which can be easily built and maintained, can be used. This means a reduction of weight and also a reduction in energy consumption (no dedicated transmitter is necessary). For these reasons a passive radar has great potential to be mounted on Unmanned Aerial Vehicles (UAVs) or Ultralight Aircrafts (ULAs), and makes it very appealing for covert and/or low cost monitoring operations. Furthermore it can be easily, without big effort, installed on vehicles and on boats. By doing so it is possible to monitor a large area, e.g. countrysides, coast-lines, etc. covertly, thus

[1] https://www.hensoldt.net/solutions/land/radar/passive-radar/

[2] https://www.fhr.fraunhofer.de/en/press-media/press-releases/PARASOL-receives-accreditation-from-german-air-traffic-control.html

providing security and border control by early target detection, and the passive radar system can be supportive as an early warning system for an active radar, which then focuses its operation onto the detections of the passive radar.
These advantages start from the premise that an IO is available. This dependence on an external source, is a disadvantage, as the passive radar operator needs to rely on a transmission, which is not under control of the operator, but which needs to be available at all times. However, nowadays a large number of transmitters (terrestrial or satellite-borne) are available and provide broadcast and communication transmissions to the people, therefore, provided the passive radar is flexible in selecting the available transmitters, nearly worldwide coverage can be assumed. As (terrestrial) broadcast and communication transmitters transmit usually on Very High Frequency (VHF) or Ultra High Frequency (UHF) frequencies, which have the property to travel beyond the radar horizon, it is possible, to increase with a passive radar exploiting transmissions in these frequency bandwidth the detection capability beyond the radar horizon, that is for over-the-horizon radar. Furthermore, it is said, that VHF and UHF frequencies have the capability of foliage penetration, thus increasing the potential operation possibilities, e.g. for detection of targets in forested areas.
Over the past years, digital broadcast and communication transmitters were the preferred choice as IO due to a number of advantages. They transmit with constant bandwidth, which provides a constant range resolution. Furthermore, the digital transmission format makes an almost ideal recovery of the transmitted signal possible. This is an important factor, as the knowledge of the transmitted signal is crucial for the signal processing in order for a reliable detection of targets. The choice of a digital modulated signal as illumination signal is advantageous for the passive radar, as the transmitted signal might be recovered from one (or all) of the surveillance channels, which reduces the total number of receiving channels, as a dedicated reference channel pointing to the transmitter to collect a clean transmitted signal is not necessary.
Among digital transmitters the DVB-T transmitters were one of the most employed transmitters of opportunity, which is due to a high transmit power leading to a wide coverage and monitoring capability and due to the reasonably broad bandwidth, which allows good range resolution in the sense of target localisation. Furthermore, DVB-T or at least digital television transmission formats very similar to DVB-T, are almost world-wide available. Therefore, DVB-T Transmitter (TX) were chosen as IO in this work.
Although some contributions about passive radar on moving platforms exist, a stage of maturity of a working passive radar system on moving platforms is not reached yet. That means there is great field for research and questions that need to be answered in order to make a passive radar on moving platforms for target

detection and clutter suppression possible and contribute to the maturity of the system. The focus must be especially on the exploited waveform, as the time-varying content of the waveform can severely impede the clutter suppression, but this key point has received little attention in the research for passive radar on moving platforms so far.

1.2 Goal and Aims of the Thesis

The goal of this thesis is to contribute to passive radar on mobile platforms for moving target indication by negotiating the limitations given in the signal structure in order to achieve an ideal suppression of the clutter spread in Doppler.
Specifically, the goal of this work is to address: (i) the continuous waveform that is intrinsic in the DVB-T passive radar and tends to provide a very limited dynamic range in the bistatic range-Doppler map; (ii) the spread of the signal sidelobes through the whole range-Doppler map caused by the platform motion. The effect of applying the two alternative approaches: Matched filtering and Reciprocal filtering is analysed on the capability to remove the clutter contribution via an appropriate clutter suppression technique. This is intended to identify the best processing scheme to apply passive radar moving target indication from a moving platform. To achieve this goal following aims were set:

- Analysis and understanding of the influence of the inherent signal structure on clutter suppression performance if a conventional signal processing stage is considered.
- Based on the understandings, an appropriate solution is to be provided in order to improve the clutter suppression. This includes:
  - Analysis of the achievable improvements in clutter suppression.
  - Comparing the achieved results to the conventional processing.
- Confirmation of the results by organising, planning, and conduction of measurement campaign and evaluation of the acquired data.
- Among these aims there is also the demonstration of the practical effectiveness of the Moving Target Indication technique with an appropriate experimentation. This includes addressing all the practical problems that must be solved in a practical application, among which (i) receiving channel calibration; (ii) platform motion estimation, and (iii) antenna pattern calibration need to be mentioned.

1.3 Layout of the Thesis

The layout of this thesis is as follows: In Chapter 2 the passive radar background, its geometry and nomenclature are described as well as an overview of the widely used DVB-T standard and the preprocessing employed here in this work. Furthermore an overview on existing literature and publications about passive radar in general and especially about passive radar on moving platforms is given.
Chapter 3 provides the signal model in Sec. 3.1; The problem statement is addressed in Sec. 3.2, which is analysed in detail in Sec. 3.3. The suggested solution to negotiate the described problem is provided in Sec. 3.4 of the same Chapter.
The results achieved theoretically and in simulations are verified by the evaluation of measurement data from two different trials, which are described in Chapter 4.
In Chapter 5 various techniques to further improve the detection, e.g. improved signal processing algorithms are provided and analysed.
The Chapter 6 addresses further work about limitations and achieved results, which were found during the work for this thesis.
Chapter 7 draws the conclusions, gives an insight to limitations and provides an outlook for further work.

1.4 Contributions Made by this Thesis

This work has contributed to the passive radar community with (insert number) key contributions, as there are:

1. A mathematical analysis of the impact of the widely used matched filter for range compression on clutter suppression.

2. A mathematical analysis of the advantage using the reciprocal filter for range compression in lieu of the matched filter and subsequent clutter suppression.

3. Verification of the results by simulated data and evaluation of real data.

4. Development of signal processing algorithms in order to re-establish the DPCA condition for real environments.

5. Development of signal processing algorithms in order to perform a digital calibration for improved clutter suppression.

6. Demonstration of the phenomenon of co-channel-interference by means of real data for the first time; additionally an algorithm to reduce the co-channel interference is presented.

7. Technique to improve the range resolution with multiple receivers.

Parts of this work were published as journal articles [1] and [2], and in conference papers [3], [4], [5] and in [6]. Furthermore it was contributed to research on passive radar in following publications: [7], [8]. The results described in [9] were presented as a poster at the 12th European Conference on Synthetic Aperture Radar (EuSAR 2018) in Aachen, Germany, which has won the Best Poster Award.

Chapter 2

Background

This chapter focuses on the theory of Passive Bistatic Radar and provides the necessary theoretical background to this work.

2.1 Passive Bistatic Radar

The term Passive Coherent Location (PCL) or Passive (Bistatic) Radar defines a type of radar, which does not emit any signals on its own, i.e. it does not have a dedicated radar transmitter under its control [10]. Instead the Receiver (RX) makes use of electromagnetic waves, which are emitted by commercial broadcast and/or communication transmitters.
A TX which is dual-used (or hijacked) by a PCL system, is called "Illuminator Of Opportunity (IO)".

2.1.1 Geometry of a bistatic (passive) radar

The geometry of a bistatic radar is characterized by the displacement of the RX and the TX.

Fig. 2.1 shows the drawing of a bistatic radar, with the transmitter $T = [x_T, y_T, z_T]^\dagger$, the receiver $R = [x_R, y_R, z_R]^\dagger$, and the target $G = [x_G, y_G, z_G]^\dagger$[1]. The velocity vectors of the target and of the receiver are defined by $\mathbf{v}_G = [v_{Gx}, v_{Gy}, v_{Gz}]^\dagger$ and $\mathbf{v}_R = [v_{Rx}, v_{Ry}, v_{Rz}]^\dagger$. $\hat{\mathbf{u}}_{RG}, \hat{\mathbf{u}}_{RT}, \hat{\mathbf{u}}_{GR}, \hat{\mathbf{u}}_{GT}$ define Line Of Sight (LOS) unit vec-

[1]The subscript "†" indicates the transposed operation.

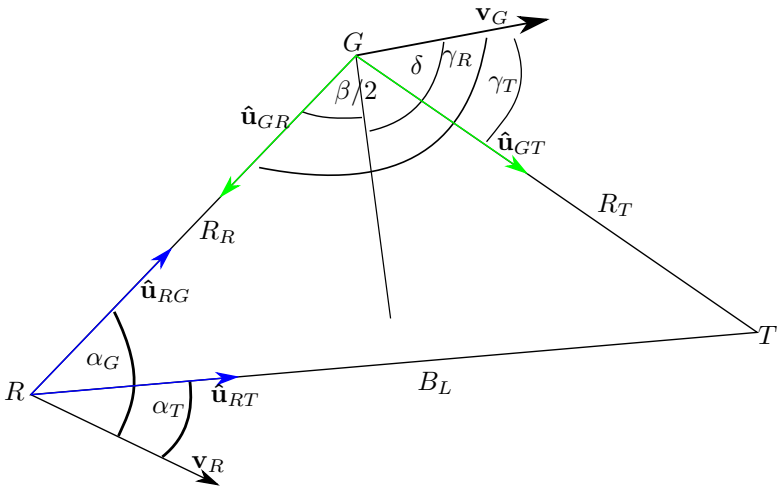

Fig. 2.1: Bistatic geometry.

tors pointing from receiver/target to target/receiver and transmitter, where:

$$
\begin{aligned}
|\hat{\mathbf{u}}_{RG}| &= 1 \\
|\hat{\mathbf{u}}_{RT}| &= 1 \\
|\hat{\mathbf{u}}_{GR}| &= 1 \\
|\hat{\mathbf{u}}_{GT}| &= 1
\end{aligned}
$$

The angles α_T, α_G and γ_R, γ_T define the angles between the receiver's/target's direction of velocity and the vector pointing towards target/receiver and TX, i.e.:

$$
\begin{aligned}
\cos\alpha_G &= \frac{\hat{\mathbf{u}}_{RG}\mathbf{v}_R}{|\hat{\mathbf{u}}_{RG}||\mathbf{v}_R|} = \frac{\hat{\mathbf{u}}_{RG}\mathbf{v}_R}{|\mathbf{v}_R|} \\
\cos\alpha_T &= \frac{\hat{\mathbf{u}}_{RT}\mathbf{v}_R}{|\hat{\mathbf{u}}_{RT}||\mathbf{v}_R|} = \frac{\hat{\mathbf{u}}_{RT}\mathbf{v}_R}{|\mathbf{v}_R|} \\
\cos\gamma_R &= \frac{\hat{\mathbf{u}}_{GR}\mathbf{v}_G}{|\hat{\mathbf{u}}_{GR}||\mathbf{v}_G|} = \frac{\hat{\mathbf{u}}_{GR}\mathbf{v}_G}{|\mathbf{v}_G|} \\
\cos\gamma_T &= \frac{\hat{\mathbf{u}}_{GT}\mathbf{v}_G}{|\hat{\mathbf{u}}_{GT}||\mathbf{v}_G|} = \frac{\hat{\mathbf{u}}_{GT}\mathbf{v}_G}{|\mathbf{v}_G|}
\end{aligned}
$$

δ defines the angle between $\mathbf{v}_G$ and the bistatic bisector $\beta/2$, where β defines the bistatic angle between the directions from target to RX and TX.
The values R_R, R_T, and B_L define the range from target to RX and from target to TX, and the baseline, which is the range from TX to RX.

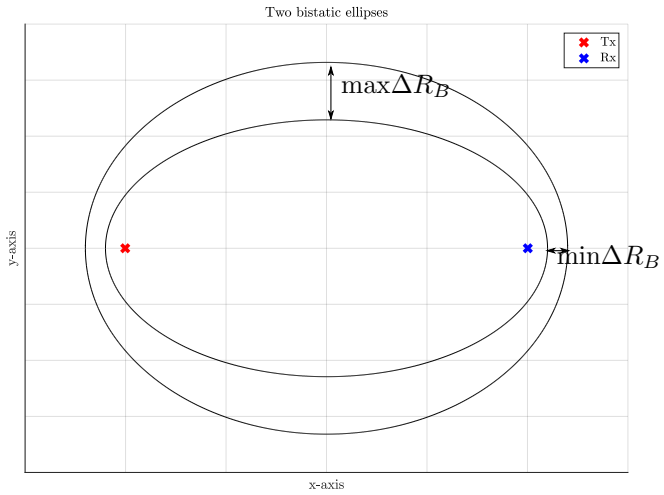

Fig. 2.2: Bistatic ellipses with the positions of TX and RX as focal points.

2.1.2 Range and Doppler relationships

Bistatic range Using the definitions of Sec. 2.1.1, the bistatic range R_B can be defined, which is the distance resulting in a time difference of arrival between the direct signal and the delayed echo from the target both received at the RX:

$$R_B = R_T + R_R - B_L \tag{2.1}$$

Isorange ellipsoid and isorange ellipse In a bistatic system the target is located on an ellipsoid, which is usually called isorange ellipsoid. Neglecting the altitude of TX, RX, and target, the intersection of the isorange ellipsoid with the plane of TX, RX, and target, results in an ellipse, where $R_T + R_R = 2a$ with a defining the semi major axis of the ellipse. Usually this ellipse is called isorange ellipse. This is shown in Fig. 2.2, where two isorange ellipses are plotted with TX and RX in the focal points. The separation between two bistatic ellipses is defined as bistatic range cell ΔR_B which can be approximated by [11]:

$$\Delta R_B = \frac{c_0}{2\cos(\beta/2) \cdot B_W} \tag{2.2}$$

c_0 and B_W define speed of light and the bandwidth of the exploited signal. The width of the bistatic range cell defines the minimum separation which is necessary to differentiate between the returns of two point scatterers, which is called the range resolution. Unlike to a monostatic (active) radar, the range cell's width is dependent on the bistatic angle β with its maximum value for $x = 0$ and its

minimum value for $y = 0$. In the best case, the range resolution would be equal to the range resolution, which occurs for $\beta = 0$.

Doppler of point-like scatterer The bistatic Doppler-shift of a point-like scatterer is given as [11]:

$$\begin{aligned} f_D(\alpha, \gamma) &= f_T\Big(\frac{v_R}{c_0}\cos\alpha_G + \frac{v_G}{c_0}\cos\gamma_R + \frac{v_G}{c_0}\cos\gamma_T\Big) \\ &= f_T\Big(\frac{v_R}{c_0}\cos\alpha_G + \frac{v_G}{c_0}\cos\delta\cos\beta/2\Big) \end{aligned} \tag{2.3}$$

f_T defines the centre frequency of the signal emitted from the TX. In case the point-like scatterer is a non-moving object, i.e. $v_G = 0$, (2.3) would reduce to:

$$f_D(\phi) = \frac{v_R}{c_0} f_T \cos\phi_G \tag{2.4}$$

SFN and MFN A cluster of transmitters, spatially distributed in a closed region is usually referred to as Single Frequency Network (SFN). Each TX from the SFN is transmitting the same content on the same frequency f_T. Directly adjacent SFNs transmit on different frequencies, but availability of frequency bandwidth is limited, so a used frequency will be reused again in the next but one SFN. This type of transmitter network holds for the DVB-T transmission in Germany, Norway, Poland, etc.
However, it is as well possible, that the transmitters are not grouped into an SFN, but each TX emits the signal on a different frequency. This kind of transmission is referred to as Multi-frequency Network (MFN), and holds for the DVB-T transmission e.g. in Australia.

2.2 DVB-T as Illuminator of opportunity

Basically each broadcast or communication TX can serve as IO, e.g. DVB-T, Digital Audio Broadcasting (DAB), FM radio stations, and communication signals such as Global System For Mobile Communications (GSM), WiFi, or Long-Term Evolution (LTE).
This work focuses on PCL systems exploiting Orthogonal Frequency-division Multiplexing (OFDM) transmitters of opportunity, and without loss of generality with a focus on DVB-T transmitters. OFDM is a technique, to transmit a signal using multiple so-called carrier frequencies, in which all of the carriers are orthogonal to each other. In this way, a wider bandwidth is occupied by the transmission. One transmission scheme exploiting the OFDM standard is DVB-T. It has become

very popular and is established worldwide (with few adaptations e.g. in the USA) providing television. For the passive radar community it offers some advantages, e.g. it has usually a high transmit power, the occupied bandwidth is reasonably broad thus providing good range resolution possibilities. On land it is available almost everywhere, thus providing a good coverage which makes it attractive for PCL. The main advantage is, however, the possibility of recovering the transmitted waveform due to the digital modulation. This advantage generally holds for each digital transmission. Therefore it is possible to use a clean copy of the transmitted signal for range compression without introducing any errors due to correlation with a defective reference signal. For these advantages, DVB-T transmitters are one of the most frequently used transmitters of opportunity and therefore will be exploited as IO in this work.

2.2.1 Overview of the DVB-T standard

DVB-T is a variant of Digital Video Broadcasting (DVB), which is used for the transmission of audio and video content using terrestrial TX. The used frequency band is in the UHF band: $474 - 786\,\mathrm{MHz}$. One DVB-T channel covers in total a bandwidth of $8\,\mathrm{MHz}$, of which a bandwidth B_W of approximately $B_W = 7.61\,\mathrm{MHz}$ are used for data transmission [12]. The unused bandwidth of $0.39\,\mathrm{MHz}$ serves as a guard bandwidth to the adjacent DVB-T channels.

Time domain The DVB-T signal is transmitted as Continuous Waveform (CW) signal. It constitutes in time-domain of so called symbols, each of duration $\mathrm{T_S}$. Each symbol consists of a useful part of duration $\mathrm{T_U}$ and of a guard interval (also called cyclic prefix) of duration $\mathrm{T_{CP}}$: $\mathrm{T_S} = \mathrm{T_U} + \mathrm{T_{CP}}$. The guard interval is a copy of the last part of the useful part and copied before it, thus enabling cyclic continuation of the useful part. It is inserted to prevent Intersymbol Interference (ISI), which can arise due to delayed echoes with high power, or from transmissions from TXs from the same SFN, i.e. TXs transmitting the same signal content on the same frequency. The other reason for the insertion of the cyclic prefix is to enable cyclic convolution [13]. Four different values for $\mathrm{T_{CP}}$ are possible, which are listed in Tab. 2.1.

Frequency domain In frequency domain the DVB-T signal utilizes the OFDM modulation scheme, which means that each symbol comprises K separately - modulated carriers, where the frequency of each carrier is separated by $\frac{1}{\mathrm{T_U}}$ (therefore the orthogonality). The carriers are indexed with $k = 0, \ldots, K-1$.
The carriers can be divided into two groups: a group of carriers which carry non-deterministic information, i.e. the payload data, and a group of carriers which

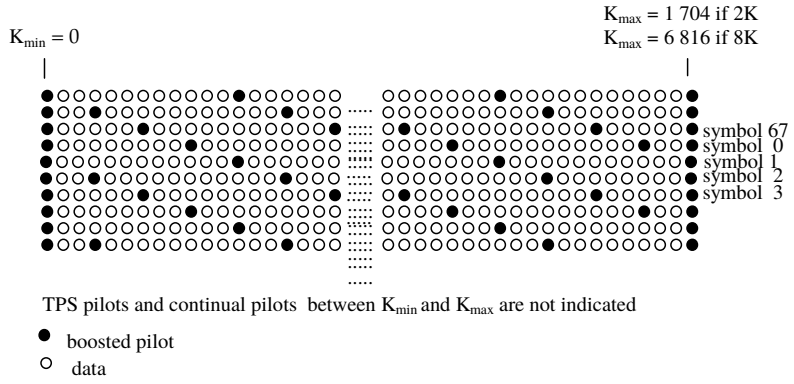

Fig. 2.3: DVB-T pilot pattern [12].

Table 2.1: Parameter of the DVB-T standard as it is used in Germany for 8 MHz channels and 8K mode.

Symbol	Description	Value
T_U	Useful symbol duration	$896\,\mu$s
T_{CP}	Guard interval duration	$T_U \cdot [\frac{1}{4}, \frac{1}{8}, \frac{1}{16}, \frac{1}{32}]$
K	Number of used carriers (payload + pilots)	6817
B_W	Used bandwidth	$T_U/K \approx 7.61\,\text{MHz}$

carry deterministic information: the so-called pilot carriers. The payload data carriers are modulated using either Quadrature Phase-Shift Keying (QPSK), or 16- or 64-Quadrature Amplitude Modulation (QAM), while the pilot carriers are modulated using Binary Phase-shift Keying (BPSK). The pilot carriers are transmitted with 3 dB higher power level compared to the average power level. They can be further subdivided into two groups, the Continual Pilot Carriers (CPC) and the Scattered Pilot Carriers (SPC). The positions $\mathbf{k}_{\text{CPC}}$ of the CPC are known and constant for each symbol. The positions $\mathbf{k}_{\text{SPC}}$ of the SPC are known as well, but the positions vary from one symbol to the next three symbols: the indices are shifted by three from symbol to symbol, i.e. for each 4th symbol the positions $\mathbf{k}_{\text{SPC}}$ repeat. The index of the positions of both CPC and SPC will be referred to using $k_p \in \mathbf{k}_p = \{\mathbf{k}_{\text{SPC}}, \mathbf{k}_{\text{CPC}}\}$
Due to their deterministic nature, the pilot carriers enable synchronization in frequency and time, and channel estimation.

2.2.2 Preprocessing of the received signal

In a single transmitter environment, the complex envelope of the received signal at the passive radar surveillance channel can be written as a function of time t as

$$\begin{aligned} s_R(t) =& a_T s_T(t) \exp(j2\pi f_{DT}(\alpha_T)t) \\ &+ \sum_{q=1}^{N_R} \int_{\Phi_q} a_q(\alpha) s(t-\tau_q) \exp(j2\pi f_{Dq}(\alpha)t) d\alpha \\ &+ \sum_{g=1}^{N_G} a_g(\alpha,\gamma) s(t-\tau_g) \exp(j2\pi f_{Dg}(\alpha,\gamma)t) \\ &+ e(t) \qquad 0 \le t \le T \end{aligned} \tag{2.5}$$

where T is the global observation time, $s_T(t)$ is the transmitted signal and a_T is its corresponding complex amplitude at the surveillance antenna, N_R is the range extent of the observed scene (expressed in range gates), Φ_q is the azimuthal angular sector of the illuminated scene, $a_q(\alpha)$ is the complex amplitude of the echo received with time delay $\tau_q = R_q/c_0$ from azimuth angle α, and R_q is the bistatic range of the q-th range gate. $f_{DT} = \frac{v_T}{c_0} f_T \cos\alpha_T$ is the Doppler frequency for the motion component relative to the transmitter. Correspondingly, $f_{Dq}(\alpha)$ is the Doppler frequency for the stationary echo received in the q-th range gate observed as defined in (2.4). Finally, the third contribution of (2.5) corresponds to contributions of N_G moving targets of delay τ_g and bistatic Doppler shift $f_{Dg}(\alpha,\gamma)$ as defined in (2.3). The component $e(t)$ is Additive White Gaussian Noise (AWGN).

The signal model introduced in (2.5) refers (for simplicity) to the MFN case, but it can be readily extended to the SFN case by summing up the contributions for each and every transmitter in the network.

2.2.3 Synchronization and reference signal reconstruction for DVB-T

The reconstruction of the reference signal in DVB-T is based on: (i) the synchronization in time and frequency on the transmitted signal (as any other DVB-T receiver should do, not only a PCL receiver); (ii) estimating the Channel Transfer Function (CTF) by exploiting the pilot carriers; (iii) decoding of the synchronized signal according to the DVB-T standard down to the sequence of bits; (iv) the remodulation of the bit sequence according to the DVB-T standard.
At the end of this processing, a replica $\hat{s}_T(t)$ of the transmitted signal is available, which is free of multipath echoes and multiple transmitter contributions, so that it can be used as the reference signal for range compression of the collected data. In contrast to analogue transmissions the reference signal can be recovered from

the received data from one of the surveillance channels (or many in the case of exploiting antenna diversity, in order to achieve a replica $\hat{s}_T(t)$ with less errors.). In fact, provided that the direct signal is the strongest contribution and the Signal-to-noise Ratio (SNR) of the direct signal is above a certain threshold, its decoding is generally possible. The threshold depends on the employed constellation map, forward-error-correction methods, platform speed, etc. [14]. Furthermore, this approach of recovering the reference signal from the surveillance data offers the possibility to use one additional surveillance channel instead of loosing a degree of freedom to a dedicated reference channel. To this approach of synchronising and recovering of the transmitted signal from a dedicated surveillance channel will be referred throughout this thesis.

In the DVB-T standard, synchronization features are represented by the scattered and continuous pilot carriers within the signal. Furthermore, since the position, amplitude and phase of these carriers are known, a comparison of their received values with the expected ones is used to determine the CTF and then to estimate by interpolation the values of the data carriers. First it is synchronized on the received signal $s_R(t)$ in order to detect the start of a DVB-T symbol in the CW signal by correlating with a reference sequence. This sequence is a synthesized segment of four DVB-T symbols containing only the known modulation of the scattered and continual pilots. Here it will be referred to as "template". Correlating the $s_R(t)$ with the template results in a detection statistic that has a dominant peak at the synchronisation position, i.e. at the beginning of four consecutive symbols with different positions of the scattered pilots in each symbol. The received signal can therefore be considered synchronised to the transmitter with an accuracy equal to half the sampling rate.

Afterwards, as the start of each symbol in terms of sample index is known, the guard intervals – which precede each useful part of a symbol – can be removed from the signal stream. In this way, the continuous waveform structure of the signal is not given anymore. The signal can now rather be considered as being similar to an active pulse-Doppler radar with a Pulse Repition Interval (PRI) equal to the duration of one complete OFDM symbol (or rather DVB-T symbol): $\mathrm{PRI} = \mathrm{T_S} = \mathrm{T_U} + \mathrm{T_{CP}}$. That is, the useful part $\mathrm{T_U}$ is comparable to a transmitted pulse of a pulse-Doppler radar, while the cyclic prefix can be considered as dead time in between the pulses. As $\frac{1}{\mathrm{T_S}} = 892.9\,\mathrm{Hz}$, this process can be considered as a pulse-Doppler radar operating in low Pulse Repition Frequency (PRF) mode [15]. By recalling (2.5) and by referring only to the direct signal contribution, the received signal corresponding to the n-th OFDM symbol after sampling and after Discrete Fourier Transform (DFT) in the frequency domain

(i.e. $S_{Rn}[k] = DFT\{s_n[l]\}$) can be written as

$$\begin{aligned} S_{Rn}[k] &= \sum_{l=1}^{K} s_n[l] e^{-\frac{j2\pi kn}{K}} \qquad k = 1, \ldots, K \\ &= S_{Rn}[k] \cdot H_n[k] + E[k] \end{aligned} \tag{2.6}$$

After removal of the guard carriers on either side of the occupied bandwidth, the CTF H_n can be estimated at the known pilot carrier positions $k_p \in [\mathbf{k}_{\mathrm{SP}}, \mathbf{k}_{\mathrm{CP}}]$ by using:

$$H_n[k_p] = \frac{S_{Rn}[k_p]}{S_{Tn}[k_p]} \tag{2.7}$$

as $S_{Rn}[k_p]$ are the received pilot carrier values and $S_{Tn}[k_p]$ are the known pilot carrier values modulated according to the DVB-T standard [12]. The CTF at the remaining carriers can be estimated using one-dimensional interpolation in frequency domain across the carriers of one symbol or as two-dimensional interpolation across multiple symbols at the pilot positions first and then across the carriers of each symbol individually. Applying the CTF on the received signal symbol-wise using:

$$S_{Tn}^{(e)}[m] = \frac{S_{Rn}[m]}{H_n[k]} \tag{2.8}$$

gives a preliminary estimate $S_{Tn}^{(e)}$ of a transmitted symbol. The carrier values of $S_{Tn}^{(e)}$ have then to be remapped to the actual values of the constellation map, which results in a "clean" (i.e. non-noisy, but not necessarily correct) estimation $\hat{S}_{Tn}$ of a transmitted symbol S_{Tn}.
The synchronisation and reference signal estimation process is also described in [16]. It has to be noted here, that CTF estimation on a stationary receiver is possible due to the orthogonality of the carriers and time-invariance of the CTF at least for the duration of one DVB-T symbol. This is not necessarily the case for a moving receiver, as due to a Doppler shifted direct signal and due to Doppler shifted multipath returns the CTF for OFDM signals might be not time-invariant anymore. However, the DVB-T standard is very robust against time-varying channels as stated in [14] and which has been confirmed recently [17]. Therefore, the described processing scheme holds as well for a stationary receiver but also for a moving receiving platform without the need of motion compensation, while being limited only by the SNR.

2.3 Related Work and Literature Review

2.3.1 Clutter Suppression Methods

Doppler spread clutter is a common problem in both active and passive radar on moving platforms. For this reason the suppression of Doppler spread clutter is a widely studied field in active radar with many contributions. One of the commonly used techniques is Space-time Adaptive Processing (STAP), on which many adaptations were suggested and still research for improvements is going on. An overview and an introduction are given in [18] and [19]. Basically STAP involves the creation of a two-dimensional filter, which is adaptive to the clutter returns in order to maximize the SNR. It is adaptive in a way as the filter is calculated using a covariance matrix $\mathbf{R}$ which is estimated from secondary. For this, $\mathbf{R}$ needs to be inverted, which can be computationally demanding as $\mathbf{R}$ can become very large as $\mathbf{R} \in \mathbb{C}^{NM \times NM}$ for the ideal STAP approach. For this reason dimension reducing STAP approaches were suggested, e.g. in [20].
Another common technique is the application of Displaced Phase-Center Antenna (DPCA) [21], [22]. The basic approach involves an antenna array equipped with two receiving channels each with one of two identical antenna elements. The elements are usually mounted in side-looking condition, and can be called Leading Antenna (LA) and Trailing Antenna (TA). The array moves along-track such that the Trailing Antenna (TA) is at the Leading Antenna (LA)'s position a defined time step T_{DPCA} later. If this requirement is satisfied, then the TA exhibits the same phase shift in clutter echoes as the LA, and the clutter can be completely removed by a simple subtraction of the range compressed pulses between both antenna elements, being only limited by thermal noise and potentially Internal Clutter Motion (ICM). Usually $T_{\mathrm{DPCA}} = K \cdot \mathrm{PRI} = \frac{K}{\mathrm{PRF}}$, where PRI and PRF define the PRI and PRF. This requirement is labelled the DPCA condition and involves:

$$v_R = \frac{d}{T_{\mathrm{DPCA}}} = \frac{d}{K \cdot \mathrm{PRI}} \tag{2.9}$$

i.e. there is a strict requirement for v_R, as it is dependent on the PRI. As only time delays and subtractions are involved for DPCA, it does not have as high computational demands as for STAP.
Among the ICM, another limitation is the non-ideal displacement of the TA's phase centre as the platform is susceptible to wind or sea-state and therefore does not move as required by (3.8). In active radar the latter issue might be compensated by adapting the PRI to the platform's velocity. In PCL this is not possible, as the transmitted waveforms are not under control of the radar operator, i.e. the PRI can not be adapted in the required flexibility (given that the processing as

described in 2.2.3 is carried out).
Another issue for PCL refers to the time-varying characteristics and to the strong ambiguities inherent in the transmitted waveforms, which limit the clutter cancellation of DPCA even for ideal DPCA conditions, but as well for STAP approaches.

2.3.2 Passive Radar on moving platforms

Although stationary PCL systems are established now and the first commercial PCL systems are on the market, research about PCL on moving platforms with the application of Moving Target Indication (MTI) or Synthetic-aperture Radar (SAR) is still at the beginning.
The first time when PCL was considered for moving target detection using clutter suppression methods like STAP was in 2006 by Neyt et al. in [23]. The authors considered a passive radar receiver exploiting GSM transmissions. First the authors generalized STAP for noise-like signals, applying the Matched Filter (MF). Then, in order to remove the direct signal, a filter based on covariance matrix estimation was created. Th show the performance, simulations were shown for a forward-looking moving receiver. Real data and its evaluation was as well shown, however, the data was acquired from a stationary platform.
In [24] and [25] the work and results for air-borne PCL using FM transmitters were presented. This was the first time, that a passive radar was mounted on an air-borne platform, and as the detection of targets was demonstrated, this was the proof of concept of air-borne passive radar. Furthermore, the behaviour of stationary ground clutter was analysed and an image of stationary ground clutter was created using Doppler beam sharpening. However, a method to suppress the clutter returns was not applied, thus leaving further research possibilities.
To this aim, the authors of [26] and [27] considered the use of DPCA on real data from FM transmissions, and on simulated DVB-T data in order to suppress clutter returns in an airborne system. The authors state that the dependence of DPCA on the platform velocity and the PRI can be neglected, as the broadcast transmissions are CW transmissions. Due to this fact any required temporal delay between the collected data from both channels can be obtained in a digital signal processing stage by properly selecting the correct data. This selection is precise up to the sampling frequency. In fact this is true for any CW transmission formats, but the authors did not consider the signal characteristics in the digital modulated waveform, which can hinder target detection. The authors applied matched filtering for range compression, which increases the SNR, but also leads to ambiguities and sidelobes in the ambiguity function. This can severely limit the target detection and the clutter suppression performance of DPCA.
In [28] and [29] the results of seaborne trials were presented. The work's focus is mainly on the study of transmitter imperfections and their influence on the am-

biguity function. It is presented how transmitter non-idealities lead to increased Doppler sidelobes of the direct signal, thus increasing the noise floor and limiting target detection. While this contribution's focus was not on target detections but on the description of transmitter imperfections in MFN networks, it states an important contribution for PCL, as it describes the dependence of the TX, which has not been considered to this date, but it also provides a possibility to overcome the limitations.
Knowledge of the reference signal is crucial in passive radar, factors leading to poor reference signal estimation, can severely hinder target detection. This issue is addressed in [17], where the authors study the influence of Intercarrier Interference (ICI) due to fast time-varying channels (e.g. due to platform motion) on the reference signal estimation. The authors come to the conclusion that ICI can be neglected as a major drawback for reference signal estimation, but provide techniques and algorithms to improve reference signal estimation and show the effectiveness on data from an airborne measurement campaign using a DVB-T TX as IO.

2.3.3 Ambiguity suppression in Passive Radar

The deterministic components enabling synchronisation and channel estimation are a crucial requirement for recovering the transmitted signal. However, simultaneously they lead to ambiguities, thus impeding target detection.
Cherniakov describes this issue in [30] based on DVB-T transmissions. The impact is described and simulations visualize the drawback. A possibility on ambiguity suppression is provided, for which a differentiation in intersymbol ambiguities and intrasymbol ambiguities is done and peaks resulting from guard interval correlations. Intersymbol ambiguities result from correlations between different symbols, whereas intrasymbol ambiguities result from correlations in the symbol itself. In order to cope with the ambiguities, a three step process is proposed which involves: (i) blanking of the guard interval to remove guard interval correlation peaks, and (ii) two complementary procedures: power equalization (i.e. mismatch filtering) of the pilots leading to intrasymbol ambiguities and notch filtering of the pilots leading to intersymbol peaks before correlation. In a third step (iii) the filtered signals are selectively combined to create an ambiguity-free signal.
In [31] the DVB-T waveform as well as two other digital waveforms are considered, namely WiFi and WiMAX transmission. The ambiguity peaks in WiFi result from a Pseudorandom Binary Sequency (PRBS) exploited for the transmission. A two step process for ambiguity removal is employed, which involves the creation of a filter via convex optimization to suppress the peaks at shorter range and afterwards a further sidelobe reduction by subtracting from the Ambiguity Function (AF) a properly scaled and weighted copy of the AF.

In the WiMAX transmission the ambiguous peaks result from guard interval, and from fixed and variable pilots, all in all deterministic components similar to DVB-T. As these are deterministic it is suggested to create a linear filter to suppress the ambiguities, where the designed filter is an inverse filter (or reciprocal filter) and able to remove the ambiguities at non-zero delay.
It is suggested to apply the inverse filter also for DVB-T signals, which effectively removes ambiguities at zero-Doppler and ambiguities resulting from intersymbol correlations, however intrasymbol correlations remain, probably due to missing guard-interval blanking. To overcome this issue, it is referred to the approach in [30].
A deeper analysis of the impact on DVB-T waveforms can be found in [32]. The positions where the ambiguities appear, depending on the duration T_U of the useful part and on the duration T_{CP} of the exploited guard interval length, is given. A technique for ambiguity suppression is given and its performance is deeply analysed against simulated and real data.
Glende presents in [33] the application of the reciprocal filter in order to effectively suppress the ambiguities:

$$H(f) = \frac{\beta^2}{\hat{S}(f)} \tag{2.10}$$

where $H(f)$ denotes the filter, and β is used as a threshold factor to prevent overweighting of signal content with low spectral amplitude. This is especially necessary for analogue modulated waveforms, as the reference signal can not be recovered and due to noise and bad signal reception the denominator might become zero.

Conclusion and summary The deterministic components appearing as peaks in the ambiguity function affect the target detection and can even blind the PCL system against particular targets. Therefore different techniques were suggested to overcome this issue. However, so far there is no publication where the influence of the non-deterministic components was analysed, i.e. the increased noise floor which arises due to matched filtering. In fact, matched filtering maximizes the SNR, but as each OFDM symbol is different and therefore all impulse responses after matched filtering vary, there is a non-correlated increased noise floor in the range-Doppler map. Considering clutter suppression techniques for moving platforms, e.g. DPCA, the time-variant impulse responses degrade the clutter suppression performance. It has not been studied yet, how the DPCA processing is affected if the matched filter is used for range compression, and furthermore, no alternative to the matched filter for PCL on moving platform has neither been suggested nor analysed. Clearly, there are open questions in passive radar research.

Chapter 3

Problem formulation, signal model, and analysis

3.1 Signal model and geometry

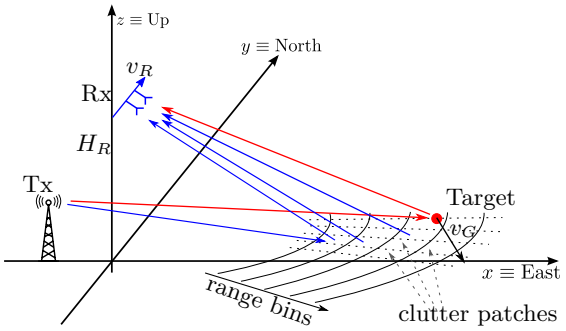

Fig. 3.1: System geometry.

Introduction A passive radar mounted on a moving platform is considered. It exploits a terrestrial TX as IO, that transmits digital modulated waveforms. Without loss of generality, DVB-T is considered as transmitted waveform. The moving platform carrying the receiving equipment moves at constant altitude H_R with a constant velocity of $\mathbf{v}_R = [v_{Rx}, v_{Ry}, v_{Rz}] = [0, v_{Ry}, 0]$ along the y-axis, see Fig. 3.1. The absolute velocity of the platform is defined as $v_R := |\mathbf{v}_R|$. The ground is flat for simplicity, i.e. the ground does not exhibit any distinctive clutter features.

General parameters of receiver The RX is equipped with two identical receiving channels, each connected to an identical antenna element. The antennas

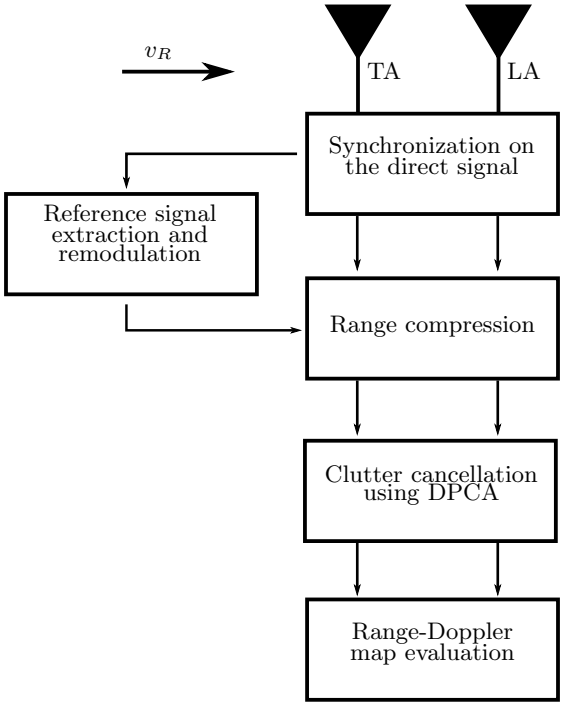

Fig. 3.2: Flowchart of the processing.

are displaced by $d = \lambda_T/2$ in along-track direction, mounted in pure side-looking configuration. $\lambda_T = c_0/f_T$ refers to the wavelength of the centre frequency f_T and c_0 describes the speed of light. The first antenna element will be referred to as LA, the second element will be referred to as TA. The RX's velocity v_R is set to $v_R = d/T_{\mathrm{DPCA}} = d/T_D = d/(K \cdot \mathrm{PRI})$. In this way the TA occupies the same spatial position as the LA after an amount of time T_D, i.e. it fulfils the DPCA condition [22], where PRI is considered to correspond to the DVB-T symbol duration $\mathrm{T_S}$.

Processing overview The platform moves along the defined trajectory, while the receiver samples signals within the DVB-T band in order to search for and detect moving targets within the collected data. To do so the signals are digitised after a downconversion in both receiving channels. After a preprocessing of the data, which involves synchronisation and reference signal reconstruction (described in Sec. 2.2.3), the data is range-compressed in a dedicated range compression stage. Afterwards, a clutter cancellation stage is applied, here it is considered to use DPCA, as two receiving chains and antenna elements are used. Finally it can be searched for targets in the resulting range-Doppler map. This process is shown in the flowchart in Fig. 3.2.

Received signal model As the RX is moving along the defined trajectory, it receives echoes $r_C^{(\zeta)}(t)$ from stationary objects, i.e. clutter, and echoes $r_G^{(\zeta)}(t)$ from moving objects, i.e. targets, at both antenna elements:

$$r^{(\zeta)}(t) = r_C^{(\zeta)}(t) + r_G^{(\zeta)}(t) + r_N^{(\zeta)}(t) \tag{3.1}$$

$r_N^{(\zeta)}$ defines AWGN at both receiving channels $\zeta := [LA, TA]$; statistically independent between both receiving channels.
The clutter component consists of a superposition of stationary point-like scatterers, while the target component consists of a non-stationary point-like scatterer.
The return from a point-like scatterer with complex amplitude A_0 can be written as:

$$\begin{aligned} r_0^{(LA)}(t) &= A_0 s(t-\tau_0)\exp(2\pi j f_{D_0} t) \\ r_0^{(TA)}(t) &= A_0 s(t-\tau_0)\exp(2\pi j f_{D_0} t)\exp(-2\pi j \frac{d}{\lambda_T}\cos\alpha_0) \end{aligned} \tag{3.2}$$

where t and τ_0 define time and bistatic propagation delay: $\tau_0 = (R_T + R_R - B_L)/c_0$.
f_{D_0} defines the bistatic Doppler shift for a signal reflected from a point-scatterer as defined in (2.3) and (2.4) for a target, and for a stationary scatterer, respectively.
$s(t)$ defines the baseband signal which has been emitted by the TX.
The signal will be sampled with sampling frequency f_S after down-conversion in the receiving hardware:

$$\begin{aligned} r_0^{(LA)}[l] &= A_0 s[l - l_{\tau_0}]\exp(2\pi j f_{D_0} l/f_S) \\ r_0^{(TA)}[l] &= A_0 s[l - l_{\tau_0}]\exp(2\pi j f_{D_0} l/f_S)\exp(-2\pi j \frac{d}{\lambda_T}\cos\alpha_0) \end{aligned} \tag{3.3}$$

where $l = t f_S$ and $l_{\tau_0} = \tau_0 f_S$.
In the next processing steps one Coherent Processing Interval (CPI), consisting of N_S symbols $n = [0, \ldots, N_S - 1]$ is regarded. It is furthermore assumed, that A_0 is constant, or non-fluctuating for one CPI (i.e. following a Swerling1 model).

$$\begin{aligned} r_0^{(LA)}[l,n] &= A_0 \left(\sum_n^{N_S} s_n[l - nL_s - l_{\tau_0}] \right) \exp(2\pi j f_{D_0} nT) \\ r_0^{(TA)}[l,n] &= A_0 \left(\sum_n^{N_S} s_n[l - nL_s - l_{\tau_0}] \right) \exp\left(2\pi j f_{D_0} nT\right) \exp\left(-2\pi j \frac{d}{\lambda_T}\cos\alpha_0\right) \end{aligned} \tag{3.4}$$

where L_S resembles the number of samples in one OFDM symbol $L_S = \mathrm{T_S} f_S$.
The signals $r_C^{(\zeta)}$ consists of a superposition of contributions from stationary scatterers appearing at different range cells $r = 1, \ldots, N_{RC}$, and seen under different

angles α within the angular sector Φ_A with amplitudes $A_r(\alpha)$. In order to study the capability of the clutter cancellation stage, ICM is neglected here. The amplitudes can be modelled as zero mean complex Gaussian random variables with variance $\sigma_C^2(\alpha) = E\{|A_r(\alpha)|^2\} = E\{|A_r|^2\}$. The amplitudes $A_r(\alpha)$ appearing at different range cells and angles are assumed to be statistically independent within one CPI:

$$E\{A_r(\alpha)A_i^*(\alpha')\} = 0, \text{ for } r \neq i, \text{ for } \alpha \neq \alpha' \tag{3.5}$$

The clutter signal model can be written as:

$$\begin{aligned}
r_C^{(LA)}[l,n] &= \sum_r^{N_{RC}} \int_{\Phi_A} r_r^{(LA)}[l,n,\alpha]d\alpha \\
&= \sum_r^{N_{RC}} \int_{\Phi_A} A_r(\alpha) \sum_n^{N_S} [l - nL_s - l_{\tau_r}] \exp(2\pi j f_D(\alpha) n \mathrm{T_S}) d\alpha \\
r_C^{(TA)}[l,n] &= \sum_r^{N_{RC}} \int_{\Phi_A} r_r^{(TA)}[l,n,\alpha]d\alpha \\
&= \sum_r^{N_{RC}} \int_{\Phi_A} A_r(\alpha) \sum_n^{N_S} [l - nL_s - l_{\tau_r}] \exp(2\pi j f_D(\alpha) n \mathrm{T_S}) \\
&\quad \cdot \exp(-2\pi j \frac{d}{\lambda_T} \cos\alpha) d\alpha
\end{aligned} \tag{3.6}$$

The direct signal is excluded from the equations above. It is assumed that it is suppressed by a dedicated cancellation stage [34], which allows to study and to highlight the signal processing for the clutter suppression.
A simulation was done according to (3.6), where the scene is set to $N_{RC} = 1000$ range cells, while for the antenna pattern an omnidirectional pattern is chosen. The angular sector for each range cell r is in the range of $\Phi_{Ar} = \Phi_A = [0, \pi],\ \forall\ r$, and the carrier frequency was set to $f_T = 600\,\mathrm{MHz}$, which leads to a wavelength of $\lambda_T = 0.5\,\mathrm{m}$.

The platform velocity amounts $v_R \cong 24.8\,\mathrm{m/s}$, such that the DPCA condition is fulfilled for an antenna spacing $d = \frac{\lambda_T}{2} = \frac{c_0}{2f_T} = 0.25\,\mathrm{m}$ and integer multiples of the symbol duration T_S:

$$v_R = \frac{d}{K \cdot T_S},\ K \in \mathbb{N} \tag{3.7}$$

$$= \frac{d}{T_{\mathrm{DPCA}}} = \frac{d}{T_D} \tag{3.8}$$

DVB-T simulation The clutter model was multiplied with a simulated DVB-T signal. It is simulated according to the DVB-T standard [12]: the durations $\mathrm{T_U}$ and $\mathrm{T_{CP}}$ were set to $\mathrm{T_U} = 896\,\mu\mathrm{s}$ and $\mathrm{T_{CP}} = \frac{1}{4}\mathrm{T_U} = 224\,\mu\mathrm{s}$ giving a total duration of $\mathrm{T_S} = \mathrm{T_U} + \mathrm{T_{CP}} = 1120\mu\mathrm{s}$. The constellation map was chosen to be 16-QAM. All the payload data values were discrete uniform distributed in $\mathcal{U}\{0, 15\}$, such that they can easily be mapped to the constellation map. The pilot carriers were simulated according to the definitions in the standard. A CPI of the simulated signal was selected to consist of 512 DVB-T symbols, leading to a total duration of $T_{\mathrm{CPI}} = 512 \cdot \mathrm{T_S} \approx 0.57\,\mathrm{s}$.

3.2 Problem formulation

As is well known, clutter returns will appear spread in the Doppler domain due to platform motion, so that they are likely to mask echoes from slowly moving targets[1]. This effect is more severe in PCL systems since the AF of the employed waveforms of opportunity shows a generally high sidelobes level both in range and in Doppler. Basically, clutter echoes generated at a given range cell will affect, through their sidelobes of the deterministic and non-deterministic components, range cells which are distant to the originating one. Therefore, they are likely to affect the detection of targets appearing at other cells even in the presence of a large range/Doppler separation.
To better understand the effects of this phenomenon, a conventional signal processing based on the MF at the range compression stage is considered. The range compression is performed on signal fragments of length $L = \mathrm{T_U} f_S$, i.e. on the useful part of a DVB-T symbol, after removal of the cyclic prefix and the guard carriers. It can be assumed that the received signals are synchronised to the start of the DVB-T template (according to Sec. 2.2.3). Furthermore it is assumed that the transmitted signal is ideally reconstructed and serves as reference signal for range compression. Then the output of the range compression stage can be written as:

$$\begin{aligned} \bar{x}^{(\alpha)}[l,n] &= r^{(\alpha)}[l,n] * h[l,n] \qquad n = 0, \ldots, N_S - 1 \\ &= \mathrm{IDFT}\{\mathrm{DFT}\{r^{(\alpha)}[l,n]\} \odot \mathrm{DFT}\{h[l,n]\}\} \end{aligned} \tag{3.9}$$

where the operators '$*$' and '$\odot$' denote convolution, which is performed on a fragment-wise basis, and element-wise multiplication respectively. The output of this stage is arranged in a slow-time/fast-time matrix (indicated by the bar

[1] A target is considered as slow moving, if its Doppler shift f_{D_G} falls within the Doppler bandwidth of the clutter, i.e.: $f_{D_G} \leq f_{D_{\mathrm{Cl}}}^{(\max)} = \frac{v_R}{\lambda_T}$

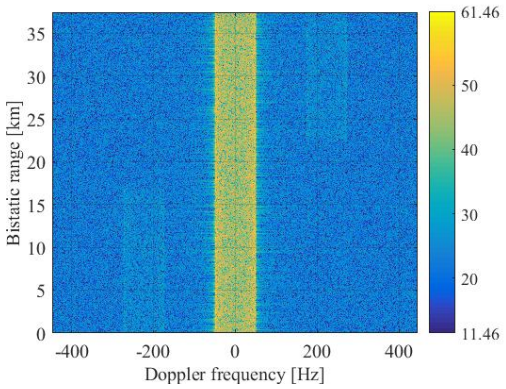

Fig. 3.3: Range-Doppler map for the matched filtered for a simulated scenario following (3.9).

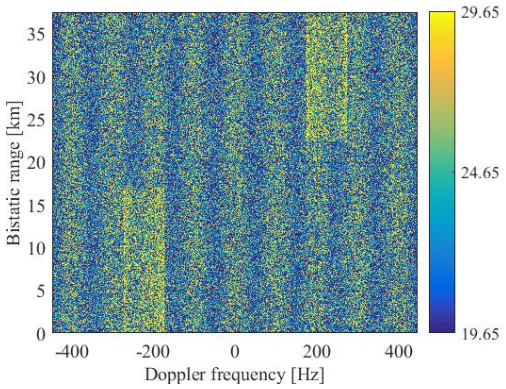

Fig. 3.4: Range-Doppler map for the simulated scenario including only clutter echoes after DPCA processing, following (3.10).

above the symbol) $\bar{x}^{(\alpha)}[l,n]$, where the n-th column of $\bar{x}^{(\alpha)}[l,n]$ contains the n-th fragment (i.e. range-compressed DVB-T symbol) after range compression. The next step in the processing is the application of DPCA in order to suppress clutter according to (3.10) and a Doppler DFT across slow-time dimension according to (3.11):

$$\bar{y}[l,n] = \bar{x}^{(LA)}[l,n] - \bar{x}^{(TA)}[l,Kn] \tag{3.10}$$

$$\bar{z}[l,m] = \sum_{n=0}^{N_{\mathrm{FFT}}-1} \bar{y}[l,n] \exp(-2\pi jmn/N_{\mathrm{FFT}}) \tag{3.11}$$

where N_{FFT} defines the length of the Doppler DFT, and K is as defined in 3.8.
In Figs. 3.3 and 3.4 two range-Doppler maps are displayed. The range-Doppler map in Fig. 3.3 is the Doppler integrated output of (3.9) for $\zeta = \mathrm{LA}$. The range-Doppler map in Fig. 3.4 shows the output of (3.11), that is the Doppler integrated result after DPCA application. Fig. 3.3 is lower limited to 50 dB below the highest peak appearing at 61.46 dB. For this, the generated signal was scaled in amplitude so that the overall clutter contribution has an assigned power level $P_C^{(\mathrm{in})} = 30\,\mathrm{dB}$ above a reference thermal noise level, which was set to unity. However, in the examples shown in Fig. 3.3 and Fig. 3.4 noise was not included during the evaluation. Only one receiving channel is shown in Fig. 3.3, but the same power level was applied for both receiving channels.
When analysing Fig. 3.3 one can see different distinctive features:
First, strong clutter returns appear at all the considered range cells across a clutter Doppler bandwidth $B_{WD} \approx [-50, 50]\,\mathrm{Hz}$. The width of the clutter ridge depends

on the platform's velocity v_R, the transmit frequency f_T and the antenna pattern, as well as from the angles from which the returns arrive. Similar to an active radar, these effects can mask weak as well as slow moving target returns.
Second, a generally high clutter power level is observed at higher Doppler regions centred at $\pm\text{PRF}/2 \approx \pm 223\,\text{Hz}$, which covers the same amount in Doppler as the clutter appearing at zero-Doppler. This effect results from the high sidelobes of the AF of the employed signal's waveform, which has been studied in [35] where the authors provide an estimate of the power level of the observed range-Doppler map background for a single point-like scatterer. This means, the ambiguities resulting from deterministic components lead to high clutter power levels, which span a range in Doppler, which is as well dependent on the platform's velocity. The centres of the bandwidth are at positions in Doppler, that are only dependent of the characteristics of the employed waveform. The positions of their appearance are listed and analysed in detail in [36] and [32]. The extension in bistatic range is due to the simulated clutter for $N_{RC} = 1000$ range cells.
Third, one observes a generally higher power level across the whole range-Doppler map, which is due to sidelobes from deterministic and non-deterministic components.
When analysing Fig. 3.4 one can notice different distinctive features as well. First, the clutter ridge has been cancelled by about 35 dB, i.e. the DPCA cancellation stage has been effective here. However, one notices second, that the higher clutter power levels which were observed at $\pm 223\,\text{Hz}$ in Fig. 3.3 are not cancelled, instead they appear now as the highest contributions in the map, although ideal conditions (no ICM, fulfilment of the DPCA condition, no mis-calibrations or channel non-idealities) were assumed. Third one can see a high background noise level across the whole range-Doppler map which has a repetitive pattern consisting of equally spaced maxima and minima.
The reason for the clutter not being cancelled out, is due to the fact that the impulse response of symbol n after matched filtering is different for each symbol n. However for the DPCA technique to be effective, a train of coherent time-invariant pulses needs to be transmitted (among absence of ICM, calibrated receiving channels, etc.), as it is usually the case for MTI from an active radar. This means that clutter cancellation techniques will not be effective and cancel clutter returns totally, as implied by the emitted time-varying symbols, the impulse responses vary.

Conclusion and problem statement These results lead to the conclusion, that the MF is not a valid and suitable approach for range compression in PCL systems exploiting digital modulated waveforms, as the impulse response after matched filtering changes from OFDM symbol to symbol due to the varying con-

tent, i.e. it is not stationary over time, and therefore the clutter returns can not be cancelled completely. As time-invariant pulses are a crucial factor for a successfully working MTI radar, but the transmitted signal can not be adapted, proper techniques must be found, to solve this issue.
The best way to solve this issue is to change the processing such that a time-invariant impulse-response is achieved. For this, the filter applied for range compression must be changed. It is here suggested to use the so-called Reciprocal Filter (RpF) for range compression. The Reciprocal Filter (RpF) removes the signal characteristics and equalises the output of the range compression stage, which means this filter is able to create a time-invariant impulse response for each symbol n.
In this work the limitations in terms of clutter suppression and target detection when using the MF will be studied. Then the RpF will be applied for range compression. The output of each processing stage will be mathematically analysed in detail and compared to the results of the MF, as well by means of simulations and data evaluation from measurement campaigns.

3.3 Limitations of Matched Filter

3.3.1 Single point-like scatterer

To understand the limitations of matched filtering and the influence it has on the DPCA clutter cancellation stage, the clutter output power $P_C^{(\text{out})}[l,m]$ as a function of the delay-Doppler bin $[l,m]$ will be studied, namely at the end of Fig. 3.2 after the clutter cancellation stage.
First, only one point-like scatterer will be considered. The output of (3.9) is then:

$$\begin{aligned} x^{(\text{LA})}[l,n] &= A_0 g_n^{(\text{MF})}[l-l_{\tau_0}]\exp(j2\pi\frac{v_R}{\lambda}\cos\alpha_0 n\text{T}_\text{S})\exp(-j2\pi\frac{v_B}{\lambda}n\text{T}_\text{S}) \\ x^{(\text{TA})}[l,n] &= A_0 g_n^{(\text{MF})}[l-l_{\tau_0}]\exp(j2\pi\frac{v_R}{\lambda}\cos\alpha_0 n\text{T}_\text{S})\exp(-j2\pi\frac{v_B}{\lambda}n\text{T}_\text{S}) \\ &\qquad \cdot\exp(-j2\pi\frac{d}{\lambda}\cos\alpha_0) \end{aligned} \tag{3.12}$$

where

$$g_n^{(\text{MF})}[l] = s_n[l-nL_S] * h_n^{(\text{MF})}[l] = \kappa\text{IDFT}\{|S_n[m]|^2\} \tag{3.13}$$

is the output of the filter matched to the n-th OFDM symbol $s_n[l-nL_S]$, $S_n[m]$ being the DFT of $s_n[l]$, i.e. and IDFT defining the Inverse Discrete Fourier Transform (IDFT).
As described in 2.2.1 the DVB-T signal is a broadcast signal. Due to the transmitted information its payload content varies from symbol to symbol, therefore

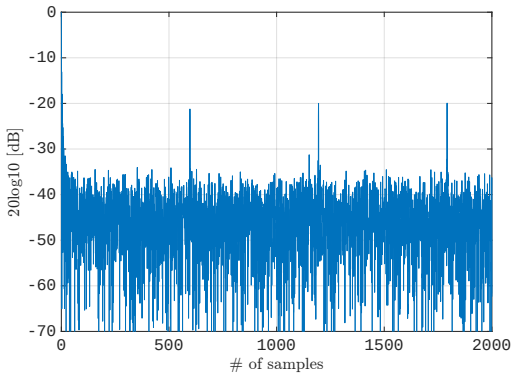

Fig. 3.5: Impulse response of one matched filtered DVB-T symbol.

the impulse response $g_n[l]$ after matched filtering for a particular symbol $s_n[l]$ is different from the output response $g_p[l]$ for a symbol $s_p[l]$, if $n \neq p$:

$$\begin{aligned} &s_n[l] \neq s_p[l], \text{ for } n \neq p \quad \Rightarrow \quad h_n[l] \neq h_p[l] \\ &g_n[l] \neq g_p[l] \end{aligned} \tag{3.14}$$

In Fig. 3.5 the impulse response of one matched filtered DVB-T symbol is shown. One can clearly see strong peaks approximately 20 dB below the main peak, which appear due to the deterministic components (pilots) in the waveform and usually show periodic repetitions across consecutive OFDM symbols within a frame. Furthermore one notices a quite constant background level of approximately 40 dB below the main peak. This noise floor is due to correlation of the non-deterministic payload data transmitted on the data sub-carriers and varies from impulse response to impulse response. The power of the impulse response was aligned relative to the main peak, which is independent of n if equal energy fragments are used.
In the following analysis the deterministic components are neglected. Instead the signal is modelled as a random waveform with zero-mean and variance $\sigma_s^2 = E\{|s[l]|^2\}$.
Specifically a CW transmission with constant power during the observation time is considered. The signal fragments $s_n[l],\ n = 0, \ldots, N_S - 1$ are statistically independent.
Under these assumptions, the samples of the autocorrelation $g_n^{(\mathrm{MF})}[l] = s_n[l]s_n^*[l]$ can be treated as random variables, statistically independent across consecutive

batches, with mean value and variance given by:

$$E\{g_n^{(\mathrm{MF})}\}[l] = E\left\{\sum_{\nu=0}^{L} s_n[\nu]s^*[\nu+l]\right\} \qquad \forall\ n=0,\ldots,N-1 \tag{3.15}$$
$$= \sum_{\nu=0}^{L} E\{s[\nu]s^*[\nu+l]\} = \kappa L\sigma^2\delta[l]$$

$$\mathrm{Var}\{g_n^{(\mathrm{MF})}\} = \kappa^2 L\sigma^4(\mu-1) \qquad \forall\ n=0,\ldots,N-1 \tag{3.16}$$

where $\mu = \frac{1}{M_C}\sum_{m=0}^{M_C-1}|c_m|^4$ is dependent on the adopted modulation scheme, and $M_C = \{4, 16, 64\}$ for QPSK, 16-QAM, and 64-QAM. The corresponding constellation is defined so that it has a unitary average power, $\frac{1}{M_C}\sum_{m=0}^{M_C-1}|c_m|^2 = 1$, and $\{c_m\}_{m=0,\ldots,M_C-1}$ being the constellation symbols of the corresponding constellation map. The evaluation of the variance can be found in the appendix 8.A. Eqs.(3.15) and (3.16) lead to a Peak-to-sidelobe Ratio (PSLR) of:

$$\mathrm{PSLR} = \frac{|E\{g_n^{(\mathrm{MF})}\}[0]|^2}{\mathrm{Var}\{g_n^{(\mathrm{MF})}\}[l]} = \frac{|\kappa L\sigma^2|^2}{\kappa^2 L\sigma^4(\mu-1)} = \frac{L}{\mu-1} = \\ = \frac{B\mathrm{T_S}}{\mu-1} \tag{3.17}$$

Apparently, for the QPSK case, the variables $g_n^{(MF)}[l]$ become deterministic as all the transmitted symbols have equal energy and the power spectral density of any signal fragment is therefore deterministically and continuously flat. This result might slightly differ from the actual output of the simulated clutter and DVB-T signal, as the presence of pilot carriers was neglected in the equations above. The discussion in the following will be mostly referred to the widely exploited 16-QAM and 64-QAM schemes.

A more general result was originally developed in [35] at the output of the range–Doppler map evaluation. In (3.15) and (3.16), it is focused on the range compression stage outputs that represent the input of the clutter cancellation stage under investigation based on DPCA. However, the results reported in (3.15) and (3.16) can be easily derived from the corresponding equations of [35] by neglecting the effect of the Doppler processing stage.

After the DPCA-based cancellation stage (where the DPCA condition is fulfilled: $d = v_R K\mathrm{T_S}$, see (3.8)), the scatterer contribution becomes:

$$\begin{aligned} y_0[l,n] =& x_0^{(TA)}[l,n] - x_0^{(LA)}[l,n-K] \\ =& A_0\Big(g_n^{(\mathrm{MF})}[l-l_{\tau_0}] - \exp(j2\pi\frac{v_B}{\lambda}K\mathrm{T_S})g_{n-K}^{(\mathrm{MF})}[l-l_{\tau_0}]\Big) \\ & \cdot\exp(j2\pi\frac{v_R}{\lambda}\cos\alpha_0(n-K)\mathrm{T_S})\exp(-j2\pi\frac{v_B}{\lambda}n\mathrm{T_S}) \end{aligned} \tag{3.18}$$

In the case $v_B \neq 0$ for a moving target, its contribution is not totally filtered out due to its phase shift of $2\pi v_B/\lambda K\mathrm{T_S}$, as expected from the DPCA application. However, unlike to conventional active radar exploiting periodic time-invariant waveforms, the contribution from a stationary scatterer provides a non-zero output although a constant amplitude A_0 at temporally displaced observations was assumed. This is because the shape of the impulse response changes for each n (compare (3.14)).
To achieve a range-Doppler map, the output of the DPCA-based stage is then integrated by a DFT, as described in (3.10):

$$\begin{aligned} z_0[l,m] =& \sum_{n=0}^{N-1} y_0[l,n] \exp(-j2\pi \frac{m}{N} n) \\ =& A_0 \exp(-j2\pi \frac{v_R}{\lambda} \cos\alpha_0 K\mathrm{T_S}) \sum_{n=0}^{N-1} \exp(j2\pi (f_{D_0}\mathrm{T_S} - \frac{m}{N})n) \\ & \cdot \left(g_n^{(\mathrm{MF})}[l - l_{\tau_0}] - \exp(-j2\pi \frac{v_B}{\lambda} K\mathrm{T_S}) g_{n-K}^{(\mathrm{MF})}[l - l_{\tau_0}] \right) \end{aligned} \tag{3.19}$$

where $f_{D_0} = \frac{1}{\lambda}(v_R \cos\alpha_0 - v_B)$. Eq. (3.19) represents the output contribution of a point-like scatterer belonging to the delay-Doppler bin $[l_{\tau_0}, f_{D_0} N\mathrm{T_S}]$ observed at the delay-Doppler bin $[l,m]$. That means, as the echo of a stationary point-like scatterer ($v_B = 0$) is not perfectly cancelled in (3.18), its contribution will be spread all over the range-Doppler map, thus leading to an increased floor moving targets have to compete with.
Based on the assumption of a random noise-like waveform, the mean value of the output in (3.19) can be written as:

$$\begin{aligned} E\{z_0[l,m]\} =& A_0 \exp(-j2\pi \frac{v_R}{\lambda} \cos\alpha_0 K\mathrm{T_S}) \exp(j\pi \frac{v_B}{\lambda} K\mathrm{T_S}) \kappa L \sigma^2 \delta[l - l_{\tau_0}] \\ & \cdot \left(-2j \sin\left(\pi \frac{v_B}{\lambda} K\mathrm{T_S} \right) \right) \exp\left(j2\pi \left(f_{D_0} - \frac{m}{N\mathrm{T_S}} \right) (N-1)\mathrm{T_S} \right) \\ & \cdot \mathrm{dsinc}\left[\pi (f_{D_0} - \frac{m}{N\mathrm{T_S}})\mathrm{T_S}, N \right] \end{aligned} \tag{3.20}$$

where $\mathrm{dsinc}(x,N) = \sin(Nx)/\sin(x)$ is the digital sinc function. Eq. 3.20 yields a non-zero value only at the delay-Doppler bin where the scatterer belongs to (and at its ambiguous Doppler location), i.e. $l = l_{\tau_0}$ and $\frac{m}{N\mathrm{T_S}} = f_{D_0} + \frac{r}{\mathrm{T_S}}$, $r \in \mathbb{Z}$. However it can be observed that this mean value is identically equal to zero all over the delay-Doppler plane when $v_B = 0$.
Focusing on a stationary scatterer, the second moment of the output in (3.19) is

evaluated as:

$$\begin{aligned} E\{|z_0[l,m]|^2|v_B=0\} =&|A_0|^2 \sum_{n=0}^{N-1}\sum_{p=0}^{N-1} f[l,n,p] \\ &\exp\left(j2\pi\left(f_{D_0}-\frac{m}{N\mathrm{T_S}}\right)(n-p)\mathrm{T_S}\right) \end{aligned} \tag{3.21}$$

where

$$\begin{aligned} f[l,n,p] =&E\big\{\big(g_n^{\mathrm{MF}}[l-l_{\tau_0}]-g_{n-k}^{\mathrm{MF}}[l-l_{\tau_0}]\big) \\ &\cdot\big(g_p^{*\mathrm{MF}}[l-l_{\tau_0}]-g_{p-k}^{*\mathrm{MF}}[l-l_{\tau_0}]\big)\big\} \\ =&\begin{cases} 2\mathrm{Var}\{g_0[l]\} & p=n \\ -\mathrm{Var}\{g_0[l]\} & p=n\pm K \\ 0 & \text{elsewhere} \end{cases} \end{aligned} \tag{3.22}$$

And using (3.16), (3.21) is then:

$$E\{|z_0[l,m]|^2|v_B=0\} \cong 4|A_0|^2\kappa^2 L\sigma^4(\mu-1)N\sin^2\left(\pi\left(f_{D_0}-\frac{m}{N\mathrm{T_S}}\right)K\mathrm{T_S}\right) \tag{3.23}$$

where the border effects, which result from the exploitation of a limited number of slow-time samples are neglected.
As can be seen in (3.23), it can be observed that the output power level for a stationary scatterer is equal to zero only at Doppler bin $m = f_{D_0}N\mathrm{T_S}$. In contrast, a stationary scatterer belonging to a given delay-Doppler bin $[l_{\tau_0}, f_{D_0}N\mathrm{T_S}]$ contributes to the delay-Doppler bin $[l,m]$, where the output power level is modulated by a $\sin^2$ shape in the Doppler dimension. Therefore, this cancellation residual limits the detection of the echo from a moving target.
Although ideal conditions were assumed, a perfect removal of the contribution from a stationary scatterer is not possible, due to the varying shape of the employed waveform.

Target contribution Here the contribution of a moving target at the delay-Doppler bin where it is expected to appear will be analysed. The target has a delay of $l_{\tau_T} = \tau_T f_S$ and a bistatic velocity of v_{B_T}, yielding to a bistatic Doppler of f_{D_T} and a complex amplitude A_T. Using (3.19) yields:

$$\begin{aligned} z_T[l=l_{\tau_T}, m=f_{D_T}N\mathrm{T_S}] =&A_T\exp(-j2\pi\frac{v_R}{\lambda}\cos\alpha_T K\mathrm{T_S}) \\ &\cdot\sum_{n=0}^{N}\left(g_n^{\mathrm{MF}}[0]-\exp(j2\pi\frac{v_{B_T}}{\lambda}K\mathrm{T_S})g_{n-K}^{\mathrm{MF}}[0]\right) \end{aligned} \tag{3.24}$$

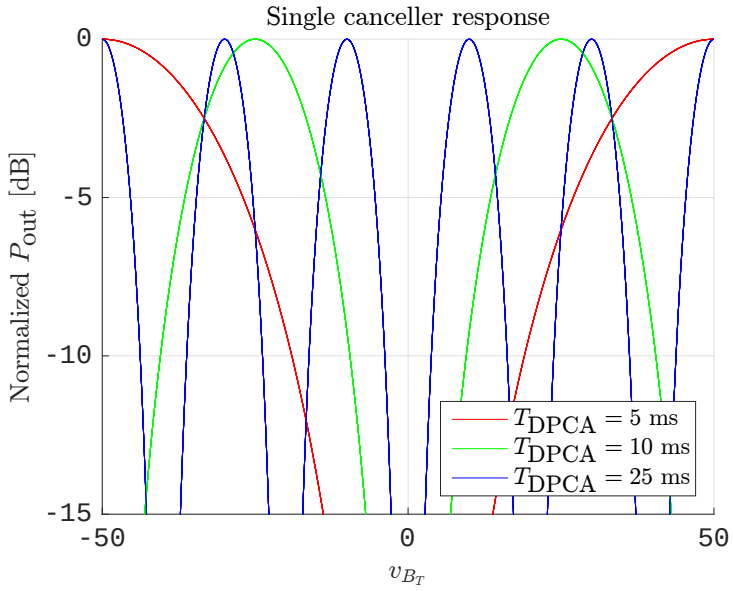

Fig. 3.6: Single canceller response for different $T_{\text{DPCA}} = K\text{T}_\text{S}$ times.

As the mean value of the random variable $g_n[l]$ is independent of n, the expectation value and the quadratic expectation value of (3.24) are given as:

$$\begin{aligned} E\{z_T[l = l_{\tau_T}, m = f_{D_T} N\text{T}_\text{S}]\} =& A_T \exp(-j2\pi \frac{v_R}{\lambda} \cos\alpha_T K\text{T}_\text{S}) N E\{g_0[0]\} \\ & \cdot \left(1 - \exp(2\pi \frac{v_B}{\lambda} K\text{T}_\text{S})\right) \end{aligned} \tag{3.25}$$

$$\begin{aligned} P_T^{(\text{MF})} &= |E\{z_T[l = l_{\tau_T}, m = f_{D_T} N\text{T}_\text{S}]\}|^2 \\ &= \left| A_T N E\{g_0[0]\} \exp(-j2\pi(\frac{v_R}{\lambda}\cos\alpha_T) - \frac{v_{B_T}}{\lambda} K\text{T}_\text{S}) 2j \sin\left(\pi \frac{v_{B_T}}{\lambda} K\text{T}_\text{S}\right) \right|^2 \\ &= |A_T|^2 N^2 |E\{g_0[0]\}|^2 \cdot 4 \left| \sin\left(\pi \frac{v_{B_T}}{\lambda} K\text{T}_\text{S}\right) \right|^2 \\ &\overset{(3.16)}{=} |A_T|^2 N^2 |\kappa L \sigma^2|^2 \cdot 4 \left| \sin\left(\pi \frac{v_{B_T}}{\lambda} K\text{T}_\text{S}\right) \right|^2 \end{aligned} \tag{3.26}$$

However, (3.26) is referred to as the Single Canceller Response (SCR) and its output is shown in Fig. 3.6. One observes that the highest gain of the output of (3.26) is for $v_{B_T} = \frac{\lambda(1+2k)}{2K\text{T}_\text{S}}$, $k \in \mathbb{Z}$, while the system will be blind for targets with some particular radial velocities (so-called "blind velocities") at $v_{B_T} = \frac{k\lambda}{K\text{T}_\text{S}}$, $k \in \mathbb{Z}$. For the simulated scenario in 3.2 and the case study here, blind velocities occur at $v_{\text{blind}} = k \cdot 49.6\,\text{m/s}$, which can be clearly seen in Fig. 3.4.

The shorter the duration T_{DPCA}, i.e. the faster the platform moves, the wider the filter notch becomes to suppress clutter returns spread in Doppler. Furthermore it is obvious that with longer durations of $T_{\mathrm{DPCA}} = K\mathrm{T_S}$ the system's capability to detect slow moving targets is enhanced (see the narrower filter notch in 3.6), but this would lead to an increased number of blind velocities occurring in the Doppler range of interest.

3.3.2 Multiple stationary point-like scatterers

In the following subsection a multitude of stationary point-like scatterers will be considered, i.e. clutter is simulated according to (3.6). It is assumed, that the clutter contributions from different clutter patches are statistically independent: $A_r(\alpha) \rightarrow \mathcal{CN}(0, \sigma_{Cr}^2)(\alpha)$. The range compressed outputs at the input of the cancellation stage is:

$$\begin{aligned} x_C^{(LA)}[l,n] &= \sum_{r=1}^{N_R} \int_{\Phi_r} A_r(\alpha) g_n[l - l_{\tau_r}] \exp\big(j2\pi \frac{v_P}{\lambda} \cos\alpha n T\big) d\alpha \\ x_C^{(TA)}[l,n] &= \sum_{r=1}^{N_R} \int_{\Phi_r} A_r(\alpha) g_n[l - l_{\tau_r}] \exp\big(j2\pi \frac{v_P}{\lambda} \cos\alpha n T\big) \exp\big(-j2\pi \frac{d}{\lambda} \cos\alpha\big) d\alpha \end{aligned} \tag{3.27}$$

Under consideration of the DPCA condition $d = v_R K \mathrm{T_S}$, the application of the cancellation stage leads to:

$$\begin{aligned} y_C[l,n] &= x_C^{(TA)}[l,n] - x_C^{(LA)}[l,n-K] \\ &= \sum_{r=1}^{N_{RC}} \int_{\Phi_r} A_r(\alpha) \left(g_n[l - l_{\tau_r}] - g_{n-K}[l - l_{\tau_r}]\right) \exp\big(2\pi j \frac{v_P}{\lambda} \cos\alpha (n-K) T\big) d\alpha \end{aligned} \tag{3.28}$$

and after a Doppler filter stage the output is:

$$\begin{aligned} z_C[l,m] =& \sum_n y_C[l,n] \exp(-j2\pi \frac{m}{NT} nT) \\ =& \sum_n \sum_{r=1}^{N_{RC}} \int_{\Phi_r} A_r(\alpha) \left(g_n[l-l_{\tau_r}] - g_{n-K}[l-l_{\tau_r}]\right) \\ & \cdot \exp\left(2\pi j \frac{v_P}{\lambda} \cos\alpha (n-K)T\right) d\alpha \exp(-2\pi j \frac{m}{NT} nT) \\ =& \sum_{r=1}^{N_{RC}} \int_{\Phi_C} A_r(\alpha) \exp(-j2\pi \frac{v_R}{\lambda} \cos\alpha K \mathrm{T_S}) \\ & \cdot \sum_n \left(g_n^{\mathrm{MF}}[l-l_{\tau_r}] - g_{n-K}^{\mathrm{MF}}[l-l_{\tau_r}] \right) \exp(j2\pi (\frac{v_R}{\lambda}\cos\alpha - \frac{m}{N\mathrm{T_S}}) n \mathrm{T_S}) d\alpha \end{aligned} \tag{3.29}$$

The clutter output power is evaluated as (for detailed equations refer to 8.B):

$$\begin{aligned} P_C^{(\mathrm{out})} =& E\left\{ |z_C[l,m]|^2 \right\} \\ =& 4N \mathrm{Var}\{g_0[l]\} \sum_{r=1}^{N_R} \int_{\Phi_r} \sigma_{Cr}^2(\alpha) \sin^2\left(\pi \frac{m}{NT} KT - \frac{d}{\lambda}\cos\alpha\right) d\alpha \\ =& 4N \mathrm{Var}\{g_0[l]\} \sum_{r=1}^{N_R} \int_{\Phi_r} \sigma_{Cr}^2(\alpha) \sin^2\left(\pi \left(\frac{m}{NT} - \frac{v_R}{\lambda}\cos\alpha\right) KT\right) d\alpha \end{aligned} \tag{3.30}$$

Analysing (3.30), one can see, that there is a superposition of contributions from clutter patches on one particular range-Doppler bin. The contribution from the clutter patches comes from all considered range cells, which is encoded in the summation, and from all angles (i.e. direction of arrival), which is encoded in the integral. Each contribution undergoes an attenuation, which is encoded in the term $\sigma_{Cr}(\alpha)$, therefore being dependent on the angle of arrival α, and on the particular range cell r. The term $\sigma_{Cr}(\alpha)$ is modulated by the $\sin^2$ shape. Analysing the $\sin^2$ shape tells, that the contribution of a particular delay-Doppler cell equals zero at that Doppler frequency f_D, which corresponds to the Doppler frequency of itself: $f_D = \frac{m}{NT} = \frac{v_R}{\lambda}\cos\alpha$. That means, that a particular delay-Doppler cell $z_C[l_{\tau_0}, m_0]$ does not contribute to delay-Doppler cells, that are modulated with the same Doppler frequency $f_D = m_0 N/\mathrm{T_S}$. However, the delay-Doppler cell $z_C[l_{\tau_0}, m_0]$ contribution increases for delay-Doppler bins, which are further distant to $z_C[l_{\tau_0}, m_0]$ in terms of angle α. The contribution reaches its maximum for $\cos\alpha = \frac{\lambda}{v_R}\left(\frac{m}{N\mathrm{T_S}} - \frac{1}{2K\mathrm{T_S}}\right)$, and the power level of the contribution depends only of the term $\sigma_{Cr}^2(\alpha)$ (which includes the propagation loss, reflectivity, and the TX and RX antenna gains).

Omnidirectional antennas and homogeneous clutter within each range cell For the transmit antennas an omnidirectional pattern in azimuth can be assumed. This is a reasonable assumption, as the operators of broadcast stations intend to cover a large area around the TX in order to provide television coverage to the customers. The pattern of the receive antennas is depending on the exploited type of antennas. However, to achieve a broad coverage and large area monitoring, usually omnidirectional antennas are used. Therefore, the term $\sigma_{Cr}(\alpha)$ is mainly dependent on the reflectivity of the particular clutter patch and on propagation losses.
Keeping this in mind, equation (3.30) can further be developed under the following simplifying assumptions that:

- Very wide beam antennas (or equivalently omnidirectional antennas) are employed.
- Homogeneous clutter returns are experienced within each range cell, which yields $\sigma^2_{Cr}(\alpha) = \sigma^2_{Cr}$. It must be mentioned, that:
  - Such condition requires the direct signal from the TX to have been already suppressed, e.g. using [37].
  - This assumption cannot be strictly verified in a bistatic geometry as the Cassini's ovals intersect the bistatic range cells, so that the free-space propagation loss cannot be constant within each range cell.

Then, (3.30) becomes (for the detailed derivation refer to App. 8.C):

$$\begin{aligned} P_C^{(\text{out})}[l,m] =& 2N\kappa^2 L\sigma^2(\mu-1)P_C^{(\text{in})} \\ & \cdot\left\{1-\cos\left(2\pi\frac{m}{N}K\right)J_0\left(2\pi\frac{d}{\lambda}\right)\right\} \end{aligned} \tag{3.31}$$

$J_0(x)$ defines the Bessel function of the first kind of order zero and $P_C^{(\text{in})}$ is the global clutter power at the input of the system. $P_C^{(\text{in})}$ can be written as:

$$P_C^{(\text{in})} = E\left\{\left|r_C^{(\alpha)}[l]\right|^2\right\} = \pi\sigma^2\sum_{r=1}^{N_R}\sigma^2_{Cr} \tag{3.32}$$

For a fair comparison of the power levels between the input and the output of the processing scheme of Fig. 3.2, the multiplicative constant κ is chosen to provide unitary gain when only thermal noise as input of the processing scheme for the matched filter is considered. For κ this yields: $\kappa = \frac{1}{\sqrt{2NL_S\sigma^2\sigma^2}}$ (for the derivation

see App. 8.D) and (3.31) becomes:

$$P_C^{(\text{out})}[l,m] = (\mu-1)P_C^{(\text{in})}\left\{1-\cos\left(2\pi\frac{m}{N\mathrm{T_S}}K\mathrm{T_S}\right)J_0\left(2\pi\frac{d}{\lambda}\right)\right\} \tag{3.33}$$

Analysing (3.33) leads to two conclusions:

(i) The clutter output power varies around the average value of $(\mu-1)P_C^{(\text{in})}$. As μ is dependent on the constellation map (see (3.16)), the output power depends as well on the constellation map: for 16-QAM and 64-QAM μ is given as 1.32 and 1.38, respectively, which leads to a value of 4.9 dB and 4.2 dB below the clutter input power for the output power. For QPSK the output power becomes zero, as $\mu = 1$. However this is the result of neglecting the deterministic components, and in practice a lower bound on this average power level will be experienced, even in the QPSK case.

(ii) The last factor $\left\{1-\cos\left(2\pi\frac{m}{N\mathrm{T_S}}K\mathrm{T_S}\right)J_0\left(2\pi\frac{d}{\lambda}\right)\right\}$ varies in the interval from $(0,2)$. However, for the employed simulation where $d = \lambda/2$, the factor is in the interval $[0.7, 1.3]$. This means, that the output power of each Doppler bin varies according to this factor across all range gates. The factor $\cos(2\pi\frac{m}{N\mathrm{T_S}}K\mathrm{T_S})$ is dependent on the DPCA time shift $T_{\text{DPCA}} = K\mathrm{T_S} = d/v_R$. This means, that there is a sinusoidal pattern, where its period depends on $2\pi\frac{m}{N\mathrm{T_S}}\frac{d}{v_R}$. The average value is as stated in (i) depending on the constellation map. The sinusoidal pattern is visible in Fig. 3.4.
It can be noted, that the DPCA delay time can not be adapted to let this factor become zero, as $J_0(x) < 1$ for $x \neq 0 \Rightarrow \frac{1}{J_0(x)} > 1 \geq \cos(2\pi kK/N)$.

To compare the output of (3.33) to the outcome of Fig. 3.4, the expected theoretical result of (3.33) is plotted in Fig 3.7 along with the estimated mean value for all Doppler bins for an extended range shown in Fig. 3.4. The minima and the maxima, as calculated from (3.33), have a difference $\Delta_{P_{\text{out}}} = 10\log_{10}(1.3/0.7) \approx 2.7\,\text{dB}$, which is well in line with the results from Fig. 3.7.
Additionally one observes the modulation due to the DPCA delay time in Doppler dimension with period $f_P = \frac{1}{K\mathrm{T_S}} \approx 99\,\text{Hz}$.

DPCA cancellation ratio for MF So far the DPCA performance was analysed under the background of the residuals (sidelobes, etc.) resulting from the range compression. However, DPCA is an effective clutter cancellation stage, although being limited here by the range compression residuals. Therefore it is worth to analyse how the clutter cancellation performs, despite the fact, that it is not able

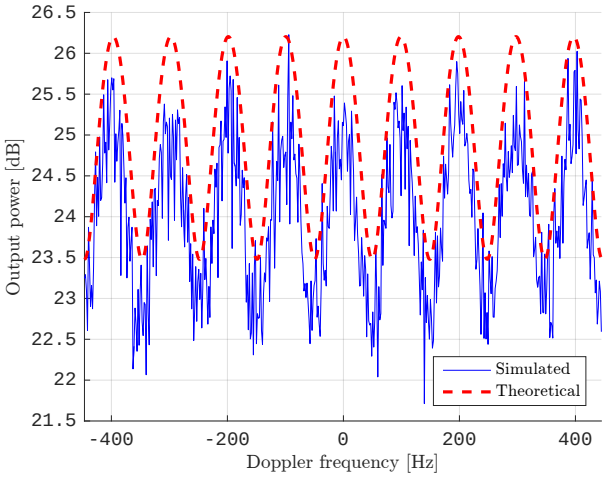

Fig. 3.7: Clutter output power in dB versus Doppler frequency [Hz] after matched filtering and DPCA. The expected theoretical result from (3.33) is compared to the estimated mean value of Fig. 3.4. The employed constellation map was 16-QAM.

to remove the clutter residuals in exo-clutter region, which as well result from the matched filtered processing. The cancellation ratio CR$[l, m]$ is given as:

$$\mathrm{CR}[l, r] = \frac{P_C^{\mathrm{LA}}[l, m]}{P_C^{(\mathrm{out})}[l, m]} \tag{3.34}$$

The term $P_C^{\mathrm{LA}}[l, m]$ refers to the clutter power at the delay-Doppler bin $[l, m]$ without DPCA processing. That is, directly at Fig. 3.3. The Doppler filtered output becomes:

$$z_C^{(\mathrm{LA})}[l, m] = \sum_{r=1}^{N_R} \int_{\Phi_r} A_r(\alpha) \sum_{n}^{N_{\mathrm{CPI}}} g_n^{(\mathrm{MF})}[l - l_{\tau_r}] \exp\left(j2\pi \left(\frac{v_R}{\lambda}\cos\alpha - \frac{m}{N\mathrm{T_S}}\right) n\mathrm{T_S}\right) d\alpha \tag{3.35}$$

The output power is then:

$$\begin{aligned} P_C^{(\mathrm{LA})}[l, m] =& E\left\{\left|z_C^{(\mathrm{LA})}[l, m]\right|^2\right\} \\ =& (\mu - 1) P_C^{(\mathrm{in})} \\ &+ L\sigma^2 \sum_{r}^{N_R} \int_{\Phi_r} \sigma_{Cr}^2 \delta[l - l_{\tau_r}] \frac{1}{N} \left|\mathrm{dsinc}\left[\pi \left(\frac{v_R}{\lambda}\cos\alpha - \frac{m}{N\mathrm{T_S}}\right) \mathrm{T_S}, N\right]\right|^2 d\alpha \end{aligned} \tag{3.36}$$

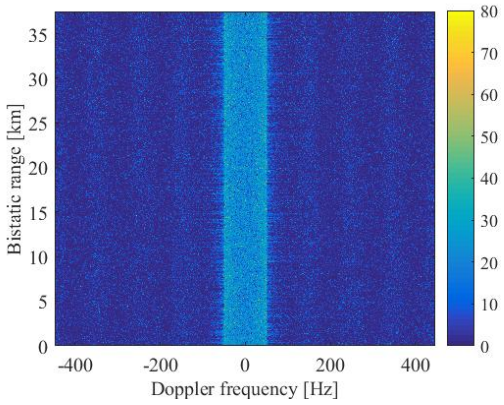

Fig. 3.8: Cancellation ratio as a function of the delay-Doppler bin for the case study considered in Fig. 3.3 and Fig. 3.4.

Eq. (3.36) is the summation of two terms. The first one $(\mu - 1)P_C^{(\text{in})}$ is dependent on the input clutter power and is constant for the complete range-Doppler map. It is a noise background and results from the matched filtering. It can be seen in Fig. 3.3 outside the main clutter ridge. Usually it is smaller than the second term, but still increases the uncorrelated noise level, thus limiting target detection.
The second term represents the non-negligible contribution of scatterers to the main clutter ridge. The width of the clutter ridge is defined by the pattern of the employed antenna elements, which shows in the factor $\frac{v_R}{\lambda}\cos\alpha$. For the assumption of antenna elements omnidirectional in azimuth the factor reduces to $\cos\alpha = 1$.
However, the conclusion drawn in Sec. 3.3.2, holds here as well: The main contribution from other delay-Doppler bins on one particular delay-Doppler bin results only from delay-Doppler bins from the same range cell, but not from the same Doppler bin.
In Fig. 3.8 the cancellation ratio between Fig. 3.3 and Fig. 3.4 is shown. The main clutter ridge appears to be filtered out, but the mean value is below 40 dB, thus far from the ideal cancellation ratio of being infinite. Furthermore, the suppression in exo-clutter region is not significant, just around 0 dB, as the compressed OFDM symbols from both receiving channels are not correlated, therefore not being suppressed.

Implications for STAP as clutter filter To this end, DPCA was regarded as clutter filter, and the concatenation of two stages, namely MF and DPCA, were analysed. The implications when using the MF were shown in detail. However, the analysis shows also that there is a constant noise background depending on

the clutter input power $P_C^{(\mathrm{in})}$, which increases the noise level. But there are as well contributions from delay-Doppler bins on one particular delay-Doppler bin, which is potentially very distant from the delay-Doppler bins, from which the contributions are originating. That is, one particular delay-Doppler bin contributes with its statistical backscatter coefficient on one delay-Doppler bin, which has likely a different backscatter coefficient, depending among others on the variety of the landscape and the observed scene.
As mentioned in Sec. 2.3, STAP, e.g. *Adjacent-bin post-Doppler STAP* [20], is adaptive on the clutter returns and estimates, based on a covariance matrix from secondary data, a weight vector $\mathbf{w}$ to be applied as filter. The secondary data are usually taken from delay-Doppler bins close to the delay-Doppler bin under test $z_{\mathrm{UT}}[l, m]$ (with a guard-interval between secondary data and $z_{\mathrm{UT}}[l, m]$), as these are assumed to reflect the statistical properties of $z_{\mathrm{UT}}[l, m]$. Therefore this processing is adaptive in order for $\mathbf{w}$ to filter out the clutter returns. Applying STAP on a matched filtered range-Doppler map as in (3.35) means, that a weight vector $\mathbf{w}$ is estimated based on secondary data, which might not reflect the statistics of the delay-Doppler bin to be filtered, due to contributions from distant range-Doppler bins. Therefore it can be expected that the clutter suppression performance is as well limited if the DPCA stage is exchanged in lieu of a STAP application.

Conclusion DPCA is an effective processing scheme when it comes to clutter suppression. However, the clutter contribution of a stationary point-like scatterer is not cancelled at the delay-Doppler bin where its output is expected, see (3.19) and (3.23) and Sec. 3.3.1. Furthermore, a particular point-like scatterer contributes with a non-negligible power level to all range-Doppler cells, thus increasing the level of the uncorrelated noise floor, which will not be removed by DPCA.
Therefore this processing chain is not effective, where the limiting factor is the application of the MF for range compression of the uncontrollable transmitted waveform.

3.4 Reciprocal Filter

The reason for the residual noise floor on the range-Doppler map, which prevents target detection, was referred to the time-varying content of the waveform: the payload data changes from OFDM symbol to symbol, and therefore the crucial condition of time-invariant pulses (as for an active radar) is not fulfilled here. As it is not possible to control the transmitted signal , the processing of the received waveform needs to changed. A method to remove the time-varying content is obviously provided by the so-called RpF, which is basically a division of the received signal by the reconstructed copy of the transmitted signal. Although originally

introduced in [33] in order to control the level of unwanted sidelobes, it is effective in providing a time-invariant impulse response. Applying the RpF equalizes the symbol and cancels the information content. Therefore a time-invariant impulse responses can be achieved and thus it serves as adequate input for the DPCA clutter cancellation stage.
From (3.9) the RpF is written as follows:

$$h_n[l] = h_n^{\mathrm{RpF}}[l] = \kappa' \mathrm{IDFT}\{S_n[m]^{-1}\} \tag{3.37}$$

The impulse response is then:

$$g_n^{(\mathrm{RpF})} = s_n[l - nL_S] * h_n^{(\mathrm{RpF})}[l] = \kappa' \mathrm{IDFT}\{\mathrm{rect}[k]\} = \kappa' L_S \delta[l] \tag{3.38}$$

In Fig. 3.9 the output of the RpF is reported. The high peaks and the constant noise floor have been removed, such that the impulse response is a digital sinc function, which is typical for signals with a flat spectrum. Clearly, due to the

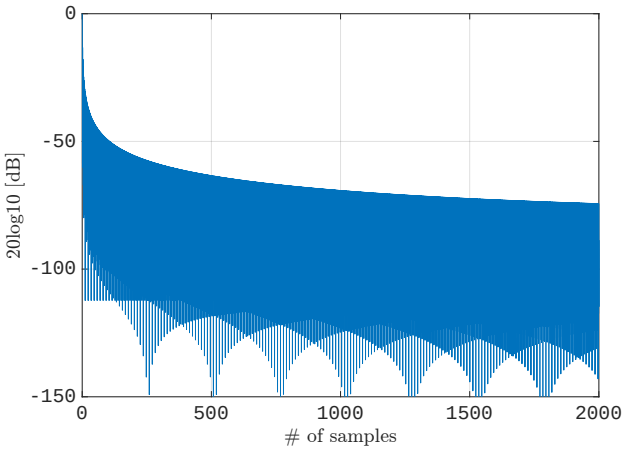

Fig. 3.9: Impulse response of one reciprocal filtered DVB-T symbol.

removal of the waveform content, the impulse response is now time-invariant for each symbol, i.e.:

$$g_n^{(\mathrm{RpF})} = g_p^{(\mathrm{RpF})} = \kappa' L_S \delta[l], \ \forall \ n, p \tag{3.39}$$

In order to avoid the issues due to overweighting possibly caused by the division by small or zero values [33], the application of the RpF is limited to non-zero subcarriers (i.e. the data- and pilot carriers). The guard carriers are excluded from the processing. Furthermore, it needs to be noted, that a division by zero (or by very small values) in practical applications will not happen, as all the data subcarriers

are forced to represent a constellation symbol in the constellation map during the processing, therefore having a non-zero value, see Sec. 2.2.2. As the positions and the values of the pilot carriers are known, they as well have a non-zero value.
In conclusion, the RpF provides an impulse response, which is deterministic and time-invariant.

3.4.1 Single point-like scatterer

The output for a single point-like scatterer will be analysed. Recalling (3.12) and substituting in (3.18) $g_n^{(\mathrm{MF})}$ with the impulse response for the RpF $g_n^{(\mathrm{RpF})}$ from (3.38), the Doppler-filtered outputs at the end of the processing stage are:

$$\begin{aligned}\bar{z}_0[l,m] =& A_0 \exp(-j2\pi\frac{v_R}{\lambda}\cos\alpha_0 K\mathrm{T_S}) g_0^{(\mathrm{RpF})}[l-l_{\tau_0}] \\ &\cdot 2j\sin\Big(\pi\frac{v_B}{\lambda}K\mathrm{T_S}\Big)\mathrm{dsinc}\big[\pi\left(f_{D_0}-\frac{m}{N\mathrm{T_S}}\right)\mathrm{T_S}, N\big]\end{aligned} \tag{3.40}$$

which is similar to the statistical expression of the output obtained for the MF (see (3.20)). The output of a stationary object $v_B = 0$ would become zero, therefore being perfectly suppressed. Furthermore, there is no contribution of a single point scatterer on other delay-Doppler cells, which is a substantial improvement compared to the MF case, compare to (3.19) and (3.29).
The output peak power P_T for a moving target echo, measured at its expected range-Doppler location, i.e. $l = \lambda_T\tau_0$ and $\frac{m}{N\mathrm{T_S}} = f_{D_0}$, can be evaluated as:

$$\begin{aligned}P_T^{(\mathrm{RpF})} =& \big|E\{z_T[l_{\tau_0}, N\mathrm{T_S}f_{D_0}]\}\big|^2 \\ &\cdot 4|A_0|^2N^2\kappa'^2L^2\big|\sin\Big(\pi\frac{v_B}{\lambda}K\mathrm{T_S}\Big)\big|^2\end{aligned} \tag{3.41}$$

where (3.38) has been used. The constant κ' is chosen such that at the outcome unitary gain is provided, in the case for thermal noise only as input signal, as was done for the MF evaluation, compare App. 8.D. For κ' it is obtained: $\kappa' = \frac{\sigma^2}{\sqrt{2NL_S\xi\sigma_N^2}}$, where ξ depends on the constellation map: $\xi = \frac{1}{M_C}\sum_0^{M_C-1}\frac{1}{|c_m|^2}$. As the same scaling strategy for MF and RpF was used, the output power level for a single point-like scatterer at its expected position l_{τ_0} and f_{D_0} can be directly compared. Comparing (3.26) to (3.41) leads to:

$$\Delta P_T = \frac{P_T^{(\mathrm{MF})}}{P_T^{(\mathrm{RpF})}} = \frac{\kappa^2L_S^2\sigma_s^4}{\kappa'^2L_S^2} = \xi \tag{3.42}$$

This results represents the loss in SNR one can expect when replacing the MF with the RpF. The expected loss is only dependent on the constellation map, which is a

given from the TX. For the three possible values of QPSK, 16-QAM and 64-QAM this can be evaluated as: $\xi = [0, 2.76, 4.29]\,\mathrm{dB}$ for $M_C = [4, 16, 64]$. Apparently, no loss is observed for the QPSK case. The reason for this is that transmissions using the QPSK constellation map, exhibit a rather flat spectral density, at least as long as only data carriers are regarded. The pilot carriers are transmitted at boosted power level, which might yield to an additional small loss. The transmissions using 16/64-QAM are more common, and then a loss in SNR has to be accepted, which is up to 4.3 dB for 64-QAM.
However, this loss needs to be compared to an improvement in terms of residual noise floor and ambiguity suppression, which can be expected from using the RpF. To analyse this, first it is observed, that (3.40) equals zero for a stationary scatterer, i.e. $v_B = 0$, under the assumption of ideal conditions, which are no ICM or amplitude fluctuations, and fulfilment of the DPCA condition. Clearly, from (3.40) and (3.41) it results, that there is no contribution from one stationary scatterer on any range-Doppler bin on the range-Doppler map.

3.4.2 Multiple stationary point-like scatterers

For a superposition of clutter echoes from multiple scatterers according to (3.6) the output power becomes at the end of the processing chain equally to zero:

$$P_C^{(\mathrm{out})}[l, m] = 0 \tag{3.43}$$

In other words, by equalizing the specific signal fragment, the same condition is restored at the output of the range compression as for the case of an active radar employing a periodic waveform composed by a train of identical pulses. This allows achieving a perfect clutter cancellation under ideal conditions:

$$\mathrm{CR} \to \infty \tag{3.44}$$

The results when replacing the MF with the RpF are shown in Figs. 3.10 (before DPCA processing) and 3.11 (after DPCA processing) exemplarily. The same simulation parameters hold as for the simulations when using the MF.
Comparing Fig. 3.3 to Fig. 3.10 it can be seen that even before applying the clutter cancellation stage, a significant higher dynamic range is achieved for the RpF at exo-clutter regions. This means, targets experiencing a bistatic Doppler higher than the maximum of the clutter Doppler frequency: $f_{D_T} > \frac{v_R}{\lambda}$ might already be detected without clutter removal. However, the clutter, visible in Fig. 3.10, still blinds the systems for weak and slow moving targets. The peak value of the clutter ridge is at 58.61 dB, which is approximately 2.85 dB below the clutter peak power for MF application, visible in Fig. 3.3. This loss in SNR results from the employed

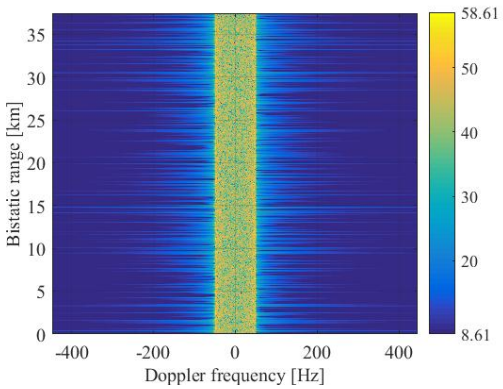

Fig. 3.10: Range-Doppler map in dB for RpF before DPCA processing for a simulated scenario including clutter echoes only.

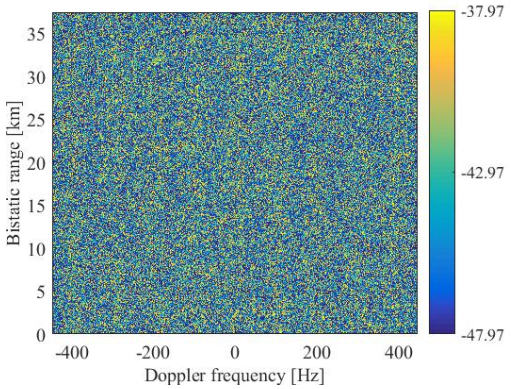

Fig. 3.11: Range-Doppler map in dB for RpF after DPCA processing for a simulated scenario including clutter echoes only.

constellation map of 16-QAM used for the simulations. It is in accordance with (3.42), and holds for single stationary and multiple stationary scatterer returns as well as for a single target return, as both MF and RpF are linear filters, and target returns are formulated in the same manner as clutter returns. However, based on the results in [35], this advantage of the RpF might reduce for a highly Doppler spread clutter.
Finally DPCA is applied, whose output is reported in Fig. 3.11. Clearly, the advantage and benefits are visible, compared to Fig. 3.4. The clutter is completely removed, while the fluctuations are due to noise coming from border effects. The clutter cancellation is therefore only limited by noise present in the receiving system.

3.4.3 Comparison of SCNR between MF and RpF

As shown in (3.40) the clutter returns are perfectly suppressed leading to a cancellation ratio approaching infinite, provided absence of ICM and DPCA fulfilment. In Fig. 3.12 the cancellation ratio evaluated between the range-Doppler maps of Fig. 3.10 and Fig. 3.11 is reported. With either the RpF and the MF, the main clutter ridge has been effectively removed, thanks to the DPCA approach thus allowing the potential detection of endo- clutter targets. In the RpF case, the cancellation ratio values obtained in the endo-clutter region are well above 80 dB (the figure has been upper limited to be directly compared to Fig. 3.8). Furthermore, cascading the RpF and the DPCA approach, the average level of the residual clutter contributions across the whole delay/Doppler map has been significantly

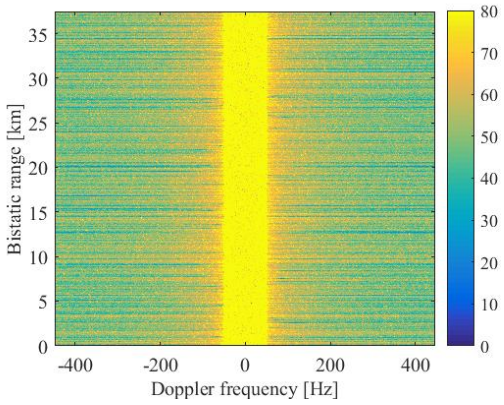

Fig. 3.12: Cancellation ratio in dB as range-Doppler map. Evaluated between the range-Doppler maps of Fig. 3.10 and Fig. 3.11.

reduced, thus improving the sensitivity of the radar against both fast and slowly moving targets. In fact, the average background level moves from about 24.6 dB in Fig. 3.4 to –43 dB in Fig. 3.11. Correspondingly, cancellation ratio values in the range 40–60 dB are also obtained in the exo-clutter region. It can be observed that a non-zero average level is obtained in Fig. 3.11 being that value lower bounded by numerical errors and border effects at the range compression stage. In practice, this residual power level is well below thermal noise.
As apparent, the cascade of the RpF and the DPCA processing ideally provides a perfect cancellation of the echoes from the stationary scene at the price of a limited loss in terms of the SNR due to the filter mismatch at the compression stage. In contrast, cascading the MF and the DPCA approach yields the highest SNR output value being the detection performance possibly limited by the clutter residual power level at the output of the cancellation stage.
In order to jointly consider these effects, the output Signal-to-clutter-and-noise Ratio (SCNR) across the range-Doppler map can be studied:

$$\mathrm{SCNR}_{\mathrm{MF\ \&DPCA}}[l,m] = \frac{P_T[l = l_{\tau_0}, m = N\mathrm{T_S} f_{D_0}]}{P_C^{(\mathrm{out})}[l,m] + 1} \tag{3.45}$$

Both the noise input power and the corresponding gain were set to unity, therefore a unitary power level for the noise at the output of the processing chain is given. With the results so far, one can write:

$$\mathrm{SCNR}_{\mathrm{MF\ \&DPCA}}[l,m] = \frac{|A_0|^2 N L_S \sigma_s^2 \left|\sin\left(\pi \frac{v_B}{\lambda} K \mathrm{T_S}\right)\right|^2}{(\mu-1) P_C^{(\mathrm{in})} \left\{1 - \cos\left(2\pi \frac{m}{N} K\right) J_0\left(2\pi \frac{d}{\lambda}\right)\right\} + 1} \tag{3.46}$$

$$\mathrm{SCNR}_{\mathrm{RpF\ \&DPCA}}[l,m] = |A_0|^2 N \zeta^{-1} L_S \sigma_s^2 \left|\sin\left(\pi \frac{v_B}{\lambda} K \mathrm{T_S}\right)\right|^2 \tag{3.47}$$

A comparison leads to:

$$\begin{aligned}\Delta S[l,m] &= \frac{\mathrm{SCNR}_{\mathrm{RpF\ \&DPCA}}[l,m]}{\mathrm{SCNR}_{\mathrm{MF\ \&DPCA}}[l,m]} \\ &= \frac{(\mu-1)P_C^{(\mathrm{in})}\left\{1-\cos\left(2\pi\frac{m}{N}K\right)J_0\left(2\pi\frac{d}{\lambda}\right)\right\}+1}{\zeta}\end{aligned} \tag{3.48}$$

All variables can be regarded as constants, while only the input power varies. The input power is equal to the clutter power: $P_C^{(\mathrm{in})} = \mathrm{CNR}^{(\mathrm{in})}$. Under these considerations, (3.48) shows that for the RpF to outperform the MF, the Clutter-to-noise Ratio (CNR) must be above a certain threshold. If stating that $\Delta S[l,m] > 1$, then:

$$\mathrm{CNR}^{(\mathrm{in})} > \frac{\zeta-1}{(\mu-1)\left\{1-\cos\left(2\pi\frac{m}{N}K\right)J_0\left(2\pi\frac{d}{\lambda}\right)\right\}} \tag{3.49}$$

This means, that the CNR must be above a certain threshold in order for the RpF to provide better results in terms of target detection and clutter suppression. The threshold for the reciprocal filtering stage to achieve a higher SCNR results is dependent of the employed constellation map and of the inter-element spacing d. Assuming that $d = \lambda/2$, then following threshold levels can be expected:

$$\begin{aligned}&\mathrm{CNR}^{(\mathrm{in})} > \mathrm{inf} && M_C = 4 \\ &\mathrm{CNR}^{(\mathrm{in})} > 6.0\,\mathrm{dB} && M_C = 16 \\ &\mathrm{CNR}^{(\mathrm{in})} > 8.0\,\mathrm{dB} && M_C = 64\end{aligned} \tag{3.50}$$

While for the QPSK case ($M_C = 4$) such improvement can not be expected, the clutter cancellation stage of the RpF provides a significant advantage for 16-/64-QAM values for CNR values higher than 6/8 dB.
However, here in the simulations it was first assumed, that the reference signal was ideally reconstructed. Second, another assumption is the fulfilment of the DPCA condition, and third, the influence of ICM was neglected and calibrated hardware was assumed.
The reconstruction of the reference signal depends on the SNR of the direct signal. As long as the SNR is above a certain level, the reconstruction is generally possible, this holds as well for fast moving platforms [12],[14]. Beside of that, the correlation using a non-ideal reference signal would lead to incorrect correlation results for both RpF and MF, therefore the advantage of reciprocal filtering still holds.
A violation of the DPCA condition is addressed in Sec. 5.1, where the influence and a possibility to overcome these limitations will be shown. Issues due to missing

calibration and a method to calibrate on the direct signal are addressed in Sec. 5.2. The effects of ICM have been largely investigated in literature also for the case of conventional active radar and is therefore not considered in the simulations. Nevertheless, when the results against experimental data are reported, ICM is unavoidably included.

To justify the advantage of using reciprocal filtering, the analysis is further extended. In the first analysis, the target's bistatic Doppler frequency is changed in the range of $f_{D_T} = [0, \ldots, \frac{\mathrm{PRF}}{2}]$ and for each f_{D_T} the SCNR is evaluated. The SCNR is evaluated by dividing the target's peak power level by the clutter power level in an extended range around the target's range-Doppler bin. The target's echo is assumed to impinge the antennas from an angle $\alpha_G = \frac{\pi}{2}$, so that its bistatic Doppler frequency is only dependent on its velocity v_G. The CNR and the SNR are set to 30 dB and to -30 dB.

Furthermore, the receiver was flying with a velocity of $v_R = 24.53\,\mathrm{m/s}$, which means, the requirement of the DPCA condition is not fulfilled. However, by exploiting an approach, which is referred to as "flexible DPCA" and in detail described in Sec. 5.1, the required DPCA condition can be re-established by means of digital signal processing. This approach is applied here for the evaluation.

The processing chain is evaluated once for the RpF, and once for the MF. The result is shown in Fig. 3.13. Both curves show the expected decay as the target bistatic velocity approaches $\frac{\lambda}{K\mathrm{T_S}}p,\ p \in \mathbb{Z}$. However, at each Doppler value, the proposed approach allows a SCNR improvement of about 20 dB, thanks to the enhanced capability to remove clutter echoes in the final map. This is clearly apparent from Fig. 3.14, where the ratio ΔS is reported of the SCNR results in Fig. 3.13. The ΔS curve largely matches the theoretical expectation based on (3.48) despite small fluctuations are present due to the local estimation of the clutter+noise power level at different Doppler bins of the map.

It should be noticed that this improvement might be upper-bounded by the noise level since, for small CNR values, the SCNR at the output of the processing stages will be dominated by the output SNR that is only slightly higher when exploiting the MF with respect to the RpF (being the advantage dependent on the adopted modulation scheme). This effect was illustrated in (3.46)-(3.48) and is shown in Fig. 3.15 where the output SCNR curves are reported as functions of the CNR at the input of the system for a fixed target Doppler value equal to -30 Hz. For CNR values below 5-6 dB the advantage of the proposed processing scheme disappears. Interesting enough, according to (3.42), a loss of 2.76 dB has to be accepted in term of output SCNR due to the exploitation of the RpF in lieu of the MF at the range compression stage. In contrast, as the CNR increases, the RpF followed by clutter suppression stage outperforms the MF and clutter suppression approach.

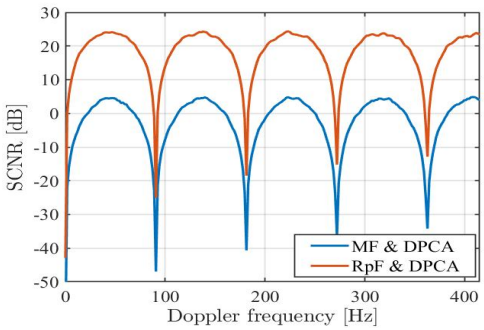

Fig. 3.13: Performance comparision: SCNR vs. target Doppler frequency for RpF (red line) and MF (blue line) after clutter suppression application.

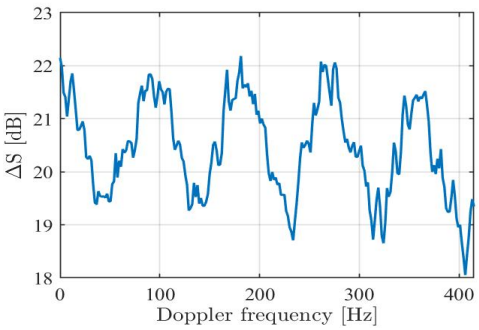

Fig. 3.14: SCNR ratio corresponding to Fig. 3.13.

3.5 Conclusion

The detailed analysis for the MF in Sec. 3.3 has shown that the MF creates time-variant impulse responses for each range-compressed OFDM symbol. Due to this time-variance, a subsequent clutter suppression stage, e.g. DPCA, is not able to remove the clutter returns completely, thus limiting target detection in endo-clutter region. In exo-clutter region the target detection is as well limited due to contributions from the range-compressed return of any point-like scatterer on other delay-Doppler cells.
In contrast, replacing the MF with the RpF leads to a remarkable improvement in terms of SCNR at the output of the processing stage, which is due to achieving a time-invariant impulse response of the range-compressed OFDM symbols. Although the RpF does not provide maximum SNR of a single range-compressed OFDM symbol (which is achieved by the MF) in terms of communication signal processing, it is the better choice for clutter suppression for moving target detection for passive radar on moving platforms.

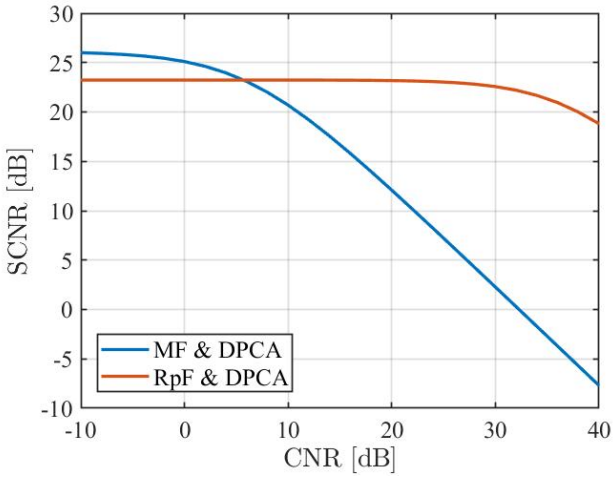

Fig. 3.15: Performance comparision: SCNR vs. CNR for RpF (red line) and MF (blue line) after STAP application.

Chapter 4

Trials and experiments

In order to show the performance of the RpF and to compare it to the analysis and simulations, two trials were conducted. The first trial was done in 2016 in Norway, and will be described in Sec. 4.2 together with the achieved results. The second trial was done in 2018 in Germany, and will be described in Sec. 4.3 together with the achieved results.
For all the results, a technique to cope with the non-fulfilment of the DPCA condition is applied. This technique is referred to as *flexible DPCA* or short *flex-DPCA* and is described in Sec. 5.1.
Furthermore for the data evaluation in Sec. 4.2.2 a technique to overcome missing calibration of the receiving channels is applied. This technique is called *Single Range-Doppler Bin (SRDB)* calibration. It is based on exploiting the direct signal, and described in more detail in Sec. 5.2.2. It is compared to digital calibration not being applied and to a second digital calibration technique in Sec. 5.2.5.

4.1 Hardware

For the trials the hardware equipment of the department Passive Radar And Anti-Jamming Techniques (PSR) of Fraunhofer FHR was used. The department has developed a two-channel receiving system, which is called *Parasol* [38]. It consists of two double-superheterodyne receivers, double in the sense, that two local oscillators are used instead of commonly one, which down convert the Radio Frequency (RF) to an Intermediate Frequency (IF) in the range of 64-96 MHz. At these frequencies two 16-bit Analog-to-digital Converters (ADCs) sample the IF with a sampling rate of 64 MHz per channel. As the real and imaginary part of the received signal are not sampled separately, the imaginary part of the signal is estimated using a Hilbert transformation. This leads to an effective bandwidth of 32 MHz. Due to 16 Opteron processors and one Stratix IV FPGA the Parasol sys-

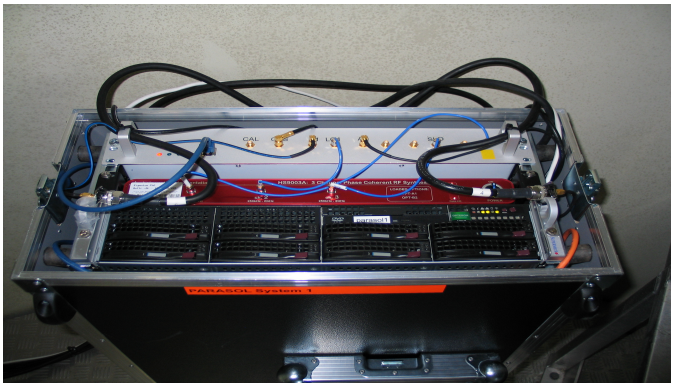

Fig. 4.1: The Parasol system.

tem is able to do in principle a real-time processing up to detection and tracking of targets in range-Doppler and Cartesian domain. However the Parasol system was used for data collection only, and data evaluation was done offline using Matlab. A picture of the system is shown in Fig. 4.1.

4.2 Experiment 1: Sea-borne platform

The first trial was done in September 2016 under cooperation with the Norwegian Defence Research Establishment – *Forsvarets forskningsinstitutt* (FFI). It took place in the Oslo fjord, the measurements lasted for three days. Two stationary RXs and one moving RX came into operation. The stationary systems were the LORA-11 and the Atlantis system from FHR and the system from FFI, who have a duplicated version of the system. For the moving platform a boat was used, which was supposed to cruise in the Oslo fjord on predefined trajectories. As receiving hardware two Parasol units (see 4.1) were used, which leads in total to four receiving channels. The antenna elements were changed regularly in order to test different configurations and setups, which means logarithmic-periodic (Log-per) and discone antennas were used in changing numbers, configurations, and polarisations.

The Figs. 4.2 and 4.3 show the Nøkken boat and the surveillance array with three discone elements. A map of the Oslo fjord is shown in Fig 4.4.

The TXs in the trial's vicinity transmit DVB-T signals on centre frequencies $f_T = [650, 658]\,\mathrm{MHz}$. The length T_G of one DVB-T symbol is $T_G = 1008 \cdot 10^{-6}\,\mathrm{s}$, i.e. the cyclic prefix T_Δ amounts $T_\Delta = \frac{1}{8}T_U = 112 \cdot 10^{-6}\,\mathrm{s}$. The employed constellation map is 64-QAM.

Fig. 4.2: The boat Nøkken used for the trials.

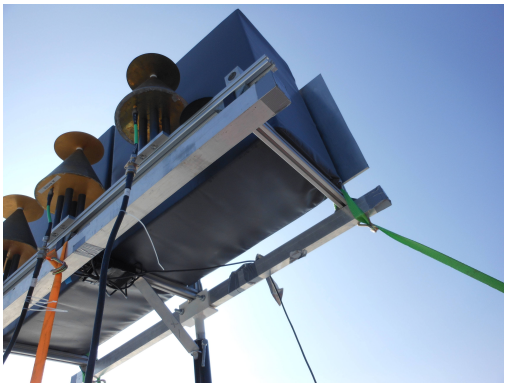

Fig. 4.3: The array with three discone elements with RAM at one side.

4.2.1 Ground truth

As ground truth the emitted Automatic Dependent Surveillance – Broadcast (ADS–B) signals of planes and the Automatic Identification System (AIS) signals of boats and vessels were recorded. After decoding of the signals the recorded positions can be remapped to detections in range-Doppler maps relative to the positions of TX and RX.

4.2.2 Data evaluation

The data which was evaluated was acquired on the first day of the trials. For this three discone antenna elements were connected to three of the four channels from the Parasol units, while one log-per antenna was connected to the remaining channel. The discone elements served as surveillance channels, while the log-per was used to acquire a reference signal as clean as possible. For this the log-per was steered manually in the direction of the DVB-T transmitter *Hvitingen*. The surveillance array was set to a side-looking condition with steering direction towards starboard. The baseline from this TX to the RX's location at the time of the data evaluation was $B_L \approx 17650\,\mathrm{m}$. The Nøkken boat was travelling from North to South with a velocity $v_{Rx} \approx 8.1\,\mathrm{m/s}$.
The spectrum of the recorded data is shown in Fig. 4.5, while the constellation maps of four DVB-T symbols are shown in Fig. 4.6 exemplarily. The evaluated data was transmitted at $f_T = 650\,\mathrm{MHz}$. As the constellation maps are very clean, i.e. a little amount of noise, a copy of the transmitted signal can be estimated which has little amount of Bit Error Rate (BER), i.e. with little amount of wrong estimated constellation points. The outer constellation points appear noisier compared to the inner ones, which is due to the reception of multipath, an effect which leads

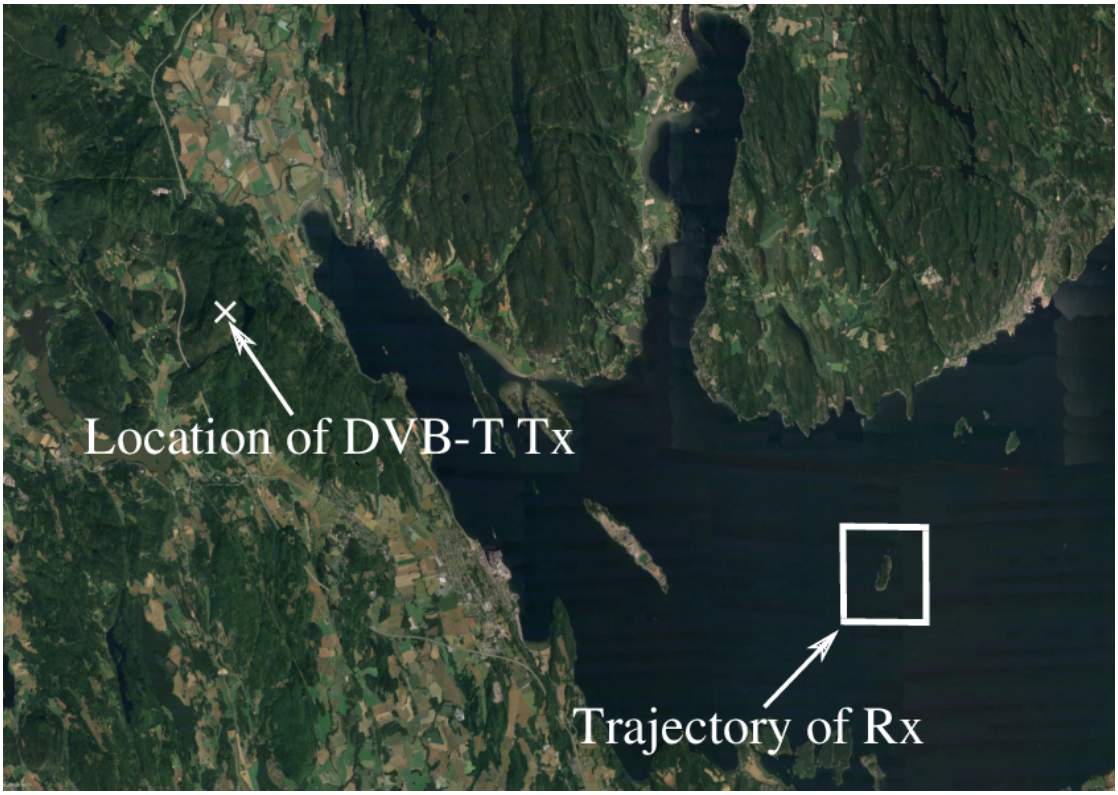

Fig. 4.4: Map of the Oslo fjord with indicated transmitter position and the receiver's trajectory (from: GoogleEarth).

to higher distortion of outer constellation points [39].

Range-Doppler maps without clutter suppression The range-Doppler maps obtained at a single surveillance channel for a CPI of $512 \cdot \mathrm{T_S} = 0.57\,\mathrm{s}$ are reported in Fig. 4.7 and in Fig. 4.8 when the range compression stage is performed according to an MF strategy and an RpF strategy, respectively. All the reported maps were scaled according to the same strategy adopted for the simulated analysis. Specifically, the 0 dB level in each map represents the estimated noise floor level that is kept constant at the output of each employed processing chain by properly scaling the filters applied so that different results can be directly compared. Moreover, the reported maps are represented using a common dynamic range in the interval [10 dB, 40 dB] above the noise floor, so that possible presence of targets and undesired residual structures can be easily identified in all the considered cases.
The strongest peak in the maps of Fig. 4.7 and Fig. 4.8 appears at Doppler 0 Hz, range gate 0, which corresponds to the direct signal from the Tx. In the reported experimental results, the direct signal contribution has not been suppressed by

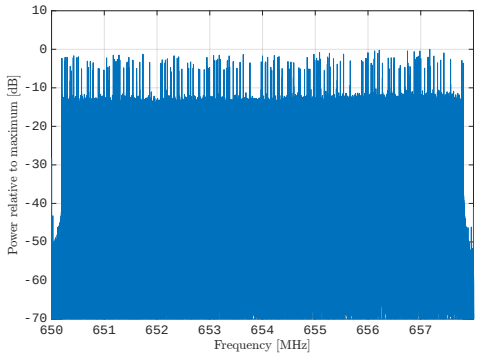

Fig. 4.5: DVB-T channel at 650 MHz.

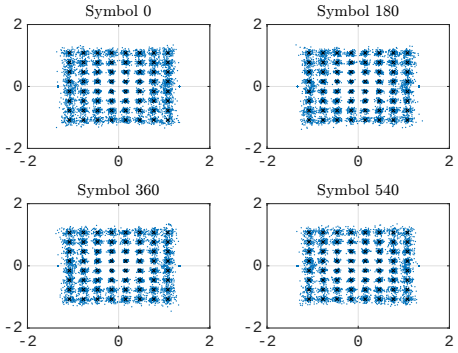

Fig. 4.6: Constellation maps for four decoded DVB-T symbols (before remapping to the constellation map). The black crosses indicate the ideal positions of the constellation points.

means of a dedicated cancellation stage. In fact, despite the theoretical developments of previous sections have been carried on under this simplifying assumption, it is intended to show that the proposed approach is effective against both the signal coming from the transmitter and its echoes from the stationary scene (namely clutter).

The Tx Doppler centroid was previously removed as described in [29]. The peak value measured for the MF case Fig. 4.7 is 96.33 dB while the RpF yields a maximum value equal to 92.11 dB. The corresponding loss is largely consistent with the value predicted by (3.42) for a 64-QAM modulation scheme.

The direct signal peak comes with high sidelobes affecting all the considered range extent. In addition strong returns appear at Doppler bins different from 0 Hz that are likely to correspond to Doppler spread clutter echoes.

All these considered signals contribute to increase the background level of the final map when exploiting a MF strategy thus jeopardizing the detection of both exo- and endo-clutter target echoes.

Given the platform velocity and the beamwidth of the employed antennas, targets can be considered as slowly moving when their bistatic Doppler frequency falls approximately within the interval [-15, 15] Hz which corresponds to an equivalent radial velocity smaller than 3.5 m/s.

In the upper part of Fig. 4.7 the enlarged view of range-Doppler regions are reported where possible targets are present. The first two regions refer to targets very close to strong clutter returns whereas the third region includes an example of exo-clutter target echo. The targets included in the first two regions cannot be

discriminated among the very high peaks appearing in those areas. In contrast, the target labelled 'T4' in the third region is sufficiently isolated so that it can be reasonably identified. However, its detection must compete with a generally high background level. Basically, whilst this target yields a SNR value of about 44 dB, the local SCNR estimated at its location is lower than 18 dB due to the disturbance background that is much higher than the estimated noise floor.
When a RpF strategy is employed Fig. 4.8, the sidelobes level of the signal AF is significantly reduced so that targets appearing outside the Doppler area of the main clutter contributions are clearly visible against the background. For instance, in this case, T4 appears at a level of 39 dB above noise (again the loss w.r.t. the MF case is because of the 64-QAM modulation scheme) and a SCNR just few dB smaller (see the range-Doppler region on the upper-right corner of Fig. 4.8). However, the main clutter structures are still clearly apparent in the final map thus masking the presence of slowly moving targets.
The next step in the proposed processing scheme involves the Doppler spread clutter removal based on a spatio-temporal approach. To this purpose, a technique which exploits the measured platform velocity v_R is applied before in order to re-establish the DPCA condition. By exploiting the measured velocity, this approach compensates by digital signal processing the mismatch from the DPCA condition, thus providing a STAP scheme that can be applied under mostly general acquisitions conditions. Here it is referred to as "flexible DPCA processing". It is addressed in detail in Sec. 5.1.
Moreover, a simple approach is adopted to provide adaptivity against amplitude/phase imbalances between the receiving channels. In fact, in practical cases, the receive channels, there including the adopted antenna elements, might show some differences, both in amplitude and in phase, that could severely limit the cancellation stage. This effect has to be compensated for in order to allow appropriate clutter cancellation. The employed technique is referred to as *Single-range Doppler-bin* (SRDB) calibration and addressed in Sec. 5.2. The results obtained with the STAP scheme after the application of this simple calibration strategy are reported in Fig. 4.9 for the STAP after MF, and in Fig. 4.10 for the STAP after RpF, respectively.
In both cases, a significant reduction is obtained for the main clutter contributions appearing at small Doppler values and this clearly demonstrates the need for a spatio-temporal clutter cancellation stage.
However, as for the case of simulated scenarios, the clutter suppression after MF does not guarantee a complete removal of the clutter sidelobes structures thus providing a generally high background level in the final map, even after the cancellation stage (see Fig. 4.9). The output power level shows a similar periodic modulation across Doppler frequencies as that observed in Fig. 3.4. As largely

investigated, this effect is due to the impossibility to effectively cancel the clutter sidelobes structures due to their random behaviour. Compared to Fig. 4.7, the resulting background level might even increase in regions where a constructive effect occurs. Consequently, some of the slowly moving targets navigating in the fjord are now visible but they cannot be easily discriminated with respect to the background, e.g. T1, T2, T3 in the upper portion of Fig. 4.9. It can be observed, that the SNR of T4 is significantly reduced as this target falls within the Doppler ambiguous cancellation notch of the DPCA filter.
The proposed RpF-based STAP approach allows filtering out both the stationary scatterers main peaks and their sidelobes structures so that the targets now appear as isolated peaks and they can be easily detected against the residual background despite the lower SNR values, see Fig. 4.10.

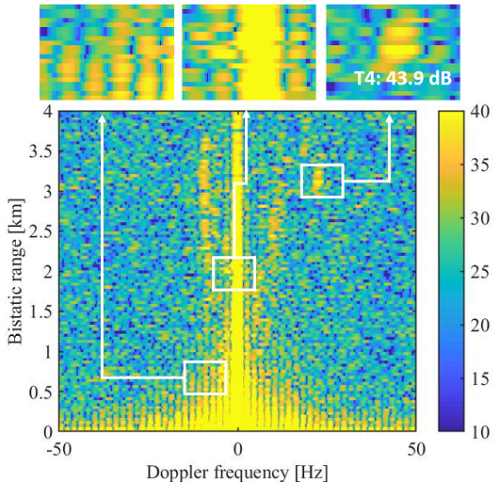

Fig. 4.7: Range Doppler map obtained for the experimental data after: MF.

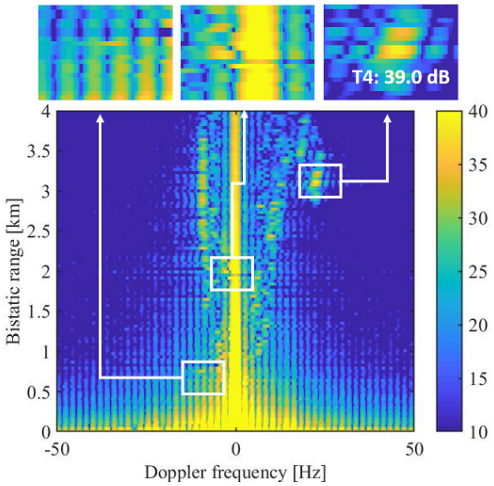

Fig. 4.8: Range Doppler map obtained for the experimental data after: RpF.

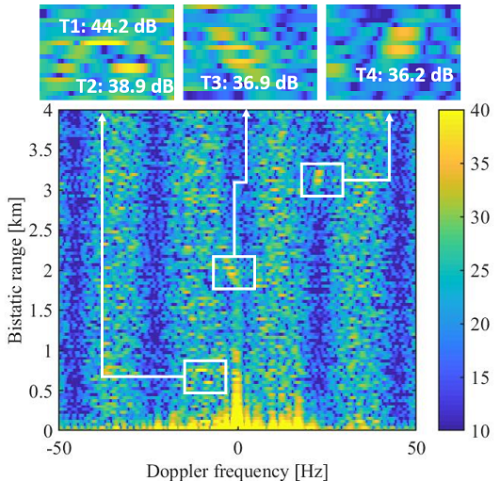

Fig. 4.9: Range Doppler map obtained for the experimental data after: STAP after MF.

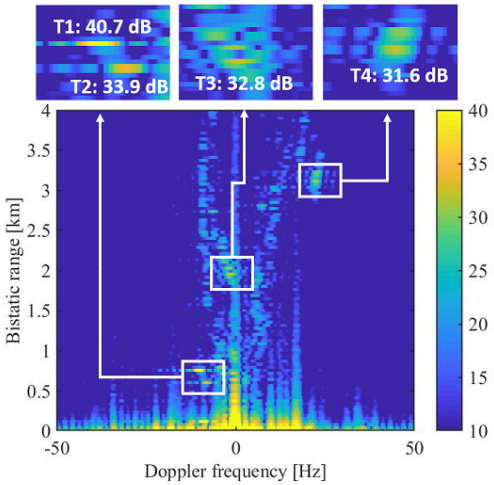

Fig. 4.10: Range Doppler map obtained for the experimental data after: STAP after RpF.

Fig. 4.11: The transmitter of opportunity "Eifel".

Fig. 4.12: The mounted antenna elements for the SRX. On the right is the GRX.

4.3 Experiment 2: Ground- and air-borne platforms

As trial site of the measurement campaign a rural area in the west of Germany was chosen. The DVB-T SFN in this area transmits on carrier frequencies $f_{C1} = 674\,\text{MHz}$ and $f_{C2} = 690\,\text{MHz}$. One particular DVB-T TX is called "Eifel / Scharteberg", which was selected as IO, Fig. 4.11 shows a photo of the transmitter.
The measurements were conducted with three receivers, one stationary receiver and two moving receivers. The stationary receiver defined as SRX consisted of one Parasol unit [38] with two recording channels. It had two logarithmic-periodic antennas which were pointing towards the IO in order to collect a clean reference signal. In Fig. 4.12 a photo of the assembled antenna elements and holdings are shown. On the right the GRX is to be seen. Two moving receivers were used: one ground-borne and one air-borne. The reason for this was, that both receivers serve as a cooperative target for the other receiver. By doing so, trial data from two moving platforms are acquired with one cooperative target in the data. Both receivers are subject to very different conditions, namely altitude, speed, field of view, etc., which all together leads to very different clutter returns that can be analysed and studied in detail. It is as well expected, that the direct signal shows different characteristics in terms of strength, and possibility of reconstruction.

Ground-borne moving receiver As ground-borne moving receiver – defined as GRX– a van was used, which pulled a caravan with a platform on top. The back-end of the receiving system, which consisted of two PARASOL units was stored in the back of the van, while the front-end of the receiving system (an antenna array) was mounted on the platform on top of the caravan. The in total

Fig. 4.13: The van with the array on the caravan.

Fig. 4.14: The antenna array with the discone elements for surveillance (elements 2–5) and calibration (element 6).

four receiving channels of both Parasol units were used as surveillance channels, each connected to a discone antenna, which is omnidirectional in azimuth. The discone antennas were mounted all together on a frame with RAM to one side, thus establishing a side-looking surveillance array. The array was positioned on top of the van and mounted on a platform which can be rotated around its centre axis by 180° and rotated in elevation. In that way, it is possible to steer the array in a certain direction. The van with the array on the caravan is shown in Fig. 4.13. A close-up of the array is shown in Fig. 4.14. The elements labelled "1" and "7" are terminated with 50 Ω, the element labelled "6" was used for calibration. It transmitted a sinusoidal signal on frequency $f_{\mathrm{Cal}} = 678\,\mathrm{MHz}$. Elements labelled "2" to "5" were connected to the Parasol units, i.e. these elements were the receiving elements. The inter-element spacing d_{GRX} was set to $d_{\mathrm{GRX}} = 0.36\,\mathrm{m}$.
An Inertial Measurement Unit (IMU) was mounted on the frame of the array in order to acquire precise ground truth position and velocity data.

Air-borne moving receiver The ULA *Delphin* was used as air-borne receiver – defined with ARX. It carried the so-called flightrecorder (the back-end receiving system), which consists of a Parasol unit mounted in a rack, which can directly be mounted inside of the ULA. The receiving front-end system was mounted into a pod, which can be mounted below a wing of the aircraft. This is shown in Fig. 4.15. Inside of the pod there was a ground plate consisting of plastic material, on whose upper side the front-end was fixed. The front-end consisted of two small log-periodic antennas, mounted with a grazing angle of 20° Deg in horizontal polarisation with an inter-element spacing $d_{\mathrm{ARX}} = 0.33\,\mathrm{m}$. On the ground plate there was as well an IMU mounted. Two Global Navigation Satellite System (GNSS) antennas, which need to be connected to the IMU, are mounted on the

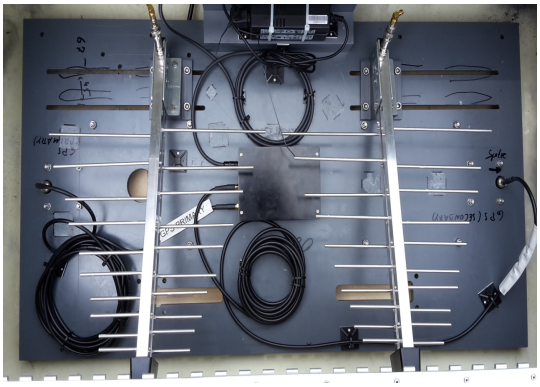

Fig. 4.15: The inside of the pod: the ground plate together with both log-periodic antennas and the IMU.

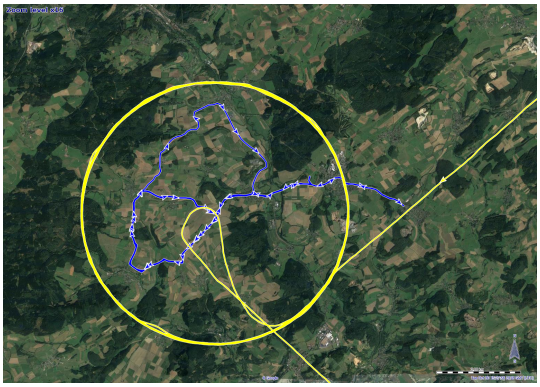

Fig. 4.16: Map from the trial site (from: Google Earth) with trajectories for the ARX (yellow) and for the GRX (blue).

bottom side of the ground plate. For the trials the pod was mounted below the right wing. In Fig. 4.16 a map with indicated trajectories of the GRX (in blue) and ARX (in yellow) are shown. The ARX was flying on a circular trajectory, while the GRX was moving on streets and roads inside of the circle flown by the ARX.

4.3.1 Data evaluation: ground-borne platform

The surveillance array was set to a left-looking condition with respect to driving direction. The baseline B_L from the TX to the GRX location at the time of the data evaluation was $B_L \approx 14.000\,\mathrm{m}$. The receiver was driving with a velocity $v_{Rx} \approx 13.8\,\mathrm{m/s}$.
The carrier frequency of the evaluated transmitted signal was $f_C = 690\,\mathrm{MHz}$. The constellation maps of four DVB-T symbols are shown in Fig. 4.18 exemplarily. As the constellation maps are very clean, i.e. a little amount of noise, the remodulated signal has little amount of BER, which leads to a good compression ratio.
For the evaluation of the ground-borne data, the dedicated calibration signal was exploited for calibration, thus providing an ideal calibration. The results for data evaluation using the MF and the RpF are shown in Figs. 4.19 and in 4.20 respectively. Apparently, the impulse responses are very well equalized with the RpF, leading to a low noise interference (visible in the exo-clutter regions), see Fig. 4.20. However, the clutter returns, e.g. at a bistatic range of 2500 m have strong sidelobes in range, decreasing there the detection capability. The reported results are scaled according to the same strategy adopted for the simulated analysis. Applying the STAP scheme leads to the range-Doppler maps shown in 4.21 and 4.22. One

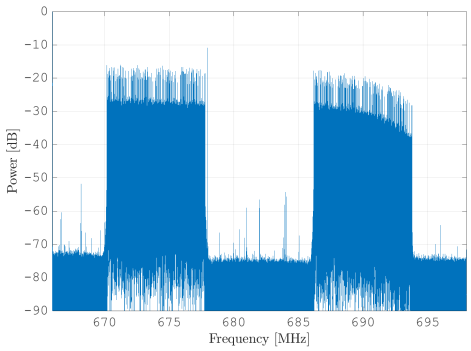

Fig. 4.17: Spectrum of the recorded data.

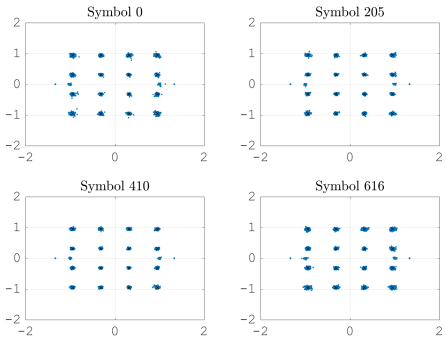

Fig. 4.18: Constellation maps for four decoded DVB-T symbols (before remapping to the constellation map).

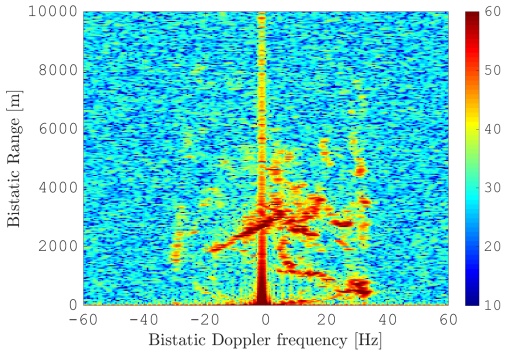

Fig. 4.19: Range-Doppler map obtained for the experimental data for MF.

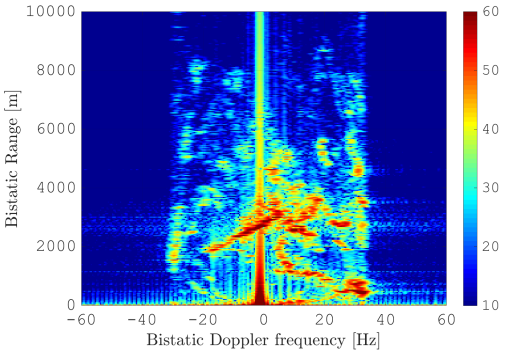

Fig. 4.20: Range-Doppler map obtained for the experimental data for RpF.

can see the sinusoidal pattern in the range-Doppler map after matched filtering, leading to a strong interference level that prevents target detection both in endo- and exo-clutter regions, which has been largely investigated. The RpF is able to provide time-invariant impulse responses, therefore the interfering noise level in exo-clutter regions is suppressed down to the noise level, being limited only by the ADC resolution. However, the clutter cancellation was not as effective as for the application for the data from the seaborne platform. Many strong clutter returns remain in the endo-clutter region. They result from rotating wind turbines, e.g. at bistatic Doppler $f_D = 30\,\text{Hz}$, bistatic range $r_B = 500\,\text{m}$, where sidelobes in Doppler can be detected. The strong returns which span in the bistatic range from 2000 m to 3000 m and bistatic Doppler shift from -20 Hz to 5 Hz are backscattered echoes from a forest close to the receiver's position.

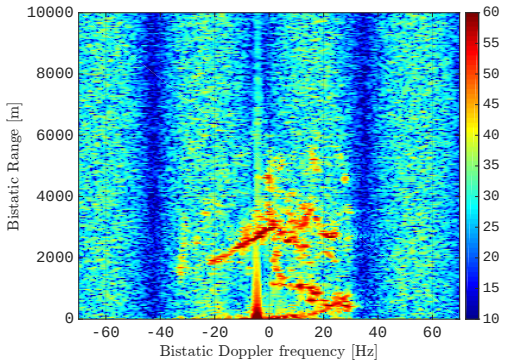

Fig. 4.21: Range-Doppler map obtained for the experimental data for MF after flex-DPCA.

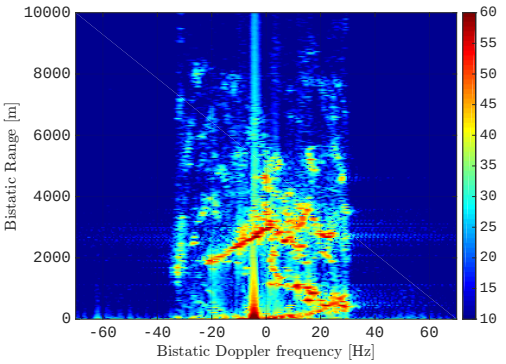

Fig. 4.22: Range-Doppler map obtained for the experimental data for RpF after flex-DPCA.

At the time stamp of data evaluation, the ARX was in a bistatic distance R_B of $R_B \approx 6500\,\mathrm{m}$, and its bistatic Doppler $f_{D_{\mathrm{ARX}}}$ shift amounted $f_{D_{\mathrm{ARX}}} \approx -31\,\mathrm{Hz}$. Fig. 4.23 reports an enlarged view into the cooperative target's position on the range-Doppler plane of Fig. 4.9 for STAP after MF. Apparently the target can not be detected, due to the sidelobes spread across the whole range-Doppler map. Fig. 4.24 reports an enlarged view into the cooperative target's position on the range-Doppler plane of Fig. 4.10 for STAP after RpF. The target return appears as peak with an SNR of $\approx 29\,\mathrm{dB}$. However, there are still clutter returns close to the target's position, which can make it hard to detect the target. Furthermore, as can be seen in Fig. 4.10, still clutter returns remain on the range-Doppler map, which result from foliage, i.e. forest and trees, and wind turbines.

4.3.2 Data evaluation: air-borne platform

The baseline from the TX to the location of the ARX at the time of data evaluation amounts $B_L \approx 8050\,\mathrm{m}$. The receiver was flying with a velocity $v_{Rx} = 36.03\,\mathrm{m/s}$, in an altitude of $H_{\mathrm{Rx}} = 1135\,\mathrm{m}$ relative to Mean Sea Level (MSL).
The carrier frequency of the evaluated transmitted signal is $f_C = 690\,\mathrm{MHz}$. Fig. 4.25 shows the spectrum of the DVB-T channel. As can be seen by the fluctuations in the spectrum, a lot of multipath was received. The constellation maps of four DVB-T symbols are shown in Fig. 4.26 exemplarily. The constellation symbols in the constellation maps are hard to be seen, however the structure is visible. The high amount of noise in the constellation maps is not due to failing remodulation algorithms due to a high radial velocity of the ARX relative to the TX. In fact, the DVB-T standard is very resistant to high velocities, provided the SNR is high. This means, as long as the SNR is above a certain value, the receiver's velocity

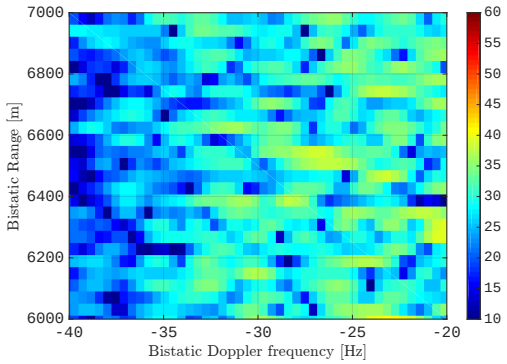

Fig. 4.23: Range-Doppler map for MF after flex-DPCA: Enlarged view into Fig. 4.9 at the cooperative target's position.

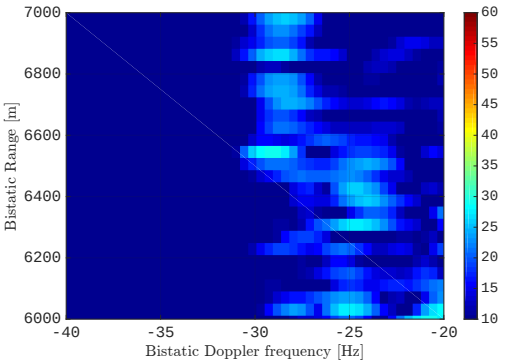

Fig. 4.24: Range-Doppler map for RpF after flex-DPCA: Enlarged view into Fig. 4.10 at the cooperative target's position.

can be compensated and the received signal can be decoded [14].
The reason for the noisy constellation maps is in fact a low Signal-to-interference-and-noise Ratio (SINR). As the ARX is flying it receives transmitters from a greater distance, which are usually shadowed for ground borne receivers due to landscape, hills, forests, and man-made objects like buildings, etc. That is, the ARX received signals emitted from Digital Video Broadcasting – Second Generation Terrestrial (DVB-T2) SFN located in other regions of Germany and Western Europe, e.g. France and the Benelux countries. These transmitters are in a greater distance than the guard interval length, and transmit a different content. For this reason, the signals are interfering signals and decrease the SINR, thus preventing a successful decoding and remodulation. This is described in detail together with a technique to suppress the interference to a certain amount in [6].

Fig. 4.27 shows range-Doppler maps for the evaluated data. Although the remodulated reference signal is very noisy, one can see lower noise level due to the equalized OFDM symbols. However, the overall suppression performance, as it was seen for the seaborne and the groundborne trials, is not given here. Recalling the constellation maps 4.6 and 4.18 from the described trials and the successful equalization of the waveform and comparing it to the results from the airborne trials, definitely shows the importance of a clean and good acquired reference signal. This can be further seen in Figs. 4.28 and 4.29, where the application of DPCA is shown, both for the MF and the RpF. It can be seen, that the overall noise and clutter level for reciprocal filtering and DPCA is lower than compared to the matched filtering. However, the clutter level is still considerably high for both filters.

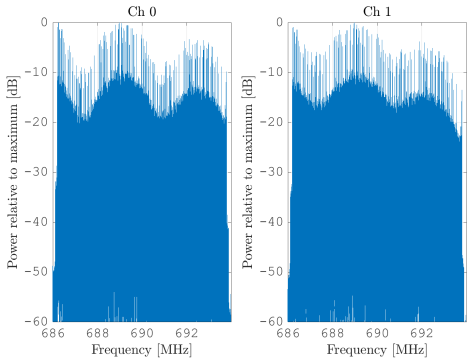

Fig. 4.25: DVB-T channel of the acquired data.

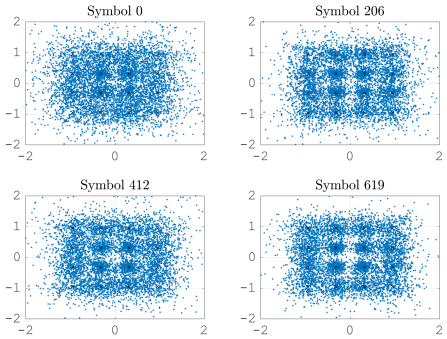

Fig. 4.26: Constellation map for different symbols from the airborne data. The black crosses indicate the ideal positions of the constellation points.

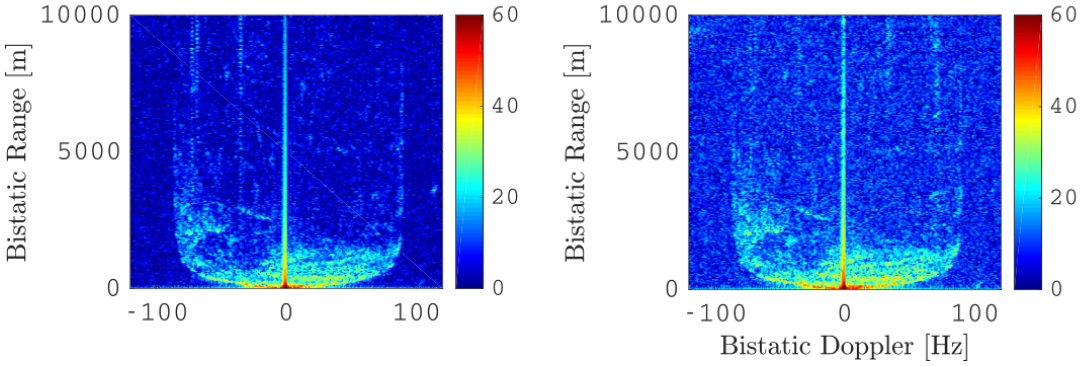

Fig. 4.27: Range-Doppler maps for data evaluation of the ARX for the LA. Left: for Rpf. Right: for MF.

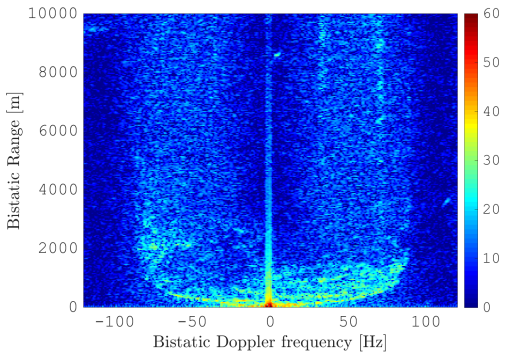

Fig. 4.28: Range-Doppler map after DPCA and matched filtering.

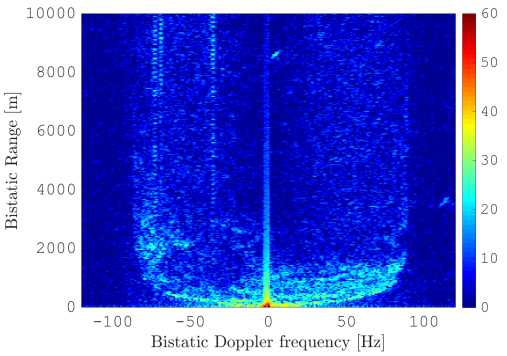

Fig. 4.29: Range-Doppler map after DPCA and reciprocal filtering.

Chapter 5

Further data evaluation and improvements

5.1 Flexible DPCA-shift

As mentioned in the Introduction, the authors of [27][26] show that a perfect DPCA condition can be easily obtained when parasitically exploiting continuous waveform transmissions. In fact, any required temporal delay between the signals collected at the two Rx antennas can be simply obtained by properly selecting temporally displaced fragments of the received signals, being the granularity limited by the sampling frequency f_S only.
However, when considering DVB-T signals, especially for the case of a RpF based range compression stage, a batching strategy is adopted, so that the temporal delay granularity is typically limited by the OFDM symbol duration. Therefore, in Chapter 3 the constraint was restored on the equivalent PRF, i.e. it was assumed that the relevant parameters satisfy the following condition $T_{\mathrm{DPCA}} = K\mathrm{T_S} = d/v_R$.
In practice, a more general STAP technique is required for an operational passive radar. Based on the DPCA approach, an effective STAP approach is obtained by relaxing the constraint on the equivalent PRF, along the line suggested by Ender in [40] for the case of a SAR equipped with two displaced antennas for MTI applications. Basically, the temporal displacement between the observations of the LA and the TA can be compensated for during the SAR azimuth processing by operating in the Doppler frequency domain where a linear phase shift should be corrected. This is quite appropriate in air-/space-borne SAR systems since the delay to be compensated is usually much smaller than the CPI.

5.1.1 Algorithm based on third-party device

In the case considered here, depending on the relative delay between the signals received at the two antennas, the time shift T_{DPCA} of the signal collected by the TA can be performed in a more robust way by resorting to a two-stage approach. Specifically:

- The first stage is a shift in time domain where time is quantized to the equivalent PRI so that the time delay that can be compensated for is given by:

$$T_q = \left\lfloor \frac{d}{\mathrm{T_S} v_R} \right\rfloor \mathrm{T_S} \tag{5.1}$$

- The second stage is a fine time delay compensation that is performed in the frequency domain by applying a linear phase law $\varphi_{\Delta T} = 2\pi f_D \Delta T$ where:

$$\Delta T = T_{\mathrm{DPCA}} - T_q,\ \Delta T \in [0, \ldots, \mathrm{T_S}] \tag{5.2}$$

Assuming that the platform velocity v_R can be measured (e.g. with an IMU) during the data acquisition) or estimated from the data, the dual-stage procedure presented above compensates by digital processing the mismatch from the DPCA condition, thus providing a STAP scheme that can be applied under mostly general acquisition conditions. This STAP scheme is referred to as "flexible DPCA processing" (or short flex-DPCA). By the presented approach the strict DPCA condition is relaxed and the mismatch can be compensated for by digital (post-) processing, instead of adapting the velocity to the PRI.
Unfortunately, the application of this approach requires the data processing scheme in Fig. 3.2 to be slightly modified. In particular, as the fine time delay compensation stage operates in the Doppler domain, the range-Doppler map cannot be built based on the output of the cancellation stage. In contrast, two different range-Doppler maps should be built at the two available channels and then subtracted after linear phase compensation. This clearly increases the computational load of the processing with respect to the basic scheme in Fig. 3.2 since the evaluation of the range/Doppler map is usually the most costly operation.
A flowchart of the modified processing is shown in Fig. 5.1.

5.1.2 Simulation

Various simulations were carried out to prove the performance of the proposed RpF-based STAP scheme in comparison to an MF-based alternative, and to show

the improvement provided by the flexible DPCA processing.
The antenna element spacing d was set to $d = \lambda/2$, and the receiver's velocity was set to $v_R = 24.53\,\mathrm{m/s}$ (this value was chosen randomly). For the ideal DPCA to hold, the TA will occupy the spatial position of the LA after a time delay $T_{\mathrm{DPCA}} = \frac{d}{v_R} = 0.01019 = K\mathrm{T_S} = 9.0992\mathrm{T_S}\,\mathrm{s}$. If the processing is adopted as being described so far (i.e. using the batching strategy), the DPCA condition can be restored using (5.1) and (5.2), which yields: $T_q = 9\mathrm{T_S}$ and $\Delta T = 0.0992\mathrm{T_S}$.
To show this, a complete scenario is simulated including clutter, target echoes, and noise. The input CNR was set to 30 dB, while the target's SNR was selected to be -40 dB, being the noise level deliberately set to unitary power level.
When applying a simple DPCA processing that basically quantizes the time shift to be applied to the PRI granularity, the actual time shift that is compensated for is T_q instead of T_{DPCA} and a severe cancellation loss is experienced despite the limited error. This is clearly shown in Fig. 5.2 where the output of the cascade of RpF and a simple DPCA approach is reported for the case under consideration.
The clutter ridge is not totally filtered out and only the very low Doppler components have been effectively removed. The reason for the removal of the very low Doppler components can be seen by Fig. 5.3. The fine time shift (i.e. the phase modulation) according to (5.2) applies a phase law for each Doppler frequency, where the phase to be compensated for Doppler $f_D = 0$ amounts zero: $\varphi_{\Delta T}(f_D = 0) = 0$. For this reason is the clutter at Doppler frequency $f_D = 0$ removed, while with increasing Doppler frequency the clutter suppression decreases. The strong clutter residuals severely mask the target echo that was injected at bistatic range of about 10 km and Doppler frequency 45 Hz (see enlarged view in the box at the upper-right corner of the figure).
When exploiting the flex-DPCA approach, with either a MF or a RpF strategy at the range compression stage, the main clutter ridge cancellation capability is effectively recovered (see Fig. 5.5 and Fig. 5.4, which correspondend to the label "(II)" in Fig. 5.1).
However, the limits of the MF are still apparent since a quite high background level is obtained after the cancellation stage. As studied intensively, such background level shows a sinusoidal modulation in the Doppler dimension with period $\frac{1}{T_{\mathrm{DPCA}}}$ and exists at a level higher than the target output level. Consequently, the injected target echo cannot be detected against the clutter residuals. This can be easily verified based on the enlarged view reported in the box at the upper-right corner of Fig. 5.5 and from the corresponding range and Doppler cuts extracted at the target's position (see Fig. 5.6–Fig. 5.9).

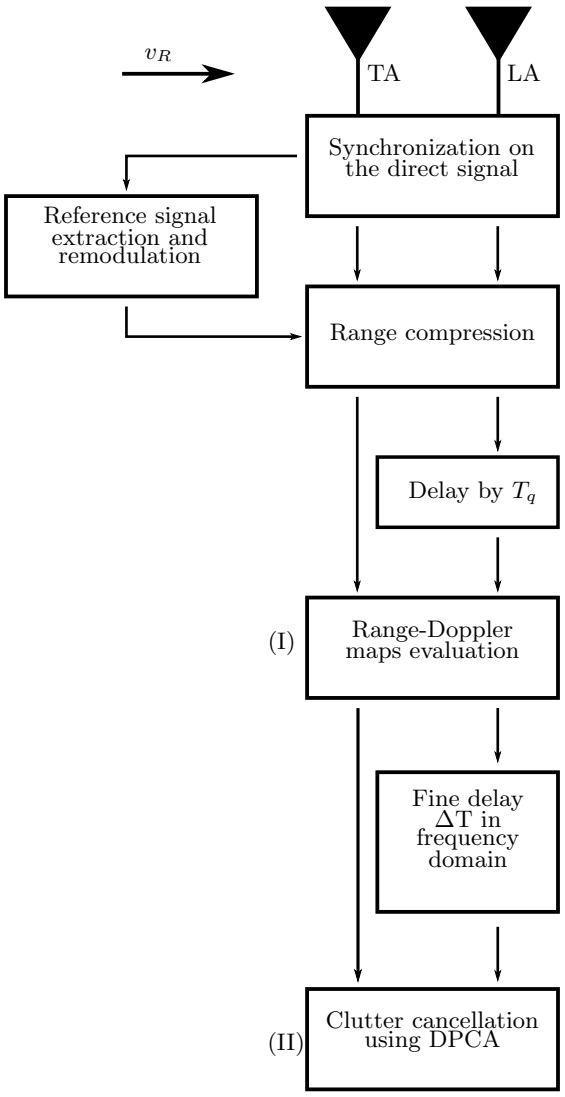

Fig. 5.1: Flowchart of the processing including the "flex-DPCA".

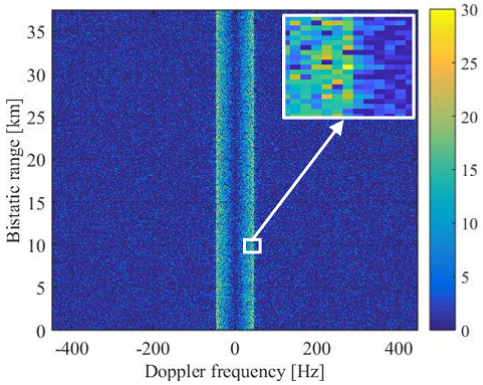

Fig. 5.2: Range-Doppler map in dB for the scenario including target, clutter, and noise under non-perfect DPCA conditions with flex-DPCA not being applied.

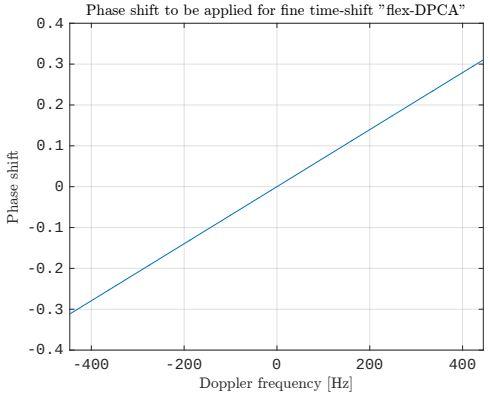

Fig. 5.3: The phase shift to be applied for each Doppler frequency due to the fine time-shift from the flexible DPCA.

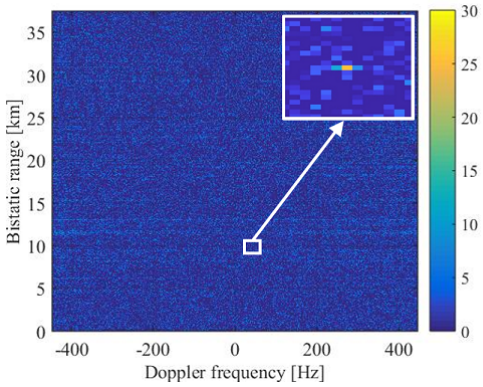

Fig. 5.4: Range-Doppler map in dB for the scenario including target, clutter, and noise with STAP being applied and RpF used for range compression.

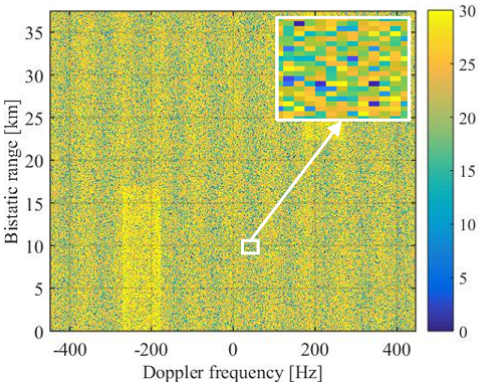

Fig. 5.5: Range-Doppler map in dB for the scenario including target, clutter, and noise with STAP being applied and MF used for range compression.

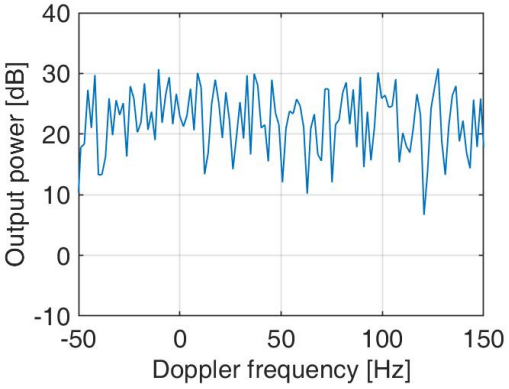

Fig. 5.6: (a)

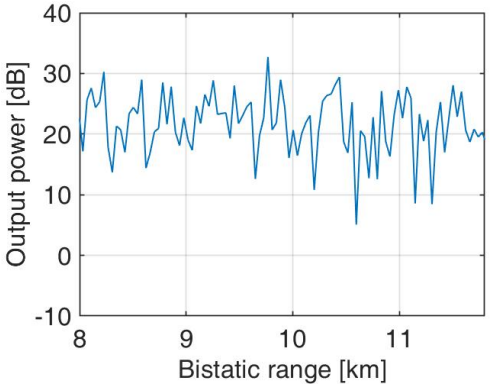

Fig. 5.7: (b)

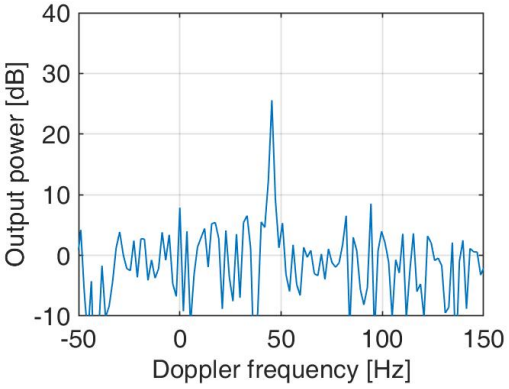

Fig. 5.8: (c)

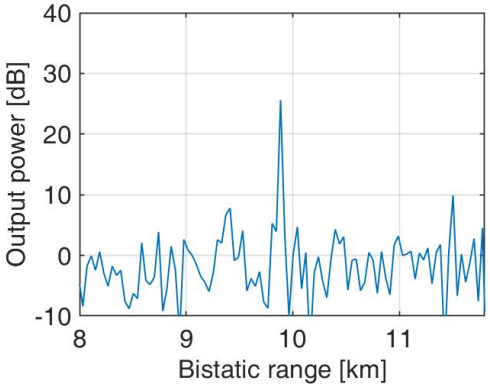

Fig. 5.9: (d)

Fig. 5.10: Range and Doppler cuts, respectively, for target's position. (a-b) STAP after MF; (c-d) STAP after RpF.

5.2 Digital Calibration

The performance of DPCA is heavily depending on the calibration of the used hardware. Inequalities in the hardware, e.g. different cable lengths or different filters, introduce incoherence of the sampled signals and can significantly worsen the performance, as described in [41]. In active radar usually an external signal - for example a sinusoid - is used to calibrate the hardware, by estimating the phase and amplitude from the received sinusoid of each antenna element to a reference antenna element. The errors of each element are then corrected by applying the estimated values. However, this solution is not very attractive for a passive radar system, as for this calibration procedure a signal needs to be emitted, which controverts the covert operation. Instead a digital calibration method making use of already available signals would be advantageous and highly appreciated. A possibility to solve this is a calibration on the LOS signal of the IO, as this is usually the strongest and first incoming signal, which appears in a range-Doppler map at range gate $r_g = 0\,\mathrm{m}$, provided there is LOS to the IO. In [42] an autocalibration method using the LOS signal for mobile communication signals is described. The authors of [43] describe a mutual decoupling algorithm using the LOS signal for a circular array for passive radar. In [44] an autocalibration method based on eigenstructure is applied on a stationary GSM passive radar and compared to the active calibration solution.
In the studies conducted here channel errors of the hardware resulting in different amplification, different delays, and different phased are analyzed in a simulation. The simulation and its results are described in Sec. 5.2.1. In Sec. 5.2.2 and Sec. 5.2.3 two different digital calibration methods and their results are presented, where both methods make use of the direct signal from the IO.

5.2.1 Simulation results

Usually, there will be inequalities in between each channel $\nu = 0, \ldots, N_A - 1$, such as different amplification $\xi_{A\nu}$, differences in the phase $\xi_{\phi\nu}$, e.g. due to unequal filters, or different delays $\xi_{\tau\nu}$, e.g. due to different cable lengths. N_A defines the number of antenna elements. The delays $\xi_{\tau\nu}$ are not resulting from the direction of arrival u, which is represented with $\tau_\nu = \frac{d}{\lambda}\cos\rho_0$. If IQ-demodulation is performed, the inphase- $I_\nu(t)$ and quadrature-component $Q_\nu(t)$ will also incur IQ-imbalance. This can be neglected if instead the Q-phase of the received signal is calculated from the I-phase by using a Hilbert transformation.
Following the approach in [41], one obtains for the down-converted and received

signal on antenna element ν:

$$S_\nu(t) = \xi_{A\nu}\mathrm{LP}\{s_{\mathrm{Rx}}(t-\xi_{\tau\nu})\cos(2\pi f_C t - \xi_{\phi\nu})\} \tag{5.3}$$
$$+ j\mathrm{LP}\{-s_{\mathrm{Rx}}(t-\xi_{\tau\nu})\sin(2\pi f_C t - \xi_{\phi\nu})\} \tag{5.4}$$

To study the influence of inter-channel errors, the covariance matrix $\mathbf{R}$ for returns from P clutter patches is estimated:

$$\mathbf{R} = E\{\mathbf{S}\mathbf{S}^{\mathbf{H}}\} = \sum_{p=0}^{N_{CP}} E\{\mathbf{S}_p\mathbf{S}_p^H\} + E\{\mathbf{N}_{Th}\mathbf{N}_{Th}^H\} \tag{5.5}$$

where $\mathbf{N}_{Th}$ represents thermal noise. $\mathbf{S}_p$ defines the signal from source p received by the array.
The signal model makes use of the fact, that the return from a clutter patch equals a Dirac delta function if the RpF is used in the receive filter. Therefore, the return signal (without any errors in the channel) can be written as the space-time matrix [18]:

$$\mathbf{S}_p = \mathbf{b}_p \otimes \mathbf{a}_p \tag{5.6}$$

$\mathbf{a}_p$ and $\mathbf{b}_p$ represent the spatial steering and temporal steering vector from source p:

$$(\mathbf{a}_p)_n = \exp(j2\pi n f_C \tau_{np}), \qquad n = [0,\ldots,N] \tag{5.7}$$
$$(\mathbf{b}_p)_m = \exp(j2\pi m f_{Dp}/f_{\mathrm{PRF}}), \qquad m = [0,\ldots,M] \tag{5.8}$$

f_{Dp} represents the Doppler shift from source p and f_{PRF} represents the PRF. M defines the number of OFDM symbols.
The influence of the errors is defined in $\mathbf{Q}_p$ [41], the so-called error sinc function:

$$(\mathbf{Q}_p)_{il} = \xi_{Ai}\xi_{Al}\exp(j\xi_{\phi i})\exp(-j\xi_{\phi l})\mathrm{sinc}(\pi B(\tau_i - \tau_l + \xi_{\tau i} - \xi_{\tau l})) \tag{5.9}$$

With (5.6) this leads to:

$$\mathbf{S}_p = \mathbf{b}_p \otimes \mathbf{a}_p\mathbf{Q}_p \tag{5.10}$$

Simulation parameters A covariance matrix for one range gate equally separated into P clutter patches was simulated. Each clutter patch represents one single source p and has a width of $\delta_\phi = 0.1°$. The clutter patches are defined for an azimuthal interval of $\pm 85°$ relative to broadside. The number of antennas N_A and of OFDM symbols M were set to $N = 3$ and $M = 128$. The carrier frequency f_C was set to $f_C = 600\,\mathrm{MHz}$, and the inter-element spacing d was set to be $d = \lambda/2$.

The velocity v_R of the receiver was set to $v_R \approx 24.8\,\mathrm{m/s}$, i.e. fulfilling the DPCA condition. The three errors ξ_τ, ξ_A, and ξ_ϕ are considered in the following analysis separately. For each error source, a probability density function of the error (treated as a random variable) is considered, and the corresponding space-time covariance matrix is derived according to the signal model in (5.10). Each realization of an inter-channel error was done independently of the other errors and repeated ten times. The analysis is conducted by calculating for each realization of the error the eigenvalue decomposition of the covariance matrix as well as the resulting SINR, defined as:

$$\mathrm{SINR}(f_D) = \frac{|\mathbf{w}^H \mathbf{s}|^2}{\mathbf{w}^H \mathbf{R} \mathbf{w}} \tag{5.11}$$

where $\mathbf{w} = \mathbf{R}^{-1}\mathbf{s}(f_D)$. In all cases, the performance corresponding to an error-free covariance matrix are reported and labelled as 'Ideal'. The influence of the signal bandwidth without any errors is not simulated, as for DVB-T the fractional bandwidth B_f is approximately $B_f = B/f_C \approx 1.27\%$. As a consequence a narrowband signal can be assumed [41].

Influence of delay errors

For the simulation of different inter-channel delays $\xi_{\tau\nu}$ following was assumed: in the digital processing stage the sampled data of each channel is synchronized to the start of a DVB-T symbol separately (compare 2.2.3). As the ADCs sample with a frequency of f_S, the maximum inter-channel delay ξ_τ can be $\xi_\tau = \frac{1}{2f_S}$ in the worst-case. The inter-channel error delay ξ_ν is therefore modelled as a uniform distributed random variable in the interval $[-\frac{1}{2f_S}, \frac{1}{2f_S}]$. For each realization the eigenvalues and the SINR were calculated. The results are shown in Figs. 5.11 and 5.12. The green line expresses the results for the calibration errors, whereas the blue line indicates the results for an ideal antenna array. Apparently the delay errors do not have an influence on the eigenvalue distribution compared to the ideal covariance matrix. This is also expressed by the SINR curve in 5.12. That means the synchronization on the DVB-T signal for each sampled data provides a sufficient calibration, which makes delay inequalities in between the receiving channels negligible.

Influence of amplitude errors

The amplitude inequalities were simulated as normal distributed random variables with variance $\sigma_A^2 = 0.003$ and a mean value of $\mu = 0.67$. This is motivated by the evaluation of measurement data from the trials in Norway (for a description of the trials refer to Sec. 4.2. For this, a CPI for the duration $T_{\mathrm{CPI}} = 512 \cdot (\mathrm{T_U} +$

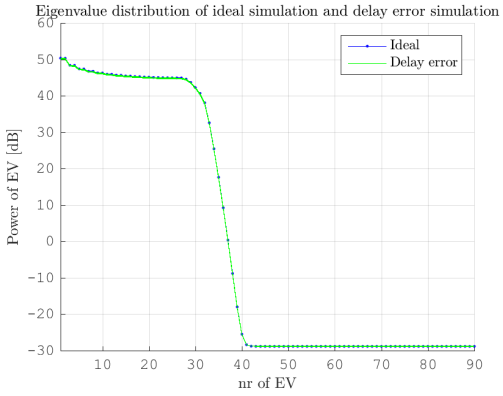

Fig. 5.11: Eigenvalue distribution of covariance matrix **R** with influence of delay errors compared to the ideal covariance matrix.

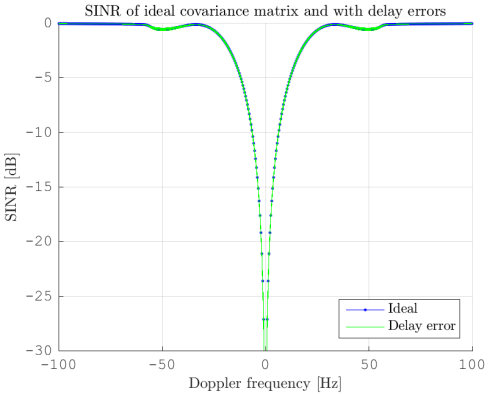

Fig. 5.12: SINR with influence of delay errors compared to the ideal covariance matrix.

$T_{CP}) = 512 \cdot (T_U + \frac{1}{8}T_U) \approx 0.5\,s$ from both receiving channels of one Parasol-unit was synchronized in time, the reference signal was reconstructed, and the range-compression with the RpF was conducted. Finally, in the range-Doppler map, the complex value of the range-Doppler bin where the direct signal appears was compared for both receiving channels in terms of amplitude and phase difference. The mean value $\mu_{A/\phi}$ and the variance $\sigma^2_{A/\phi}$ was estimated from the analysed data, which motivated the choice of σ^2_A and μ_A. In Fig. 5.13 the eigenvalue distribution with amplitude errors are shown. The power of the eigenvalues – indicated with the green lines – increases compared to the ideal case (blue line). The notch is not broadened in comparison to the ideal case, see Fig. 5.14, only notches at $\pm 50\,Hz$ get slightly deeper. In other words for this particular simulation, the inequalities of the amplitudes do not have a significant influence on the clutter suppression. However, a calibration is preferred to have.

Influence of phase errors

In this simulation phase errors are analysed. The inequalities of the phase between the channels are simulated as being uniformly distributed in the interval $\xi_\phi = [75°, 103°]$. The choice for this is motivated by the evaluation of measurement data as described in 5.2.1. In Fig. 5.15 the eigenvalue distribution of the covariance matrices with phase inequalities (green line) are shown compared to the ideal distribution (blue line). The phase errors do not have an influence on the eigenvalue distribution, but nevertheless the width of the notch of the SINR curve increases in comparison to the ideal case, thus limiting the detection for

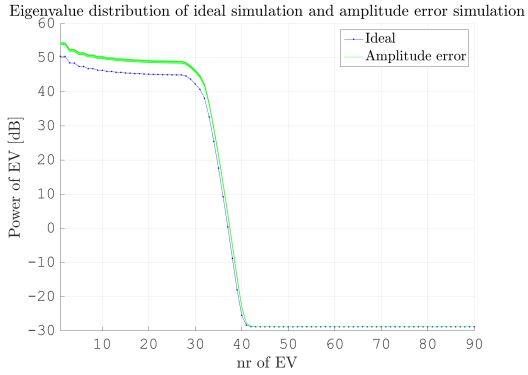

Fig. 5.13: Eigenvalue distribution of covariance matrix $\mathbf{R}$ with influence of amplitude errors compared to the ideal covariance matrix.

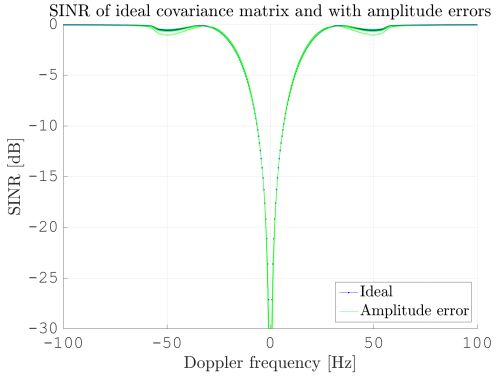

Fig. 5.14: SINR with influence of amplitude errors compared to the ideal covariance matrix.

faster moving targets, see Fig 5.16. For some realisations the SINR becomes worse for the complete Doppler range, which can make target detection difficult even for fast moving targets by up to 3 dB and thus degrade the system's performance drastically.

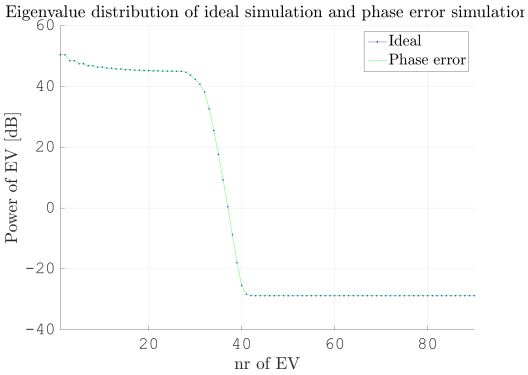

Fig. 5.15: Eigenvalue distribution of covariance matrix $\mathbf{R}$ with influence of phase errors compared to the ideal covariance matrix.

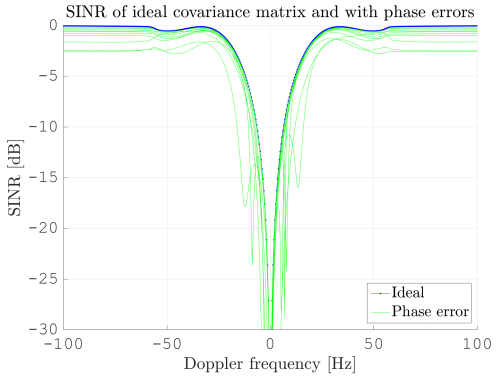

Fig. 5.16: SINR with influence of phase errors compared to the ideal covariance matrix.

5.2.2 Single Range-Doppler bin

As shown in Sec. 5.2.1, the influence of channel delay errors is already compensated during the synchronization on the DVB-T signal. The amplitude and phase

inequalities are not compensated during this process, but it is possible to use the direct signal for calibration:

$$\phi_c = \arg\{Z_{\mathrm{LA}}(f_{\mathrm{DS}}, r_{\mathrm{DS}}) Z_{\mathrm{TA}}(f_{\mathrm{DS}}, r_{\mathrm{DS}})^*\} \tag{5.12}$$

$$f_A = \left| Z_{\mathrm{LA}}(f_{\mathrm{DS}}, r_{\mathrm{DS}}) / Z_{\mathrm{TA}}(f_{\mathrm{DS}}, r_{\mathrm{DS}}) \right| \tag{5.13}$$

$Z_{\mathrm{LA}}(f_{\mathrm{DS}}, r_{\mathrm{DS}})$ is the complex data at the position of the LOS signal in the range-Doppler map of the reference element, i.e. the element on which the other antenna element has to be calibrated. Here it refers to the leading antenna. r_{DS} defines the range gate where the direct signal appears, which is due to synchronisation on the direct signal at $r_{\mathrm{DS}} = 0\,\mathrm{m}$. f_{DS} defines the Doppler bin where the direct signal appears. This is dependent on the receiver's velocity relative to the TX: $f_{\mathrm{DS}} = \frac{\mathbf{p}_{\mathrm{RT}} \mathbf{v}_{\mathrm{R}}}{c_0} f_C$.
Z_{TA} refers to the element that is to be calibrated relatively to the reference element Z_{LA}, here it refers to the trailing antenna. The calculated values ϕ_c and f_A are the corrections for the phase and amplitude mismatch, respectively, which have to be applied on the range-Doppler data Z_{TA}.
In the case of multiple receive elements ($N > 2$), all elements but one (e.g. the leading element), will be calibrated relative to the leading antenna element.
It has to be noted here, that the described processing can be applied, if the *flex-DPCA* processing (see Sec. 5.1) has been applied before.
Furthermore, if a localization technique is applied afterwards, e.g. beamforming for localization of detected targets, the angle of arrival of target signals will be relative towards the steering angle of the TX, as this angle was compensated in the calibration process.
The described method will be referred to as *Single Range-Doppler Bin (SRDB)* calibration.

5.2.3 Eigenvalue Decomposition Method

In [45] a calibration method based on eigenvalue decomposition of a range-covariance matrix R_q is described. This method is applied for calibration of two SAR images, here it is adapted to be applied on the direct signal from the TX. The range-covariance matrix is estimated according to:

$$R_q(f_D) = \frac{1}{N_{RC}} \sum_{k}^{N_{RC}} \mathbf{Z}(f_D, k) \mathbf{Z}(f_D, k)^H \tag{5.14}$$

where N_{RC} is the number of range cells to be taken into account for estimating R_q. $\mathbf{Z}(f_D, k)$ is defined as:

$$\mathbf{Z}(f_D, k) = \begin{bmatrix} Z_{\mathrm{LA}}(f_D, k) \\ Z_{\mathrm{TA}}(f_D, k) \end{bmatrix} \tag{5.15}$$

where $Z_{\mathrm{LA}}(f_D, k)$ and $Z_{\mathrm{TA}}(f_D, k)$ are the complex values at Doppler-bin f_D and the index k of the range-gates of the reference antenna element (e.g. the leading antenna) Z_{LA} and the antenna that has to be calibrated Z_{TA} (e.g. the trailing antenna).
Using an eigenvalue decomposition, eigenvalues λ_n and eigenvectors $\mathbf{e}_n$ can be calculated, where $n = [1, \ldots, N]$. The index $n = 1$ refers to the greatest eigenvalue. Each eigenvector $\mathbf{e}_n$ consists of two components e_{n1} and e_{n2}. For calibrating the amplitude, the relation of the components of the eigenvector referring to the stronger eigenvalue is used:

$$f_A = \left| \frac{e_{11}}{e_{12}} \right| \tag{5.16}$$

The estimation for the calibration value for the phase is:

$$\phi_C = \arg \{ e_{12} e_{11}^* \} \tag{5.17}$$

Using these estimated calibration factors, the data Z_{TA} can be calibrated with:

$$Z_{\mathrm{TA}}^{(c)} = f_A Z_{\mathrm{TA}} \exp\{j\phi\} \tag{5.18}$$

The remarks which were noted for the single range-Doppler bin calibration (see 5.2.2) hold here as well.
The described method will be referred to as *Eigen-value Decomposition (EVD)* calibration.

5.2.4 Mean value calibration

Another calibration method that was implemented and evaluated is based on the estimating the mean value for phase and amplitude of Doppler bins of an extended bistatic range. It is based on the observation, that there are strong clutter returns on the bistatic range cells after the direct signal range-Doppler bin. Therefore it is expected, that the estimation of the mean value gives calibration values which are more adaptive to the clutter and therefore the clutter will be suppressed in a better way.
The values ϕ_C and f_A for phase and amplitude calibration are calculated according to:

$$\phi_C = \frac{1}{N_{RC}} \sum_{r=1}^{N_{RC}} \arg \left(Z_1(f_D, r), Z_2(f_D, r)^* \right) \tag{5.19}$$

$$f_A = \frac{1}{N_{RC}} \sum_{r=1}^{N_{RC}} |f_A| = \frac{1}{N_{RC}} \sum_{r=1}^{N_{RC}} \left| \frac{Z_1(f_D, r)}{Z_2(f_D, r)} \right| \tag{5.20}$$

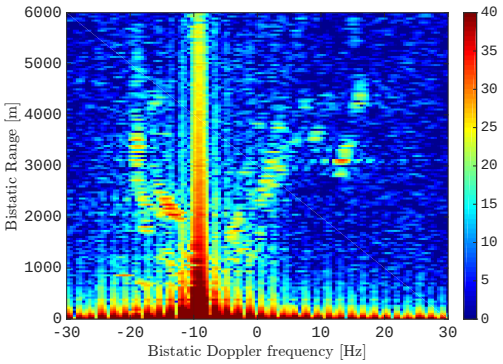

Fig. 5.17: Range-Doppler map after RpF and DPCA without calibration.

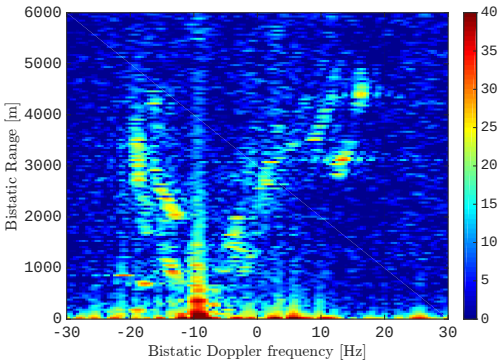

Fig. 5.18: Range-Doppler map after RpF and DPCA with EVD calibration.

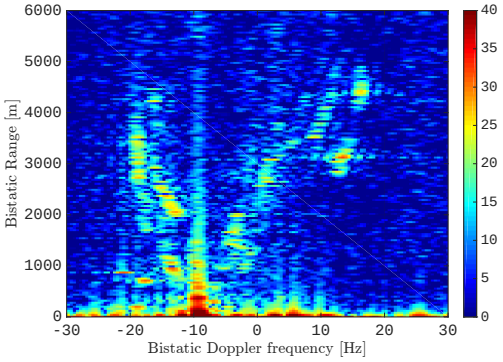

Fig. 5.19: Range-Doppler map after RpF and DPCA with SRDB calibration.

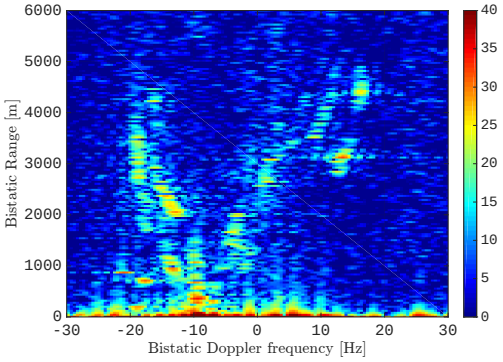

Fig. 5.20: Range-Doppler map after Rpf and DPCA with MVA calibration.

where N_{RC} is the number of range cells taken into account for estimation of the calibration values. The remarks which were noted for the single range-Doppler bin calibration (see 5.2.2) hold here as well.
The described method will be referred to as *Mean Value (MVA)* calibration.

5.2.5 Results of calibration techniques

Fig. 5.17 reports the results without calibration of the data, while in Figs. 5.18, 5.19, and 5.20 the results according to the EVD, SRDB, and MVA calibration approaches are reported. For the EVD and MVA calibration stage the first $N_{RC} = 10$ range cells were taken into account. Obviously, a dedicated calibration stage is a crucial factor for the processing, see Fig. 5.17, where the direct signal, its

sidelobes, and the clutter are not suppressed, thus limiting considerably the target detection. However, when a digital calibration is applied, the results are improved in terms of clutter suppression as well as in suppression of the direct signal. While the result after applying EVD calibration is very similar to the SRDB calibration, the MVA calibration is able to suppress the direct signal even more, thus increasing more the dynamic range for slow moving targets.
However, it must be noted, that the performance for EVD calibration and MVA calibration is very dependent on the number of range cells taken into account, and on the clutter returns at the direct signal Doppler bin itself. Furthermore, the performance is limited, if the direct signal is not received in the main lobe, but maybe in the back lobe, or with RAM in between the receiving array and the IO. Then the phase term from the direct signal might show a random and non-deterministic behaviour, which makes a reliable calibration for clutter filtering not possible.

5.3 Direct-signal-interference suppression

A common problem in passive radar systems is the presence of the direct signal or commonly called Direct Signal Interference (DSI), which consists of the direct signal and of multipath returns (i.e. clutter echoes). Usually the direct signal is the strongest and first incoming signal (provided there is LOS to the illuminator) and many magnitudes stronger than any clutter and target echo, thus this interference is the limiting factor of a PCL system, rather than thermal noise. Additionally, sidelobes of the direct signal may overlap moving targets, whose Doppler frequency are in the order of the direct signal's Doppler frequency f_{DSI}[1]. Therefore an effective method to suppress the DSI is a crucial factor in any PCL system. It has to be effective in that way, that the DSI is sufficiently suppressed, i.e. enabling target detection, while echoes of moving targets are preserved.
For a stationary and non-moving passive radar the direct signal and the multipath will be centered around (ideally on) the zero-Doppler line in a range-Doppler map. An algorithm for DSI suppression removes accordingly both direct signal and clutter/multipath returns. A recent overview and evaluation of commonly used DSI suppression algorithms for stationary passive radar systems can be found in [46].
When on a moving platform, the multipath returns have usually different Doppler frequencies f_{Cl} (unless coming from the same absolute value of the angle of arrival) than the Doppler frequency of the direct signal interference f_{DSI}. This means, that in contrast to a stationary and non-moving passive radar, the higher the velocity the less multipath returns will be suppressed in the same processing step. A recent overview and comparison of DSI suppression methods for stationary PCL systems can be found in [46].

5.3.1 ECA-CD

One technique to suppress the direct signal is described by Colone in [34], which is called Extensive Cancellation Algorithm (ECA) filter. Basically the interfering signal in the surveillance signal will be projected into a subspace orthogonal to the reference signal, such that after correlation of reference and surveillance signal the interference will be rejected. The computational load for this is very high, as this needs to be done for every scatterer (i.e. delay) and theoretically for every Doppler shift. In practice this needs to be done only for the Doppler frequency of the direct signal and a small extent in order to suppress sidelobes of the direct signal.
In [47] an adaption of the ECA for digital modulated signals was presented: the

[1] Due to the receiver's movement it holds: $f_{\mathrm{DSI}} \neq 0$, therefore the sidelobes of the DSI restricts detection of targets with similar Doppler $f_{Tgt} \approx f_{\mathrm{DSI}}$

Extensive Cancellation Algorithm By Carrier (ECA-C). The demanding processing requirements could be reduced by processing the received data on a carrier basis in frequency domain. This is possible, as the complex values of the data carriers of an OFDM symbol are independent of their delay relative to the direct path, i.e. a processing of the ECA-C for delays is not required. As input signal serves the surveillance signal and for estimation of the filter the values are obtained from the decoded reference signal.
The ECA-C was further extended to Extensive Cancellation Algorithm By Carrier And Doppler Shift (ECA-CD) in [37]. The ECA-CD widens the filter notch of the ECA-C to suppress small Doppler shifts (which arise due to ICM and sidelobes). The filtered signal S'_{surv} is given as:

$$S'_{\text{surv}} = \mathbf{I} - P_{k,d} = \mathbf{I} - Q_{k,d}(Q_{k,d}^H Q_{k,d})^{-1} Q_{k,d}^H \tag{5.21}$$

where $P_{k,d}$ is the matrix which projects the surveillance signal into a subspace orthogonal to the clutter interference. $\mathbf{I}$ is a diagonal matrix with 1 on the main diagonal. $Q_{k,d}$ is the expanded clutter subspace matrix and given as:

$$Q_{k,d} = \begin{bmatrix} \Lambda^H Q_k & Q_k & \Lambda Q_k \end{bmatrix} \tag{5.22}$$

Λ is a diagonal matrix which shifts the clutter subspace Q_k observed at zero-Doppler frequency to higher Doppler frequencies, such that the Doppler filter notch is expanded. The main diagonal values are: $\Lambda[l] = \exp\left(j2\pi f_{\text{ECA-CD}} l T_S\right),\ l = 0, 1, \ldots, N$.

Implementation For the evaluation the ECA-CD was implemented.
In [46] it is stated, that the performance of the ECA decreases with increasing duration of the CPI, which is due to slowly time-varying clutter (i.e. ICM and non-stationary channel transfer function over time). However, this is not an issue in the processing and data evaluation using the ECA-CD here, as as input signal the decoded reference signal $\hat{S}_{Tn}$ serves, which is independent of ICM due to the removal of the channel characteristics.
Fig. 5.21 shows a flowchart of the processing including the ECA-CD.

5.3.2 Results of ECA-CD

Data from Norwegian trials Fig. 5.23 shows the result after application of the RpF, flex-DPCA, SRDB calibration and DSI cancellation using the ECA-CD. For the ECA-CD a Doppler bandwidth of 1 Hz was chosen. For comparison reasons is in Fig. 5.22 the result for the same data, but withouth ECA-CD application reported. Apparently, the ECA-CD is able to completely suppress the DSI, but apart of an improvement in sidelobe suppression in near bistatic range, the overall effect in the range-Doppler map is marginal.

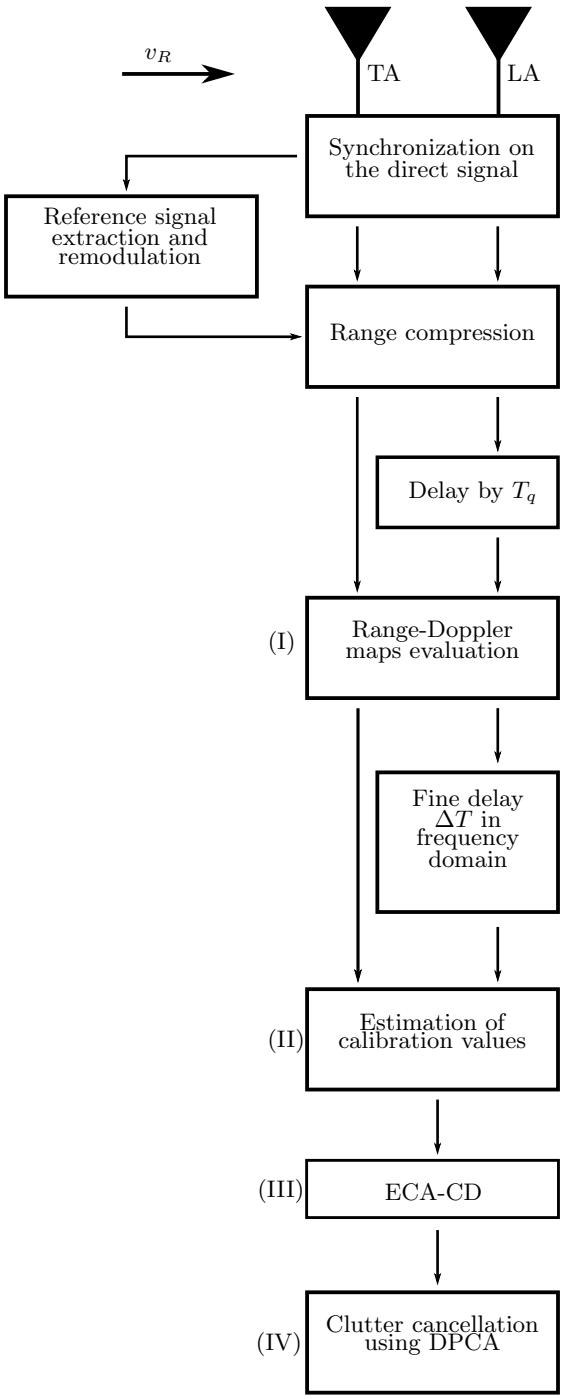

Fig. 5.21: Flowchart of the processing including the "flex-DPCA", calibration, and DSI filtering using the ECA-CD.

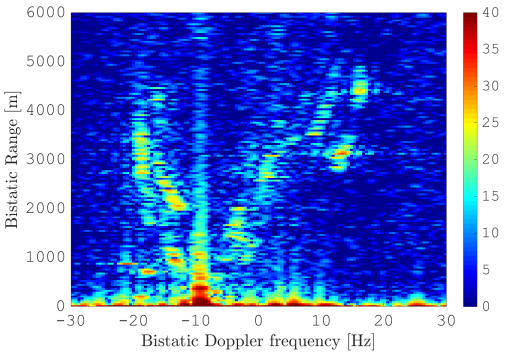

Fig. 5.22: Range-Doppler map after RpF and DPCA without DSI suppression.

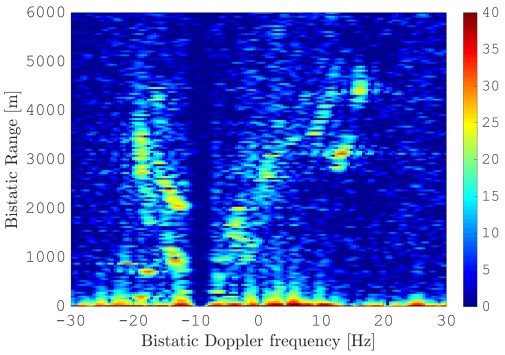

Fig. 5.23: Range-Doppler map after RpF and DPCA with ECA-CD for DSI suppression.

5.4 Analysis of the DPCA condition

With DPCA a substantial clutter suppression can be achieved. This has been shown so far for simulations as well for evaluation of real data exemplarily for the seaborne data, see Sec. 4.2. However, in order to suppress the clutter for the ground- and air-borne trials, DPCA did not suppress the clutter in a similar way as for the sea-borne data. This can be most likely addressed to mutual coupling of the antenna elements, unknown non-ideal antenna patterns (which deviates from the assumed ideal omnidirectional pattern), a non-ideal fulfilment of the DPCA condition, and potentially ICM.
In the following the single consecutive processing steps required for DPCA are analysed in more detail. This analysis should also serve as possibility to further improve the clutter suppression by analysing deviations between the ideal expected outcome, and the actual result.
A very well known tool to study the clutter distribution is the Minimum Variance (MV) power spectrum estimation P_{MV}, also known as Capon super-resolution spectral estimation [48][49]. As known, for a pure side-looking configuration, the clutter ridge is located on a diagonal line in the Doppler-angle domain, where for a stationary TX its slope β is given as [49]:

$$\beta = \frac{v_R}{d}\mathrm{PRI} \tag{5.23}$$

The estimation of P_{MV} is given as:

$$P_{MV}(f_D, \bar{\theta}) = \frac{1}{\mathbf{s}'(f_D, \bar{\theta})\mathbf{R}^{-1}\mathbf{s}(f_D, \bar{\theta})} \tag{5.24}$$

where $\mathbf{s}(f_D, \bar{\theta})$ is a space-time steering vector for bistatic Doppler f_D and the normalized angle of arrival $\bar{\theta} = \frac{d}{\lambda}\sin\theta$. $\mathbf{R}$ defines the estimated (clutter + noise) covariance matrix.
The MV is estimated for real data from the trials on the seaborne platform, where the bistatic range $r_B = [1000, \ldots, 6000]\,\mathrm{m}$ is taken into account for estimation of $\mathbf{R}$, thus excluding the direct signal and its strong sidelobes at close bistatic range from estimation. The estimation in Doppler was done for $f_D = [-20, \ldots, 20]\,\mathrm{Hz}$, as this is slightly greater than the greatest Doppler $f_{D_{\mathrm{Cl}}}^{(\max)}$ to be expected from clutter: $f_{D_{\mathrm{Cl}}}^{(\max)} = v_R/\lambda \approx 18.5\,\mathrm{Hz}$.
Before estimation, diagonal loading was used in order achieve convergence of the matrix inversion in (5.24) and to improve the estimation [50]. Although only two elements were used, which leads to a coarse angular resolution, it gives still a good impression of the clutter distribution. The MV spectrum is shown in Fig. 5.24. In Fig. 5.24 a diagonal yellow line with slope β indicates the position and the slope

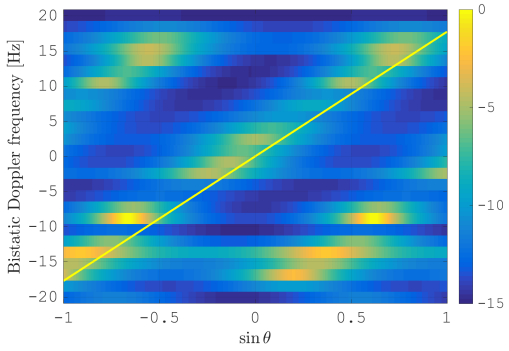

Fig. 5.24: MV power spectrum of data from the seaborne trials at the beginning of the processing chain.

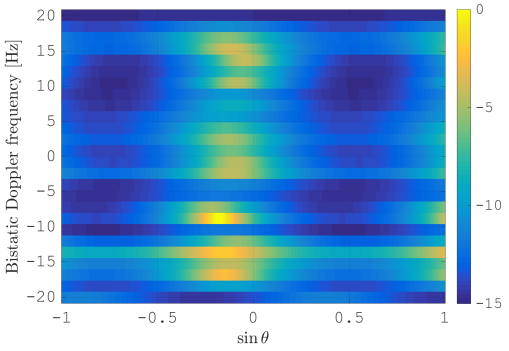

Fig. 5.25: MV power spectrum of data from the seaborne trials after flex-DPCA application.

of the clutter ridge in pure side-looking condition and under ideal circumstances. First one can see, that the slope of the clutter ridge follows the ideal slope very close.

However, the clutter ridge is somewhat shifted with respect to the ideal line. This is indicated by the position of the direct signal in the angle-Doppler domain, which still appears as a strong contribution although being excluded from covariance matrix estimation. It can be detected as the strong peak at $\bar{\theta}_T \approx -0.63$ and $f_D \approx -7\,\mathrm{Hz}$. As the direct signal can be regarded as the return of a scatterer with a very high power, its position should ideally be as well on the ideal clutter ridge at $\sin\theta_T = \bar{\theta}_T = \frac{\lambda}{v_R} f_{D_T}$. Here this is not the case due to non-calibrated antenna patterns, receiving hardware and potentially due to non-ideal measurements of the device providing position and velocity data (i.e. in the case considered here the IMU). The second strong peak in Fig. 5.24 at $\bar{\theta} \approx +0.63$ and $f_D \approx -7\,\mathrm{Hz}$ results from a grating lobe of the antenna pattern, as the displacement normalized by λ amounts $\frac{d}{\lambda} \approx 0.78$, thus leading to grating lobes. That is, spatial undersampling occurs as described in [48, p. 108]: the ambiguous responses are shifted in azimuth (while for temporal undersampling the ambiguous responses would be shifted in Doppler frequency). The first processing step for DPCA involves the proper selection of the correct range compressed DVB-T symbols from both antenna elements to be subtracted. After having selected the correct data sets from both antennas, one can estimate the MV spectrum again for analysis. The outcome of this is shown in Fig. 5.25. One can see, that for each single Doppler bin the component of the particular clutter ridge is shifted, such that the clutter ridge is now vertical. That means, the flex-DPCA does implicitly a linear transformation of the clutter ridge, as ideally both antenna elements, LA and TA would align with their positions in space perfectly, such that both antenna elements receive signals with

the same phase from scatterers. This is different to the clutter ridge being on a horizontal line at $f_D = 0$ for a stationary platform [51, p. 27], as in the case described here movement is involved. The DPCA filter can be interpreted as a filter in angular direction with a notch at $\sin\theta = 0$, which refers to the centre of the clutter ridge. However, the lack of inter-channel calibration results in a shift of the clutter ridge with respect to the $\sin\theta = 0$ line. Therefore, the antenna elements will not align ideally in space, where this displacement leads to a phase residual after subtraction of the data of both channels which limits clutter cancellation and target detection capabilities.
The technique of digital calibration using SRDB provides a useful tool in order to correct for this residual. Applying this calibration before estimating the MV spectrum shifts the clutter ridge in angular direction towards the centre of the angular axis, thus compensating for hardware inequalities leading to a phase error ϕ_e, but it also compensates the phase difference $\phi_T = 2\pi\frac{d}{\lambda}\sin\theta_T$ in between both receiving channels due to angle of arrival θ_T of the direct signal, so that the response of the direct signal is shifted by:

$$\begin{aligned}\bar{\theta}_S = \bar{\theta}_e + \bar{\theta}_T &= \frac{d}{\lambda}\left(\sin\theta_e + \sin\theta_T\right) \\ &= \frac{\phi_e}{2\pi} + \frac{d}{\lambda}\sin\theta_T\end{aligned} \tag{5.25}$$

As the flex-DPCA has rotated the clutter ridge to a vertical position before applying the calibration, the complete clutter ridge is shifted towards the centre of the angular axis. Ideally it is now in the centre of the DPCA filter notch, and the clutter can be suppressed by simple channel subtraction. The MV spectrum after SRDB calibration is shown in Fig. 5.26. One notices that the clutter ridge is shifted towards the centre of the angular dimension along all bistatic Doppler bins, such that it is located almost symmetrically along $\sin\theta = 0$.
However, SRDB calibration only operates on the direct signal contribution at $f_{D_T} \approx -7\,\mathrm{Hz}$, and does not account for potential variations of the inter-channel calibration coefficient over Doppler (e.g. over angle). As a consequence, although the direct signal contribution is now reasonably centred at $\sin\theta = 0$, the same does not occur to the clutter ridge at other Doppler bins.
For the compensation the MV power spectrum can be used. As each single bistatic Doppler frequency bin should be ideally symmetric around the zero angle, an angular value $\bar{\theta}_i$ for each particular Doppler bin f_{D_i} can be extracted from the MV power spectrum, by which f_{D_i} needs to be shifted. After having estimated an angular value for each Doppler bin, an affine function $f_{\sin\theta}(f_D) = a_0 + a_1 f_D$ using a Least-Squares (LS) fitting method can be calculated, which can be used for residual compensation. This is shown in Fig. 5.28, where the blue dots depict the angular values $\bar{\theta}_i$ for Doppler bin f_{D_i}, and the red line depicts the estimated

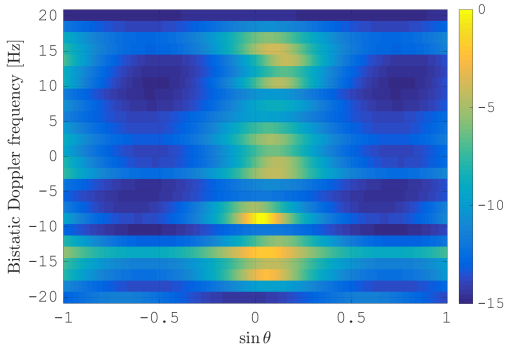

Fig. 5.26: MV power spectrum of the data from the seaborne trials after flex-DPCA and SRDB calibration.

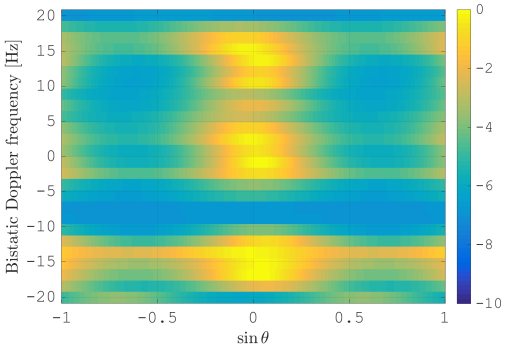

Fig. 5.27: Estimated MV spectrum after direct signal removal using the ECA-CD [37].

function $f_{\sin\theta}(f_D)$ using the LS fitting method.
Due to the trajectory and the right-looking condition, the direct signal is the strongest contribution in the data and therefore limits the dynamic range. In order to improve the estimation, it was removed beforehand using the ECA-CD. It was applied such that it cancels a bandwidth of 1 Hz centred at the Doppler f_{D_T} of the direct signal. The compensated MV power spectrum is shown in Fig. 5.27. The clutter ridge has been shifted closer towards $\sin\theta = 0$, thanks to the estimated correction function and the significantly removed direct signal contribution at $f_D \approx -7\,\text{Hz}$ prior to DPCA. Figs. 5.29, 5.30, and 5.31 show range-Doppler maps for each single processing step and DPCA. Fig. 5.29 shows the result after flex-DPCA and clutter reduction. In Fig. 5.30 the SRDB calibration was applied additionally before DPCA processing. Finally, Fig. 5.31 shows the result with the MV residual compensation using the estimated function. Although the clutter is not completely removed, an additional suppression can be seen from Fig. 5.29 to 5.31, especially for bistatic Doppler values $f_D = [-8, \ldots, +3]\,\text{Hz}$. This can also be confirmed by estimating the cancellation ratio (CR) for the range-Doppler maps. The CR between the results from Figs. 5.29 and 5.30 is shown in Fig. 5.32, and the CR between the results from Figs. 5.30 and 5.31 is shown in Fig. 5.33. Analysing Fig. 5.32 one can see, that except for strong clutter returns at $f_D \approx -15\,\text{Hz}$ and at $f_D \approx 10\,\text{Hz}$, the clutter can be reduced around 10 dB. After MV residual compensation a further reduction is achieved for some clutter regions , e.g. at $f_D = [-22, \ldots, -15]\,\text{Hz}$ and bistatic range $r_B = [2000, \ldots, 3000]\,\text{m}$ where the clutter could be reduced in between 5 to 10 dB, thus facilitating target detection, see Fig. 5.33.
It needs to be mentioned here, that the MV residual estimation is generally able to compensate as well for digital calibration inequalities, i.e. it could theoretically

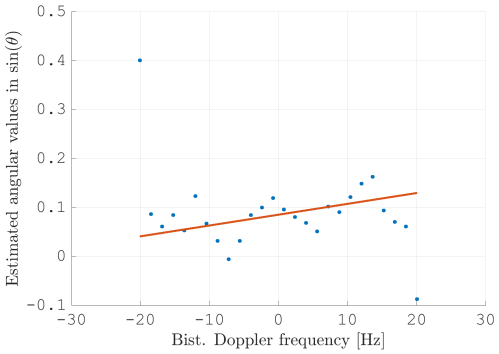

Fig. 5.28: Estimated angular values from the MV power spectrum from Fig. 5.26 after direct signal interference suppression. The red line depicts the estimated LS fitting. The outliers at Doppler frequencies where no clutter contributions can be expected were removed prior to estimation.

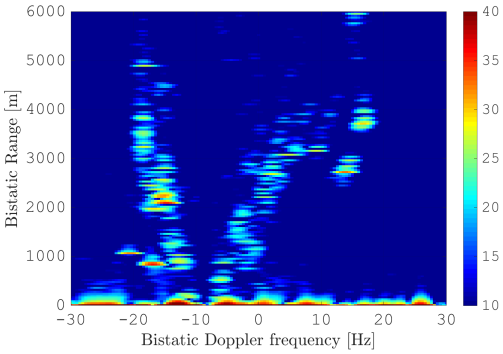

Fig. 5.29: Range-Doppler map after flex-DPCA application (DPCA applied for clutter suppression).

replace the SRDB calibration. However, by inspecting Fig. 5.25 one can detect grating lobes. If the inter element spacing d would change, maybe due to constraints such as the size of the platform or the size of the antenna elements, more grating lobes would appear. If the receiving hardware is not calibrated, e.g. a calibration is not applicable, the clutter ridge would appear shifted more. These issues could seriously affect the estimation of the angular values to be applied, as the main lobe could be mixed up with one of the grating lobes. Subsequently a wrong shift of the clutter ridge would be applied, thus possibly impeding the clutter suppression.

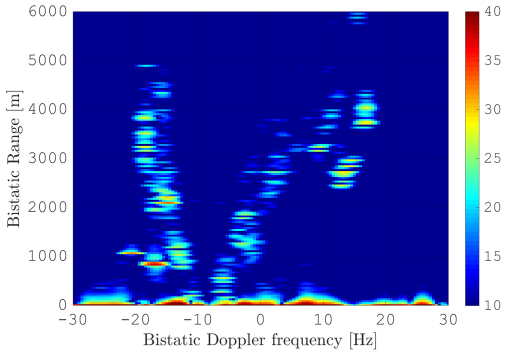

Fig. 5.30: Range-Doppler map before MV estimation and residual compensation (DPCA applied for clutter suppression).

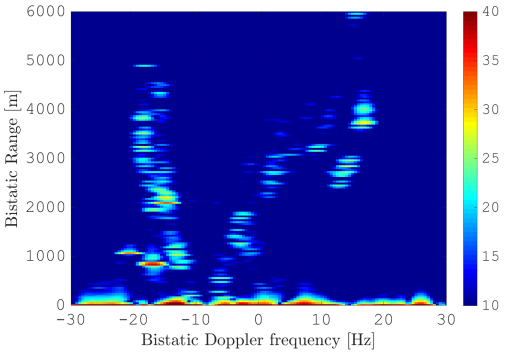

Fig. 5.31: Range-Doppler map after MV estimation and residual compensation (DPCA applied for clutter suppression).

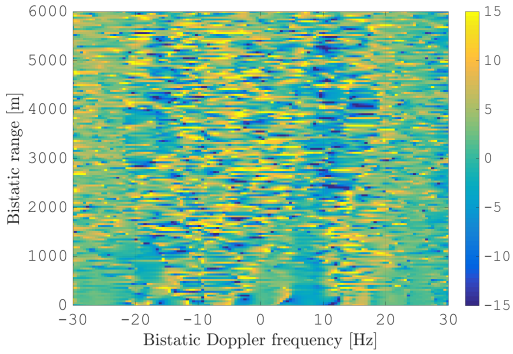

Fig. 5.32: Cancellation ratio (in dB) for range-Doppler maps shown in Fig. 5.29 and Fig. 5.30.

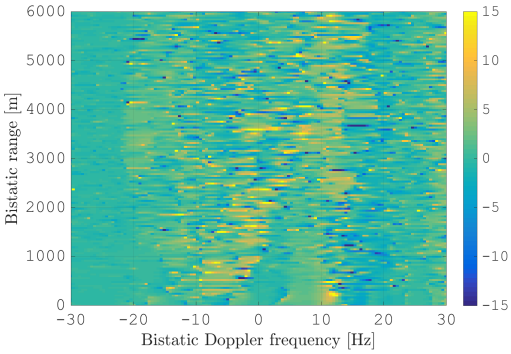

Fig. 5.33: Cancellation ratio (in dB) for range-Doppler maps shown in Fig. 5.30 and Fig. 5.31.

5.5 Comparison of DPCA to STAP

The clutter suppression technique DPCA is susceptible to calibration errors in the receiving hardware and antenna pattern. Also the non-fulfilled DPCA condition limits the detection performance.
However, STAP is adaptive to clutter returns, and up to a certain amount resistant to non-ideal conditions.
In the data from the ground-borne trials in Sec. 4.3.1, the clutter returns could not be suppressed to isolate the cooperative target, although the reference signal appeared to be very clean, the receiving channels were calibrated according to the calibration tone, and the DPCA condition was fulfilled. A reason might be that the returns from forests and trees have a high ICM, so that the returns at different time stamps at the displaced antenna elements are not coherent. A solution could be to apply another STAP technique, as this might be adaptive to the clutter returns. The results of the *Adjacent-bin Post-Doppler* STAP [20] is applied on the data evaluated in 4.3.1 using two guard gates, and 24 training gates on both sides. In order to have a fair comparison between the results of the *Adjacent-bin Post-Doppler* STAP and the results from flex-DPCA, only two out of the four antenna elements were selected for processing.
The results are shown in Fig. 5.34 for the MF and in Fig. 5.35 for the RpF. The difference and amount of clutter suppression compared to the results after DPCA application shown in Sec. 4.3.1 are obvious. The clutter is over the whole range-Doppler map almost completely suppressed. Fig. 5.36 and Fig. 5.37 shows a zoom into the Figs. 5.34 and 5.35 at the location of the cooperative target. Apparently, the application of the RpF is also advantageous compared to the MF for clutter suppression. As in the MF application the compression artefacts and residuals from the non-deterministic components will spread all-over the range-Doppler map, this affects also the estimation of the covariance matrix for estimation of the weight vector for clutter filtering. Therefore is the weight vector not ideally adaptive on the clutter, and does not suppress the clutter completely.
In contrast the application of the RpF provides a time-invariant impulse response which allows for the weight vector to be ideally adaptive on the clutter.
The disadvantages of STAP must be mentioned here: although the adaptivity on the clutter provides good clutter suppression performance, the performance is very susceptible to the parameters being chosen, i.e. number of guard gates and number of training gates. These values must be chosen carefully, as these values have a strong influence on the performance.
Another disadvantage can be seen in the range-Doppler maps: at some range and Doppler bins clutter remains, especially at range-Doppler bins which are extended across the range-Doppler map horizontally, e.g. at bistatic Doppler $f_D = [-20, \ldots, 0]$ Hz and bistatic range $r_B = [2000, \ldots, 3000]$. For these clutter

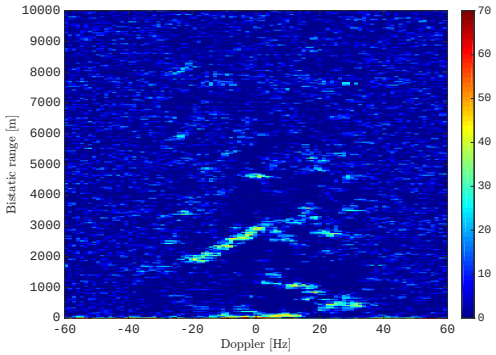

Fig. 5.34: Range-Doppler map in dB after STAP and matched filtering.

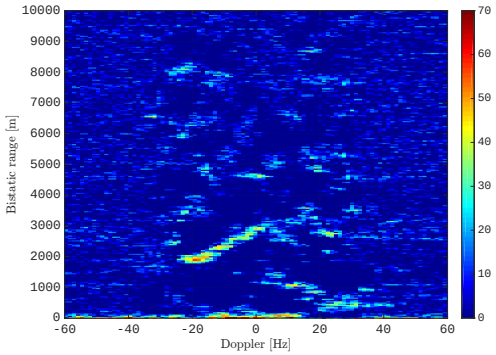

Fig. 5.35: Range-Doppler map in dB after STAP and reciprocal filtering.

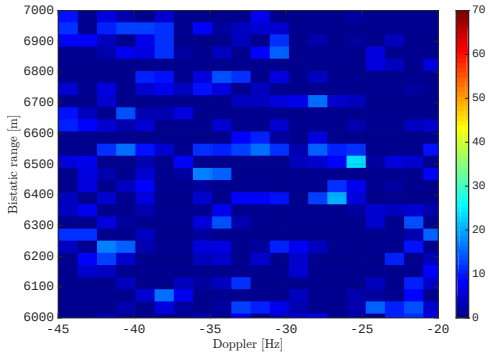

Fig. 5.36: Enlarged view for the region of the cooperative target for Fig. 5.34.

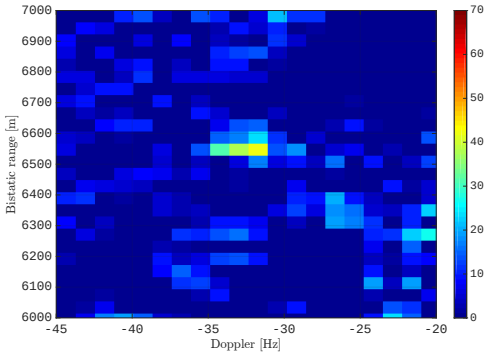

Fig. 5.37: Enlarged view for the region of the cooperative target for Fig. 5.35.

returns, there does not exist a sufficient number of training gates for the estimation of the covariance matrix and therefore the clutter is not removed.

Chapter 6

Further work

6.1 Co-Channel Interference

As described in Sec. 2.2, the DVB-T transmitters in Germany are organised in so-called Single Frequency Network (SFN). In contrast to a ground-based PCL receiver, an airborne PCL receiver will receive the transmissions from SFNs transmitting at the same frequency as the SFN from the IO. This is because the higher operating altitude results in LOS to the interfering source (i.e. the other SFNs), and - as the wave travels in free space - there are no masking and shading effects because of the terrain. The reception of more than one signal in the same frequency band from different SFNs may dramatically impede the recovery of the waveform and can therefore be regarded as wideband noise jamming or Co-channel Interference (CCI).
Dependent on the received power of the CCI and the received power of the signal from the IO, reference signal reconstruction can be made impossible or at least impeded severely, thus hindering target detection. It also degrades the quality of SAR images based on PCL, which has been demonstrated in [9].
The problem of CCI for airborne PCL using Advanced Television Standards Committee (System A) (ATSC) waveforms has previously been shown theoretically in simulations [52].
However, up to now there did not exist any open publication, which justifies this issue based on real data. Therefore a measurement campaign on an air-borne receiver was organised, in order to acquire data to gain experience with this kind of problem. However, based on the reception of signals modulated according to the same standard, e.g. DVB-T, it is not possible to differentiate between the SFNs. But Germany is in the progress of soft-switching from DVB-T to DVB-T2, which means, DVB-T stations in densely populated and metropolitan areas were switched to DVB-T2 first, while stations serving the countryside will follow later. By the

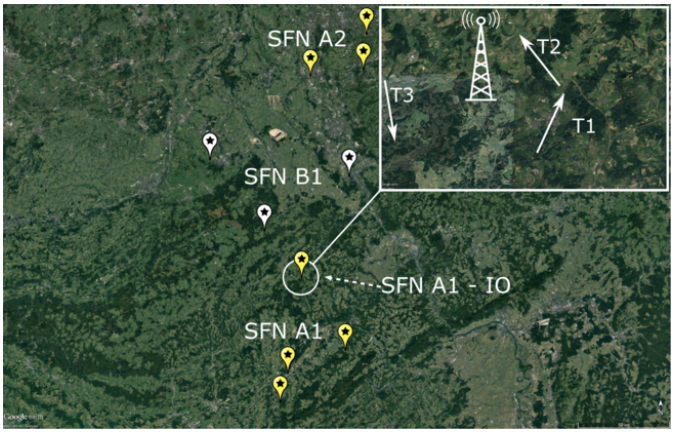

Fig. 6.1: Map of the region with some annotated SFNs. The IO is marked with *SFN A1 - IO*. A zoom into the region around the IO is shown in the upper right corner where the trajectories of the airborne receiver are labeled with T1, T2, and T3. *Image source: Google Earth.*

finalisation of this Thesis, this progress is supposed to be finished. This means, that there was the simultaneous transmission of DVB-T and DVB-T2, which is a favourable possibility: To recall, a single DVB-T channel occupies a bandwidth of 8 MHz of which it uses 7.61 MHz to transmit on 6817 subcarriers in the 8k mode [12]. The newer standard of DVB-T2 is more flexible than the DVB-T standard. For example it can transmit using an extended 16k or 32k mode, which means the emitted signal occupies 13921 or 27841 carriers in the bandwidth of 8 MHz [53]. By doing so the occupied bandwidth is extended by 0.16 MHz compared to the 8k mode of DVB-T. This gives the chance to differentiate between the DVB-T and the DVB-T2 signals in frequency domain and gives therefore the possibility to indicate the strength of the CCI as long as the DVB-T2 is weaker than the DVB-T signal.

Trial site As campaign site a location close to the trials described in Sec. 4.3 was chosen. The exploited IO is the transmitter "Eifel / Scharteberg", which is also exploited as IO for the trials described in Sec. 4.3. Fig. 6.1 shows a map of the measurement campaign site and the surrounding region with annotations to mark the exploited IO and some surrounding SFNs. The SFNs are labelled with SFN A1, A2, and B1, where the letter indicates SFNs using common frequencies, and the cypher indicates a running number in order to differentiate between distributed SFNs. In fact there are more SFNs transmitting at the same or at other frequencies around the considered illuminator of opportunity, but in order

to show the principle and to keep Fig. 6.1 clear, only two other SFNs are depicted in Fig. 6.1. Close to the centre of Fig. 6.1 one TX is marked with SFN A1 – IO, which is the transmitter "Eifel / Scharteberg". The SFN in the northern part of the map labelled with SFN A2 is an SFN transmitting at the same frequencies as SFN A1. It is located in and around the densely populated area of the city *Düsseldorf*, and transmits a signal modulated according to the DVB-T2 standard. A zoom into the region around TX Eifel is provided in the upper right corner of Fig. 6.1. The white arrows define trajectories the airborne receiver was flying.

Receiving system The receiving system used in the airborne measurement consisted of a front-end and a back-end. The back-end consists of the system "Parasol", described in Sec. 4.1.
The front-end consisted of two antennas. Each antenna was connected to one of the two receive channels of the receiving hardware. For the antennas discone elements were chosen, which have a pattern omnidirectional in azimuth. Furthermore an IMU with GNSS antennas was included providing accurate platform position truth data. The front-end was mounted in the pod. The pod together with equipment mounted inside of it is shown in Fig. 6.2. It shows both antennas at the bottom, the IMU in the centre of the pod and RAM mounted on the opposite side, which was used to achieve a signal attenuation towards the IO in order to prevent damaging of the hardware equipment due to an expected strong direct signal from the IO. A strong direct signal was expected due to the close range to the TX; and the exact strength of the direct signal could not be determined due to the unknown tilting of the transmit antennas, and due to unknown weather conditions, e.g. rain or fog, which put a constraint on the flight altitude. The RAM was not matched to the UHF wavelengths, but due to the restricted size of the pod, the space for mounting the equipment was limited. The equipment all together is mounted on a plate consisting of plastic material. The plate itself is mounted in the interior of the pod. In between the ground plate and the pod a gap of approximately 5 cm was left in order to have space for two GNSS antennas needed for the IMU. Fig. 6.2 shows the pod upside-down, which means the pod was flipped around the longitudinal axis to be mounted on the bottom of the airplane's wing.
The ULA with the pod mounted below the wing is shown in Fig. 6.3.
The receiver was flying on a circular-like path around the TX and recorded data when flying on trajectories marked by the white arrows which are labelled with T1, T2, and T3 in Fig. 6.1. For the results shown in this section, the receiver was flying along trajectory T2 (see Fig. 6.1) with an average velocity of 45 m/s at an average altitude of 1220 m above sea level. In Fig. 6.4 the spectrum of one receiving channel for this trajectory is shown. The DVB-T channels at carrier

Fig. 6.2: Image of the measurement equipment: The pod, two spider elements (at the bottom), IMU, and RAM to prevent hardware damaging from a strong direct signal.

Fig. 6.3: The ULA with the pod mounted below the right wing.

frequencies $f_T = 674\,\text{MHz}$ and $f_T = 690\,\text{MHz}$ are those occupied by the TX Eifel. One particular detail is the appearance of other DVB-T channels at $f_T = 666\,\text{MHz}$ and $f_T = 698\,\text{MHz}$. These are transmitted from a neighbouring SFN, most likely from the SFN labelled with $B1$ in Fig. 6.1.
Fig. 6.5 shows a zoom into the recorded DVB-T channel at $f_T = 690\,\text{MHz}$. Together with the DVB-T channel a DVB-T2 channel was recorded on the same carrier frequency f_T. The red line indicates the start of a DVB-T spectrum, which is supposed to be at $f_S = f_T - \frac{1}{2}\frac{K-1}{T_U}$. Here in the analysed case $f_S \approx 686.2\,\text{MHz}$ for $f_T = 690$ MHz, K equals the number of subcarriers $K = 6817$, and T_U represents the duration of the useful part of a DVB-T symbol $T_U = 896\,\mu\text{s}$. It can be seen from the figure that the spectrum is extended over the bandwidth of the DVB-T spectrum by approximately 0.08 MHz down to 686.12 MHz, indicated by the black line.
The bandwidth extension of $\text{BW}_{\text{ext}} = 0.08\,\text{MHz}$ can result either from the 16k extended carrier mode or from the 32k extended carrier mode of DVB-T2 [53]. This result shows a clear example of CCI received by an airborne passive radar. The DVB-T2 signal was most likely transmitted by the SFN located at the region of Düsseldorf, see Fig. 6.1, where it is labelled as SFN A2.
The overlap of DVB-T and DVB-T2 can also be observed for the spectra at $f_T = \{666, 674, 682, 698\}\,\text{MHz}$.

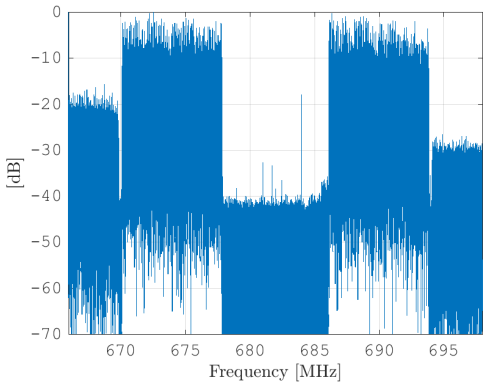

Fig. 6.4: The 32 MHz wide recorded spectrum at trajectory T2.

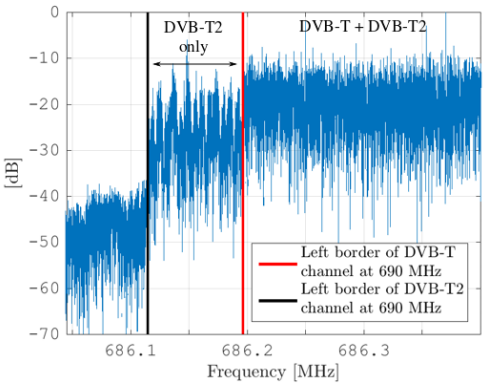

Fig. 6.5: Zoom into the left border of the DVB-T channel at $f_T = 690\,\text{MHz}$. The red line and the black line indicate the left end of the occupied spectrum by the DVB-T channel and the DVB-T2 channel respectively.

Suppression of Co-Channel Interference To demonstrate the impact of CCI on reference signal estimation, an initial attempt at estimating the reference signal without any prior CCI suppression is performed first. The first estimation is done with the received signal $Y^{(\text{LA})}(f)$ from the LA. In Fig. 6.6 the constellation maps for four DVB-T symbols are shown. TX Eifel uses 16-QAM, but this constellation format can not be recognized in Fig. 6.6. A range-Doppler map for a CPI of 512 DVB-T symbols is shown in Fig. 6.7. One can see the returns of strong clutter sources (e.g. from man-made objects, forest, and trees), but overall the range-Doppler map is covered with a high noise.

To improve the reference signal estimation here a first approach to suppress the CCI is shown. This approach is based on exploiting the frequencies where only a DVB-T2 signal is received. The received signal $Y^{(\zeta)}(f)$ on antenna $\zeta = [\text{LA}, \text{TA}]$ can be described in frequency domain as:

$$Y^{(\zeta)}(f) = H^{(\zeta)}(f)X(f) + H_I^{(\zeta)}(f)X_I(f) + N^{(\zeta)}(f) \tag{6.1}$$

where $X(f)$ defines the transmitted DVB-T signal from TX Eifel and $X_I(f)$ defines the CCI source, i.e. the transmitted DVB-T2 signal. $H^{(\zeta)}(f)$ and $H_I^{(\zeta)}(f)$ define the channel transfer function for the DVB-T signal and the interfering DVB-T2 signal respectively at antenna n. $N^{(\zeta)}(f)$ defines AWGN.

The transmission of DVB-T2 in extended bandwidth gives the opportunity to suppress the DVB-T2 signal, using the subcarriers on frequencies occupied only by the DVB-T2 signal. By formulating a minimization problem one can use these

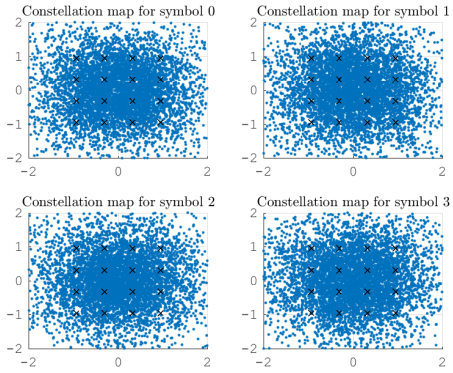

Fig. 6.6: Constellation map of four OFDM symbols before CCI suppression. The black crosses indicate the positions of the ideal constellation points.

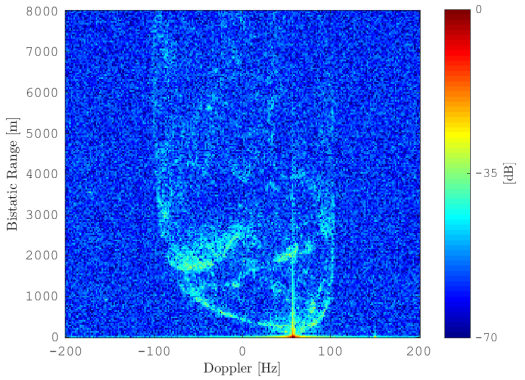

Fig. 6.7: Range-Doppler map before CCI suppression.

subcarriers and both antennas to estimate suitable values to suppress the CCI. The domains and codomains of $X(f)$ and $X_I(f)$ are defined in (6.2) and (6.3):

$$X(f) = \begin{cases} \neq 0, & \text{for } f \in F_E \\ = 0, & \text{for } f \notin F_E \end{cases} \tag{6.2}$$

$$X_I(f) = \begin{cases} \neq 0, & \text{for } f \in F_I \\ = 0, & \text{for } f \notin F_I \end{cases} \tag{6.3}$$

where:

$$F_{BW} = \left[-\frac{7168}{2T_{U_D}}, \frac{7168}{2T_{U_D}} \right], \quad F_E = \left[-\frac{K-1}{2T_{U_D}}, \frac{K-1}{2T_{U_D}} \right] \tag{6.4}$$
$$F_I = \left[-\frac{K_I-1}{2T_{U_I}}, \frac{K_I-1}{2T_{U_I}} \right], \quad F_E \subsetneq F_I \subsetneq F_{BW}$$

$K = 6817$ and $T_{U_D} = 896 \cdot 10^{-6}$ s define the number of carriers and the duration of the useful symbol part for a DVB-T symbol. $K_I = \{13921, 27841\}$ and $T_{U_I} = \{1792, 3584\} \cdot 10^{-6}$ s define the number of carriers and the duration of the useful symbol part of the extended bandwidth of a DVB-T2 symbol transmitted using the 16k and 32k mode respectively. Equation (6.4) defines frequency sets: F_{BW} defines the set of frequencies in the complete 8 MHz bandwidth. F_E defines the set of frequencies in the bandwidth occupied by the subcarriers from DVB-T and F_I defines the set of frequencies occupied by DVB-T2, where F_E and F_I overlap at the DVB-T subcarriers. The set of frequencies occupied from DVB-T2 only

is defined by: $F_T = F_I \setminus F_E$.
The minimization problem is then:

$$\underset{z \in \mathbb{C}}{\text{minimize}} \sum_{f_T \in F_T} |Y^{(\mathrm{LA})}(f_T) - zY^{(\mathrm{TA})}(f_T)|^2 \tag{6.5}$$

where z is a complex number: $z = r\exp(j\varphi)$. z is then applied on $Y^{(\mathrm{TA})}(f_E)$ on the subcarriers at the frequencies $f_E \in F_E$ in order to suppress the interfering signal by calculating the difference of $Y^{(\mathrm{LA})}(f_E)$ and $zY^{(\mathrm{TA})}(f_E)$:

$$Y_m(f_E) = Y^{(\mathrm{LA})}(f_E) - zY^{(\mathrm{TA})}(f_E) \tag{6.6}$$

The described process was done for each OFDM symbol individually.
Figs. 6.8 and 6.9 show the spectrum at the left edge and right edge of the DVB-T signal after the CCI suppression. The DVB-T2 signal is reduced by approximately 10 dB when compared to Fig. 6.5.
Assuming that by using (6.5) and (6.6), the CCI in $Y_m(f_E)$ is sufficiently suppressed while the signal of opportunity $X(f_E)$ is preserved, an estimation of the transmitted DVB-T signal $X(f_E)$ can be achieved. Constellation maps of four estimated DVB-T symbols acquired during the process of reference signal estimation are shown in Fig. 6.10. Each symbol is still noisy, but the structure of the 16-QAM is now recognizable.
A range-Doppler map of the data with suppressed CCI is shown in Fig. 6.11. The estimated reference signal was used for range-compression.
Comparing Fig. 6.11 with Fig. 6.7 the improvement is visible due to the overall reduced noise floor. A reduction of noise $\mathrm{N_{red}}$ in the exo-clutter region was calculated using:

$$\mathrm{N_{red}} = 10\log 10 \left(\frac{\sum_{f_D \in F_D} \sum_{r \in R_g} |R^{(a)}(f_D, r)|^2}{\sum_{f_D \in F_D} \sum_{r \in R_g} |R^{(b)}(f_D, r)|^2} \right) \tag{6.7}$$

where F_D are Doppler frequencies $F_D = [120, 195]$ Hz and R_g is a set of bistatic ranges $R_g = [750, 7060]$ m. $R^{(a)}$ and $R^{(b)}$ define the range-Doppler maps after and before CCI suppression. The calculated value of $\mathrm{N_{red}}$ is approximately -9.6 dB.
Suppressing the CCI allows for an improved estimate of the reference signal. The better the estimate of the reference signal is, the better are ambiguities and sidelobes of the exploited waveform removed. This effect in combination with the suppression of the CCI – which is comparable to a wideband noise jamming – leads to the reduction in noise floor and in conclusion to a better target detection performance.

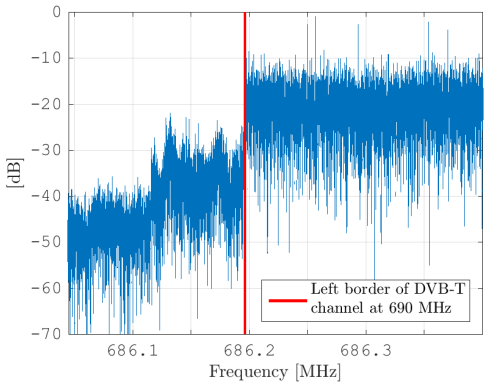

Fig. 6.8: Left side of the spectrum of the DVB-T channel after CCI suppression.

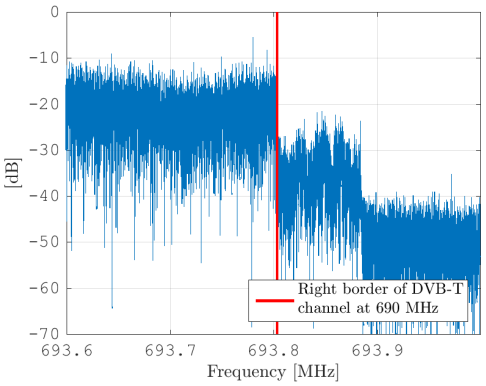

Fig. 6.9: Right side of the spectrum of the DVB-T channel after CCI suppression.

6.1.1 Conclusion

It was demonstrated with real data from an airborne platform, that the simultaneous reception of signals emitted on the same frequency as the IO mean a severe drawback for an air-borne passive radar system. A technique was suggested to reduce the interfering source (being a DVB-T2 signal), which exploits frequencies occupied only by the interfering signal in order to minimise the power of the interfering source. However, if signals are received, which are transmitted according to the same standard, this technique will not work, as it will not be possible to differentiate between the signal of opportunity and the interfering signal. To negotiate this problem, further effort and research must be done.

6.2 Range resolution improvement

6.2.1 Overview

The signals emitted by the transmitters of opportunity can also be used for imaging purposes, which has been shown for DVB-T emissions e.g. in [7], [54], and in [55] .
However, the overall bandwidth B_W of the exploited transmitter is not sufficient for high resolution purposes, as $B_W \approx 7.61\,\text{MHz}$. In fact, the range resolution of an imaging radar is inversely proportional to the signal bandwidth. In contrast, the cross-range resolution of an imaging radar is mainly limited by the along-track synthetic aperture, so that fine cross-range resolution values are theoretically achievable also by a PCL SAR.

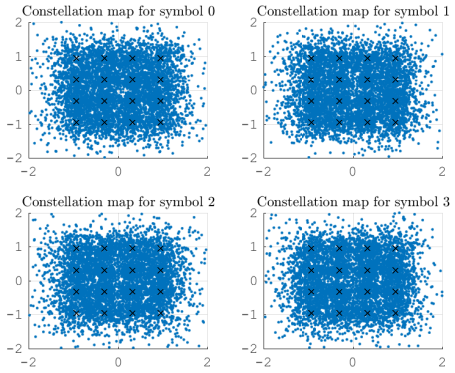

Fig. 6.10: Constellation map of four OFDM symbols after CCI suppression. The black crosses indicate the positions of the ideal constellation points.

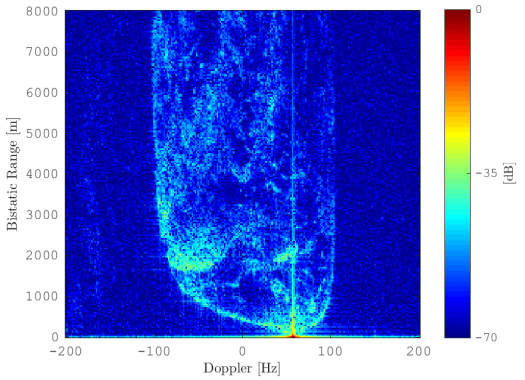

Fig. 6.11: Range-Doppler map after CCI suppression.

The range resolution of a PCL SAR can be improved by simultaneous processing of multiple adjacent received signals (for instance adjacent DVB-T channels), or by exploiting a constellation of PCL receivers observing the same area on ground illuminated by a single IO. The first approach is not always viable since there might not be multiple available signals so close that a coherent combination is possible. In contrast, the second approach is much more feasible. The problem of defining multiple trajectories that improve SAR range resolution has been already addressed for the conventional active radar case, [56], [57]. In [58] also the impact of trajectory errors are analysed. In addition, in [59], the idea has been applied to simultaneous operation of a constellation of multiple PCL receivers, where the geometry is defined by resorting to the K-space occupancy of the multiple bistatic received signals.

6.2.2 Range resolution improvement principle

In order for the range resolution improvement to be feasible, two air-borne receivers and one stationary DVB-T TX are exploited. The position of the IO is indicated with $\mathbf{T} = [x_T, y_T, z_T]^\dagger$, and with $\mathbf{R}_i(t_a) = [x_{R,i}(t_a), y_{R,i}(t_a), z_{R,i}(t_a)]^\dagger$ the time varying positions of multiple PCL receivers observing the same area illuminated by the IO ($i = 1, 2$ in the simplest case), where t_a indicates the slow-time, and the subscript $\dagger$ indicates the transpose operation. In addition, $\mathbf{P}_1$ indicates the position of the scene centre, which, for simplicity and without loss of generality, is assumed to be located in the origin of the considered Cartesian coordinate system.

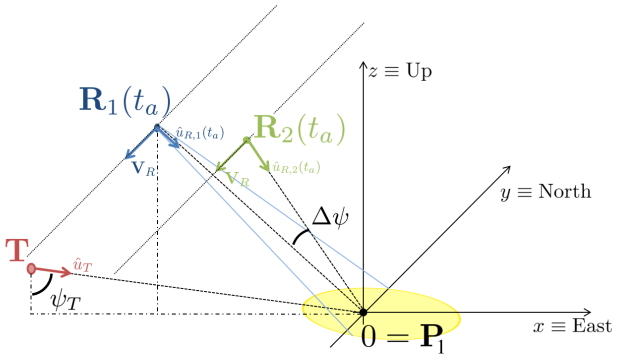

Fig. 6.12: Sketched geometry for a multi-PCL SAR with sensors moving along rectilinear trajectories.

The geometry is sketched in Fig. 6.12. Indicating with $\hat{u}_T$ the line of sight (LOS) vector from $\mathbf{T}$ to $\mathbf{P}_1$, and with $\hat{u}_{R,i}(t_a)$ the LOS unit vectors from $\mathbf{R}_i(t_a), (i = 1, 2)$ to $\mathbf{P}_1$, each bistatic observation can be equivalently represented by a monostatic one acquired on the corresponding bistatic bisectors, [11]. That is, from position

$$\mathbf{B}_i(t_a) = \frac{1}{2}\left(\mathbf{T} + \mathbf{R}_i(t_a)\right)(i = 1, 2) \tag{6.8}$$

As a consequence, the two following equivalent monostatic LOS vectors can be defined:

$$\hat{u}_{B,i}(t_a) = \frac{1}{2}\left(\hat{u}_T + \hat{u}_{R,i}(t_a)\right), i = 1, 2. \tag{6.9}$$

Recalling [60], the K-space occupancy for the two bistatic signals can be defined as

$$\mathbf{K}_{B,i}(t_a) = \left\{ k\hat{u}_{B,i}(t_a) : k \in \left[\frac{2\pi}{\lambda_{max}}, \frac{2\pi}{\lambda_{min}}\right] \right\}, i = 1, 2 \tag{6.10}$$

where k represents the wavenumber spanned by the DVB-T signal bandwidth, and λ_{min} and λ_{max} are the minimum and the maximum carrier wavelengths within the transmitted signal, respectively. Given the close dependency between K-space occupancy in (6.10) and the signal bandwidth (represented by the wavelength span $[\lambda_{\min}, \lambda_{\max}]$), it is easy to assess an inverse proportionality between $\mathbf{K}_{B,i}(t_a)$ in (6.10) and the achievable bistatic range resolution. Specifically, for SAR purposes, the ground range resolution is of interest, which directly derives from the projection of the K-spaces $\mathbf{K}_{B,i}(t_a)$ onto the (x, y)-plane, [60]. By doing so one gets:

$$\mathbf{K}_{B,i}^{(xy)}(t_a) = \mathbf{\Gamma}^{(xy)}\mathbf{K}_{B,i}(t_a) \tag{6.11}$$

where $\mathbf{\Gamma}^{(xy)} = \mathbf{I} - \mathbf{z}\mathbf{z}^{\dagger}$ is the projection onto the (x, y)-plane, $\mathbf{z}$ indicates the unit vector along the z-axis, and $\mathbf{I}$ is the identity matrix. To better understand (6.11), it can be referred to a simplified two-dimensional geometry like the one sketched in Fig. 6.13. It must be noted how this simplified geometry can be considered as a particular case of the general situation depicted in Fig. 6.12 for a specific slow-time instant $t_a = t_{a,0}$ (also referred to as mid-acquisition slow-time instant later on), where both receivers R_1 and R_2 lay on the $y = 0$ plane. Namely

$$R_1(t_{a,0}) = \begin{bmatrix} -r_{R,1}\sin(\psi_{R,1}) \\ 0 \\ r_{R,1}\cos(\psi_{R,1}) \end{bmatrix} \tag{6.12}$$
$$R_2(t_{a,0}) = \begin{bmatrix} -r_{R,2}\sin(\psi_{R,2}) \\ 0 \\ r_{R,2}\cos(\psi_{R,2}) \end{bmatrix}$$

where $r_{R,i}$ $(i = 1, 2)$ indicate the ranges of the two receivers from the origin of the considered Cartesian reference system, and $\psi_{R,i}$ $(i = 1, 2)$ indicate the corresponding incident angles. In the simplified tow-dimensional geometry of Fig. 6.13, the equivalent monostatic unit vectors $\hat{u}_{B,1}$ and $\hat{u}_{B,2}$ can be defined as:

$$\hat{u}_{B,i} = \frac{1}{2}\big(\hat{u}_T + \hat{u}_{R,1}\big) = \frac{1}{2}\left(\begin{bmatrix} u_{T,x} \\ u_{T,y} \\ u_{T,z} \end{bmatrix} + \begin{bmatrix} -\sin(\psi_{R,i}) \\ 0 \\ \cos(\psi_{R,i}) \end{bmatrix} \right), \quad i = 1, 2 \tag{6.13}$$

Consequently, the K-space signal occupancies $\mathbf{K}_{B,1}(t_{a,0})$ and $\mathbf{K}_{B,2}(t_{a,0})$ for the two bistatic acquisitions (shown in blue and green in Fig. 6.13, respectively) can be written from (6.10).
In the simplified two-dimensional geometry, the ground projection in (6.11) becomes

$$\mathbf{K}^{(x)}_{B,i}(t_a, 0) = \mathbf{\Gamma}^{(x)}\mathbf{K}_{B,i}(t_a, 0) \tag{6.14}$$

where $\mathbf{\Gamma}^{(x)} = \mathbf{I} - \mathbf{z}\mathbf{z}^{\dagger}$. Apparently (see (6.10) and (6.13)), the K-space signal occupancy in (6.14) is only dependent on the transmitter characteristics (position and signal wavelengths) and on the incident angles of the two receivers $\psi_{R,1}$ and $\psi_{R,2}$. Given that there is no control over the characteristics of the transmitter, the incident angles $\psi_{R,1}$ and $\psi_{R,2}$ are the only degrees of freedom available to correctly locate the two received signals in the K-space. Specifically, the intention is to locate them adjacent one to the other such that a wider K-space signal occupancy is achieved (see $\mathbf{K}^{(x)}_{B,(1+2)}$ in orange in Fig. 6.13). In other words, the range resolution can be improved if the (x)-plane projection of the K-space interval spanned by

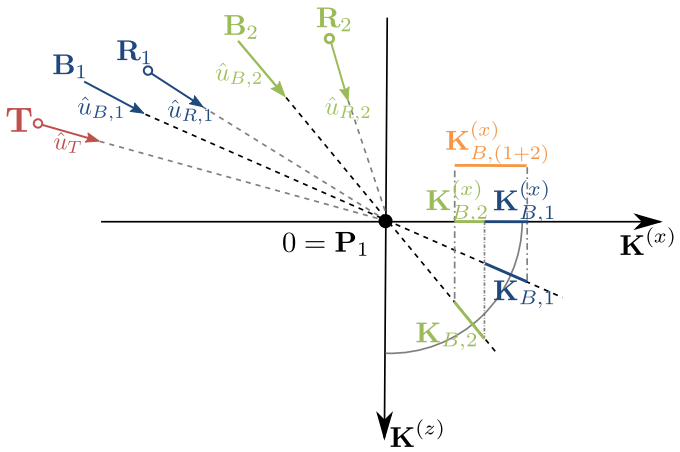

Fig. 6.13: Two-dimensional representation of K-space signal occupancy and its geometrical dependency in the bistatic case. This two-dimensional geometry corresponds to the three-dimensional geometry of Fig. 6.12, for the instant $t_a = t_{a,0}$ where relations in (6.12) apply. The dependency on $t_{a,0}$ has been removed to simplify the figure.

the first signal (namely $\mathbf{K}^{(x)}_{B,1}(t_{a,0})$) is adjacent without gaps to the (x)-plane K-space projection spanned by the second signal (namely $\mathbf{K}^{(x)}_{B,2}(t_{a,0})$), as sketched in Fig. 6.13 for a simplified two-dimensional geometry. It is easy to show that a maximum range resolution improvement can be achieved by setting the following constraint

$$\frac{2\pi}{\lambda_{max}}\mathbf{\Gamma}^{(x)}\hat{u}_{B,1}(t_{a,0}) = \frac{2\pi}{\lambda_{min}}\mathbf{\Gamma}^{(x)}\hat{u}_{B,2}(t_{a,0}). \tag{6.15}$$

This guarantees a perfect contiguity between $\mathbf{K}^{(x)}_{B,1}(t_{a,0})$ and $\mathbf{K}^{(x)}_{B,2}(t_{a,0})$ without overlap or gaps (see the contiguity in the K-space projection $\mathbf{K}^{(x)}_{B,(1+2)}(t_{a,0})$ in Fig. 6.13 for the simplified two-dimensional case). This point of perfect spectral contiguity is also referred to as "critical baseline" in SAR interferometry, see [61].

By plugging in (6.13) and (6.14) into (6.15) one gets

$$\begin{aligned}
\frac{2\pi}{\lambda_{\max}}\mathbf{\Gamma}^{(x)}\hat{u}_{B,1}(t_{a,0}) &= \frac{2\pi}{\lambda_{\min}}\mathbf{\Gamma}^{(x)}\hat{u}_{B,2}(t_{a,0}) \\
\frac{2\pi}{\lambda_{\max}}\left[\tfrac{1}{2}\left(u_{T,x}-\sin(\psi_{R,1})\right)\right] &= \frac{2\pi}{\lambda_{\min}}\left[\tfrac{1}{2}\left(u_{T,x}-\sin(\psi_{R,2})\right)\right] \\
\frac{u_{T,x}-\sin(\psi_{R,1})}{\lambda_{\max}} &= \frac{u_{T,x}-\sin(\psi_{R,2})}{\lambda_{\min}} \\
\sin(\psi_{R,2}) &= \frac{\lambda_{\min}}{\lambda_{\max}}\left(-u_{T,x}+\sin\psi_{R,1}\right)+u_{T,x}
\end{aligned} \tag{6.16}$$

which provides a direct expression to set the incidence angle of the second receiver once the transmitter and the incident angle of the first receiver are given.
The same approach can be readily extended to general three-dimensional geometry of Fig. 6.12. By doing so, the time dependency in (6.15) can be removed, since there is no need for perfect alignment in the $y = 0$ plane between transmitter and receiver for the slow-time instant $t_a = t_{a,0}$. In fact, slightly shifted trajectories in the long-track direction can be compensated and re-synchronised using simple Doppler processing. The approach here proposed for the simple case of two receivers can be readily extended to more than two receivers, with subsequent direct improvement in range resolution. It is worth mentioning that this approach has already been proposed and validated in the case of monostatic SAR with real data of a multiple pass acquisition of European Remote Sensing (ERS) radar, see [62]. A multiple input multiple output (MIMO) variation of the same approach has also been proposed in [57].

6.2.3 Scenario for multi-PCL SAR

Fig. 6.12 depicts a typical geometry multi-PCL SAR using airborne platforms, where each platform is equipped with a PCL receiver. The two platforms are supposed to fly with same velocity $\mathbf{V}_{R,1} = \mathbf{V}_{R,2} = \mathbf{V}_R$ along rectilinear trajectories observing the scene in a pure side-looking configuration. Main geometry and system parameters are reported in Tab. 6.1. Assuming the transmitter and the two receivers to be aligned in the x-axis at slow-time instant $t_{a,0}$, the optimum geometry constraint for range resolution in (6.15) applies. The resulting multistatic geometry is obtained from (6.16), leading to the parameters in Tab. 6.1. Apparently, for this simple realistic scenario, the receivers incident angles $\psi_{R,1}$ and $\psi_{R,2}$ vary less than 2°. As a consequence, a reasonable assumption on the coherence of the target backscattering between the two acquisitions can be made. As shown in Fig. 6.12 and Fig. 6.13, it would be convenient to define a geometry where the

Table 6.1: Case study geometry.

Parameter	Value
Illuminator of opportunity	DVB-T (8k mode)
Carrier frequency f_c	600 MHz
Signal bandwidth B	7.61 MHz
Transmitter incident angle ψ_T	89.9°
Height of transmitter	10 m
Distance transmitter to scene center $\lvert\mathbf{T}-\mathbf{P}_1\rvert$	12000 m
Altitude of receivers	5000 m
Receivers trajectory	rectilinear
Velocity of receivers $\lvert\mathbf{V}_R\rvert$	65 m/s
Bistatic geometry	
Receivers incident angles $\psi_{R,1},\ \psi_{R,2}$	47.98°, 46.13°
Angular separation of receivers $\Delta\psi$	1.85°

transmitter is in the back lobe of both PCL surveillance antennas. This would not only attenuate the direct signal in the surveillance channel, but it would also create a "quasi-monostatic" geometry, where the signal from the area of interest is basically back-scattered to both receivers. As a result, the bistatic iso-ranges and the bistatic iso-Doppler lines will almost be orthogonal to each other, thus creating a favourable configuration for imaging purposes, see [11]. In order this approach to be feasible, the direct signal (albeit attenuated) should be still strong enough to allow low bit error rate DVB-T digital stream decoding and signal reconstruction.

6.2.4 Simulation of DVB-T range pulse response

In this Section, the DVB-T range pulse response for a multi-PCL SAR system is analysed. Firstly, the analysis will be conducted for the scene centre $\mathbf{P}_1$, and then the effects over an extended scene will be addressed. In both these two cases, the analysis will be confined to the mid-acquisition slow-time instant $t_{a,0}$. Finally, the behaviour over an extended scene and for a rectilinear acquisition will be investigated.

Scene centre $\mathbf{P}_1$ at mid-acquisition $t_{a,0}$

Fig. 6.14 shows the spectrum in the K-space of the backscattered signal from a point target located in $\mathbf{P}_1$ received by the two receivers at slow-time instant $t_{a,0}$. As one can see, the spectra are shifted such that no gaps between the spectra are present, as expected from setting the constraint in (6.15) and (6.16). After range compressing the signal receiver from the solely first PCL sensor, the pulse

response shown as the red solid line in Fig. 6.15 is obtained. On the other hand, by coherently combining the two signals, after range compression one gets the pulse response shown as the solid black plot in Fig. 6.15. The range resolution improvement is apparent, by observing the corresponding widths of the pulse response main lobes. Tab. 6.2 reports the theoretical and measured resolutions for the single and the combined cases, respectively.

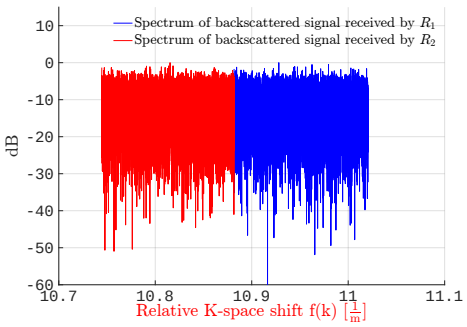

Fig. 6.14: K-space spectra of the two backscattered signals from scatterer in $\mathbf{P}_1$ at time $t_{a,0}$ projected onto (x, y)-plane [dB].

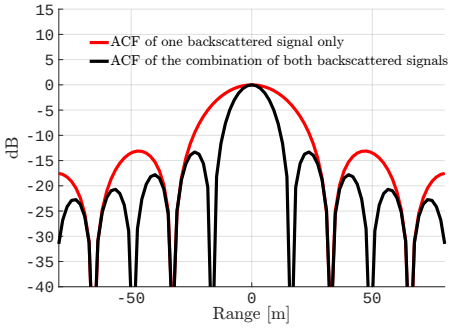

Fig. 6.15: Range pulse response (autocorrelation function (ACF)) for scatterer in $\mathbf{P}_1$ at time $t_{a,0}$: single sensor in red; two sensors combined in black [dB].

Table 6.2: Measured range resolutions for scatterer in $\mathbf{P}_1$ at instant $t_{a,0}$.

Range resolution	**Value** [m]	**Side lobe–level** [dB]
single sensor	18.8	−13.35
combined sensors	9.4	−13.26

Extended scene at mid-acquisition $t_{a,0}$

It is worth to mention that the constellation geometry (and hence the K-space shift) is calculated using (6.15) for the single point $\mathbf{P}_1$ on ground. Adjacent points will exhibit slightly different LOS unit vectors and therefore slightly different spectral shifts in the K-space, given that the constraint in (6.16) will not be fulfilled anymore. This will create a gap or an overlap between the two spectra (see Fig. 6.14). This effect has been already investigated in [63], where the variations of the wavenumber shift under strong variations of the incident angle have been analysed.

Fig. 6.16 shows a heat map of K-space signal shifts in top view of an extended scene in Cartesian coordinates. In particular, the x-axis is aligned to the along-track direction of the two platforms, and the y-axis is the ground range (see also geometry in Fig. 6.12). Compared to 6.2.4 not only one scatterer was simulated, but multiple point like targets were considered. Three points are highlighted in Fig. 6.16: $\mathbf{P}_1$, $\mathbf{P}_2$ and $\mathbf{P}_5$, whose coordinates can be found in Tab. 6.4. For every simulated scatterer $\mathbf{P}_n$ its relative K-space shift between both spectra is calculated as in (6.17):

$$\Delta f(\mathbf{P}_n) = \left(\frac{2\pi}{\lambda_{max}} \mathbf{\Gamma}^{(xy)} \hat{u}_{B,1}(t_{a,0}) - \frac{2\pi}{\lambda_{min}} \mathbf{\Gamma}^{(xy)} \hat{u}_{B,2}(t_{a,0}) \right)_{\mathbf{P}_n} \tag{6.17}$$

For each scatterer there are three possibilities of the outcome of (6.17):

1. $\Delta f(\mathbf{P}_n) = 0$: This means a perfect alignment of both spectra as shown in Fig. 6.14, and hence a fulfilment of (6.16).

2. $\Delta f(\mathbf{P}_n) < 0$: This means an overlap of both spectra.

3. $\Delta f(\mathbf{P}_n) > 0$: In this case there is a gap between both spectra.

In the first case there is an optimum in range resolution improvement achievable, whereas the second and third case result in a degradation of the performance.
Fig. 6.16 depicts $\Delta f(\mathbf{P}_n)$ colour coded as a heat map. Two regions separated by a line can be identified: a region with overlapping spectra R_{overlap} and a region R_{gap} with non-contiguous spectra. The regions are separated by a line l_0 depicted by black crosses. l_0 is the locus of points with optimum K-space spectra shift, that is no gap between both spectra. As an example, for the coordinates of $\mathbf{P}_1$ in Fig. 6.16 it holds $\mathbf{P}_1 \in l_0$, therefore $\Delta f(\mathbf{P}_1) = 0$.
$\mathbf{P}_2$ is situated in the region of the overlapping spectra, $\mathbf{P}_2 \in R_{\text{overlap}}$, therefore $\Delta f(\mathbf{P}_2) < 0$, whereas for $\mathbf{P}_5$, $\Delta f(\mathbf{P}_5) > 0$ holds as it is situated in the region of the non-contiguous spectra, $\mathbf{P}_5 \in R_{\text{gap}}$. It is here important to notice that the effects of a non-contiguous spectrum in the K-space manifest as increased side-lobes in the scatterer range pulse response, while an overlapped spectrum leads to a sub-optimal range resolution value. Given a maximum tolerated pulse response side-lobe level and a loss in the range resolution improvement, Fig. 6.16 allows to define a maximum area which can be imaged. As also stated in [63], the different incident angles over the observed scene give rise to different signal shifts in the K-space. The effects on the pulse response are clearly visible on Figs. 6.17–6.20, where a gap between the spectra produces increase in the side lobes, and while a spectra overlap leads to a non-optimum improvement of the range resolution.
Achievable ground range resolutions and sidelobe levels measured for the scatterers

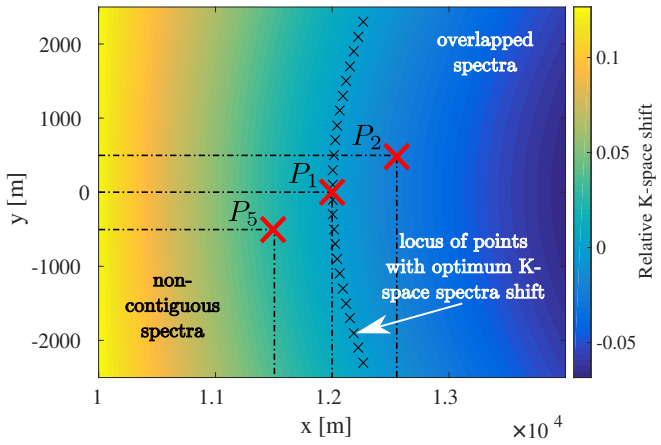

Fig. 6.16: K-space shift evaluated for the mid-acquisition slow-time instant $t_{a,0}$ over an extended scene.

in $\mathbf{P}_2$ and $\mathbf{P}_5$ at instant $t_{a,0}$ are reported in Tab. 6.3. This analysis should clearly show, which effects a relative shift in the K-space creates in the resulting range pulse response. The relative K-space spectral shift has been derived under the hypothesis of a flat terrain. Any topography in the scene would locally alternate the K-space occupancy of the corresponding echoes, thus directly affecting the relative K-space signal shift. This effect has been considered also in [63]. Unfortunately, the K-space signal occupancy can not be corrected by the topography, even if known, and this directly affects the range pulse response characteristics (similarly to what can be seen happening with $\mathbf{P}_2$ and $\mathbf{P}_5$).

Table 6.3: Measured range resolutions for scatterers in $\mathbf{P}_2$ and $\mathbf{P}_5$ at instant $t_{a,0}$.

Range resolution	**Value** [m]	**Side lobe–level** [dB]
$\mathbf{P}_2$ single sensor	19.72	−13.38
$\mathbf{P}_2$ combined sensors	10.74	−13.32
$\mathbf{P}_5$ single sensor	19.72	−13.29
$\mathbf{P}_5$ combined sensors	8.62	−9.66

Extended scene over entire acquisition

By flying a rectilinear trajectory, the optimum contiguity constraint in (6.15) cannot be kept during the entire acquisition. That is, the contiguity constraint can be set for one specific slow-time instant (for instance for the mid-acquisition instant $t_{a,0}$ as in (6.16)), but this will not be fulfilled as the platforms move along

rectilinear trajectories with constant velocity. An example of this is shown in Fig. 6.21 for the five different point scatterers located as in Tab. 6.4. In particular, the K-space shift between the two bistatic signals is shown during an acquisition corresponding to 90° of azimuth aspect angle variation. As one can see, for the scene center $\mathbf{P}_1$ and for the mid-acquisition point ($t_a = t_{a,0} = 0$) the optimum contiguity constraint is met, but the constraint deviates as the scatterer position changes or as the platform moves, leading to a gap or to an overlap between the spectra. The most annoying aspect is that the relative K-space shift is jointly a function of the slow-time t_a and of the azimuth position of the scatterers. By

Table 6.4: Positions of the five point-like scatterers in ENU.

Scatterer	**Position**
$\mathbf{P}_1$	[12000; 0; 0] m
$\mathbf{P}_2$	[12500; 500; 0] m
$\mathbf{P}_3$	[12500; -500; 0] m
$\mathbf{P}_4$	[11500; 500; 0] m
$\mathbf{P}_5$	[11500; -500; 0] m

observing Fig. 6.21, a constraint can be observed, that is never met when regarding the points $\mathbf{P}_4$ and $\mathbf{P}_5$, as they are situated in the region R_{gap} of non-contiguous spectra, compare Fig. 6.16. At the beginning of the acquisition the gap is at one of its maxima (for the duration of this acquisition); the size of the gap decreases while both receivers are moving until the minimum is reached for $t_a = t_{a,0} = 0$. The gap increases again for $t_a > 0$. The K-space shifts of points $\mathbf{P}_2$ and $\mathbf{P}_3$ show similar characteristics of their appearance, but now the relative K-space shift is negative, which means, there is an overlap between both resulting spectra. For a longer rectilinear trajectory, the amount of overlap of both spectra of $\mathbf{P}_2$ and $\mathbf{P}_3$ will decrease, until the optimum contiguity constraint will be met. From then on, the K-space shift will be positive, which results in a gap between both spectra.
As one can see, the constraint in (6.16) is met only once during the acquisition (not only for the scene centre $\mathbf{P}_1$), when a rectilinear trajectory is flown. The variation of the relative K-space shift for a given scatterer position leads to a varying range pulse response characteristic (namely range resolution) during the slow-time. A varying range resolution over slow-time would remain even after complete SAR processing, leading to a non-uniform resolution over the final focused image. This contrasts with common SAR images requirements that impose constant uniform resolutions (not only in range, but also between range and azimuth dimensions) to improve visual understanding of the scene to be imaged.
Therefore, in the next section a new trajectory will be defined.

6.2.5 Optimal trajectories for multi-PCL SAR

It will be firstly considered the trajectory of a single platform, let's say the one indicated with $\mathbf{R}_1(t_a)$. It will be shown that, to guarantee a constant width of $\mathbf{K}_{B,1}^{(xy)}$ over the slow-time t_a (that is a constant ground range resolution), the platform's trajectory must lay on a cone surface centred in $\mathbf{P}_1$. By setting the additional constraint of a constant flying altitude, the circular trajectory will be derived.
Secondly, given the first platform trajectory to be circular, the trajectory of the second platform will be derived by imposing the constraint in (6.15) for the whole slow-time t_a. That is, by imposing $\Delta f(\mathbf{P}_1) = 0 \; \forall \; t_a$.

6.2.6 Derivation of a circular trajectory

For simplicity, the dependency on the slow-time t_a is neglected here. The locus of points $\mathbf{B}_1$ (compare (6.8)) that ensures a constant ground range resolution for the scene centre point $\mathbf{P}_1$ is given as the locus of points where the corresponding K-space projections $\mathbf{K}_{B,1}^{(xy)} = \frac{2\pi}{\lambda}\left[u_{B,1}^{(x)}, u_{B,1}^{(y)}, 0\right]^\dagger$ ($\lambda \in [\lambda_{min}, \lambda_{max}]$) have constant width. The squared distance between the two edges of $\mathbf{K}_{B,1}^{(xy)}$ can be written as

$$\begin{aligned} d_{B,1}^{(xy)}(\lambda_{min}, \lambda_{max})^2 = &\left(\frac{2\pi}{\lambda_{min}} u_{B,1}^{(x)} - \frac{2\pi}{\lambda_{max}} u_{B,1}^{(x)}\right)^2 \\ &+ \left(\frac{2\pi}{\lambda_{min}} u_{B,1}^{(y)} - \frac{2\pi}{\lambda_{max}} u_{B,1}^{(y)}\right)^2 \end{aligned} \tag{6.18}$$

By setting

$$d_{B,1}^{(xy)}(\lambda_{min}, \lambda_{max})^2 = C_1 \tag{6.19}$$

being C_1 a constant greater than 0, and by indicating

$$\hat{u}_{B,1} = -\frac{1}{r_{B,1}} \cdot [x_{B,1}, y_{B,1}, z_{B,1}]^\dagger \tag{6.20}$$

and with

$$r_{B,1} = \sqrt{x_{B,1}^2 + y_{B,1}^2 + z_{B,1}^2}, \tag{6.21}$$

(6.19) becomes

$$x_{B,1}^2(1 - C_2) + y_{B,1}^2(1 - C_2) - C_2 z_{B,1}^2 = 0, \tag{6.22}$$

with $C_2 = \frac{C_1}{2\pi\left(\left(\frac{1}{\lambda_{max}} - \frac{1}{\lambda_{min}}\right)\right)^2}$. The locus of points described in (6.22) represents a cone, and specifically it states the position of the "equivalent monostatic acquisition" $\mathbf{B}_1$. From the locus of points in (6.22) it is possible to derive the locus of points of the receiver $\mathbf{R}_1$. To do this, a second Cartesian coordinate system (x'_T, y'_T, z'_T) centred in the position of the transmitter is considered. The linear transformation from $(x_{B,1}, y_{B,1}, z_{B,1})$ to (x'_T, y'_T, z'_T) is given by

$$\begin{aligned} x'_T &= x_{B,1} - x_T \\ y'_T &= y_{B,1} - y_T \\ z'_T &= z_{B,1} - z_T \end{aligned} \tag{6.23}$$

The cone in (6.22) can be expressed in (x'_T, y'_T, z'_T) as

$$(x'_T + x_T)^2(1 - C_2) + (y'_T + y_T)^2(1 - C_2) - C_2(z'_T + z_T)^2 = 0. \tag{6.24}$$

It can then be noticed by (see (6.9)), that in (x'_T, y'_T, z'_T) the coordinates of $\mathbf{R}_1$ are simply doubled of those of $\mathbf{B}_1$. As a consequence, the locus of points for the receiver $\mathbf{R}_1$ that ensure a constant ground range resolution can be written (in $(x'_{R,1}, y'_{R,1}, z'_{R,1})$) as

$$\left(\frac{x'_{R,1}}{2} + x_T\right)^2 (1 - C_2) + \left(\frac{y'_{R,1}}{2} + y_T\right)^2 (1 - C_2) - C_2 \left(\frac{z'_{R,1}}{2} + z_T\right)^2 = 0 \tag{6.25}$$

which is also a cone. By setting the flight altitude of $\mathbf{R}_1$ constant, one gets a circular trajectory for the receiver $\mathbf{R}_1$.

6.2.7 Derivation of second platform trajectory

For analogy with the first platform, it is clear that also the second platform trajectory should lay onto a cone, if the constant ground range resolution constraint has to be met. Here, in addition, it is derived the trajectory of the second platform $\mathbf{R}_2$ as a function of the first platform trajectory. To do this, the optimum contiguity constraint in (6.15) has to be set, leading to

$$\begin{aligned} x_{R,2} &= \left[\frac{\lambda_{min}}{\lambda_{max}}\left(\frac{x_T}{r_T} + \frac{x_{R,1}}{r_{R,1}}\right) - \frac{x_T}{r_T}\right] \cdot r_{R,2} \\ y_{R,2} &= \left[\frac{\lambda_{min}}{\lambda_{max}}\left(\frac{y_T}{r_T} + \frac{y_{R,1}}{r_{R,1}}\right) - \frac{y_T}{r_T}\right] \cdot r_{R,2} \end{aligned} \tag{6.26}$$

where $r_T = |\mathbf{T}|$, $r_{R,1} = |\mathbf{R}_1|$, and $r_{R,2} = |\mathbf{R}_2|$. Clearly, due to the circular nature of both trajectories, $r_{R,1}$ and $r_{R,2}$ are constant.

Table 6.5: Optimum trajectory parameters.

Parameter	**Value**
Illuminator of opportunity	DVB-T (8k mode)
Carrier frequency f_c	600 MHz
Signal bandwidth B	7.61 MHz
Transmitter incident angle ψ_T	89.9°
Height of transmitter	10 m
Distance transmitter to scene center	12000 m
Altitude of receivers	5000 m
Receivers trajectory	circular
Velocity of receiver 1 $\lvert\mathbf{V}_{R,1}\rvert$	68.778 m/s
Velocity of receiver 2 $\lvert\mathbf{V}_{R,1}\rvert$	65 m/s
Bistatic geometry	
Receivers incident angles $\psi_{R,1},\ \psi_{R,2}$	47.98°, 46.13°
Angular separation of receivers $\Delta\psi$	1.85°

6.2.8 Extended scene over entire acquisition

Fig. 6.23 shows results of the relative K-space shift for five point-like scatterers when both receivers are flying a circular trajectory. A top-view of the geometry is shown in Fig. 6.22. The K-space is evaluated for the slow-time $t_a = [-15, \ldots, +15]\,[s]$. $t_a = 0$ refers to the point of acquisition where $y_{R,1} = y_{R,2} = 0$, that is, the scenario described in Sec. 6.2. The solid line in Fig. 6.22 depicts the receivers' trajectory flown during this time interval. For illustration purposes, the trajectory is extended with a dashed line.
First the trajectory of receiver $\mathbf{R}_2$ with reference to the point scatterer $\mathbf{P}_1$ at $(12000, 0)\,[m]$ was created. Based on this trajectory, the path of receiver $\mathbf{R}_1$ according to (6.26) was calculated. When comparing Fig. 6.23 to Fig. 6.21, one can clearly see, that the relative K-space shift holds $\Delta f(\mathbf{P}_1) = 0$ for the complete time of acquisition for the circular trajectories. This is obviously, as $\mathbf{P}_1$ is the point of reference for this simulation and so it confirms (6.25) and (6.26). When comparing the relative K-space shifts for the points $\mathbf{P}_2$ to $\mathbf{P}_5$, one notices $\Delta f(\mathbf{P}_n),\ n \in \{2, 3, 4, 5\}$ is almost constant, although it deviates from the optimal value $\Delta f(\mathbf{P}_n) = 0$. The dependencies of the relative K-space shift upon: (i) the azimuth position of the scatterers, and (ii) the slow-time t_a are now significantly reduced (compare Fig. 6.21). The advantage coming from a non-varying relative K-space shift between the spectra is evident for the range as for the subsequent azimuth SAR processing. Specifically, a relative K-space shift which is constant during the acquisition and it only depends upon the position of the scatterer allows to define a maximum area which can be imaged, according to the requirements

on range resolution improvement degradation and side-lobe level increase (see last comment in Sec. 6.2.4). Basically, by exploiting circular trajectories, the results of Fig. 6.16 (which were obtained for the single mid-acquisition instant $t_{a,0}$ are now valid for the entire acquisition). On the other hand, a varying relative K-space shift during the acquisition affects the overall signal occupancy in the wavenumber domain (or equivalently K-space and Doppler domain). This clearly impacts the subsequent azimuth processing, as the characteristics of the azimuth pulse response of a given scatterer are directly affected.

6.2.9 Conclusion

The limited available bandwidth is a disadvantage for PCL SAR, as it leads to a low range resolution in images. It is shown that the range resolution can be improved by observing simultaneously the same area of interest with slightly different incident angles, so that the resulting received signals will appear shifted one to the other in the corresponding K-space. This offers an extremely interesting approach to improve imaging capability in constellations of PCL receivers. Furthermore, a mathematical derivation shows the optimal trajectories to be flown by the receivers, so that it is guaranteed that there is a constant relative K-space shift between the signal spectra received at the different constellation's platforms.

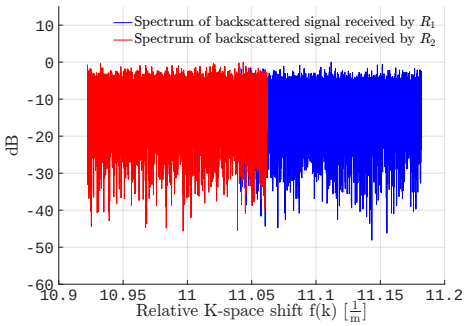

Fig. 6.17: K-space spectra of the two backscattered signals from scatterer in $\mathbf{P}_2$ at time $t_{a,0}$ projected onto (x, y)-plane [dB].

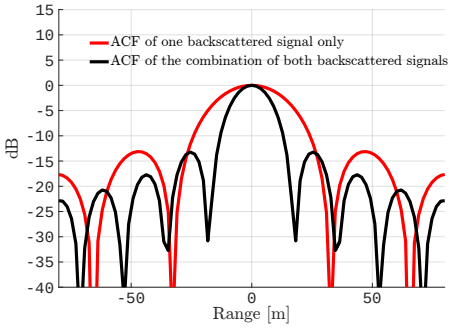

Fig. 6.18: Range pulse response (autocorrelation function (ACF)) for scatterer in $\mathbf{P}_2$ at time $t_{a,0}$: single sensor in red; two sensors combined in black [dB].

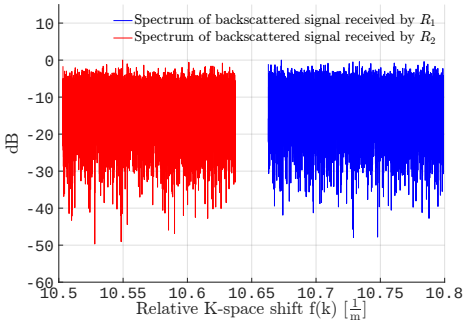

Fig. 6.19: K-space spectra of the two backscattered signals from scatterer in $\mathbf{P}_5$ at time $t_{a,0}$ projected onto (x, y)-plane [dB].

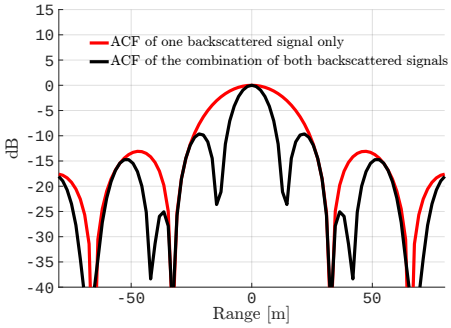

Fig. 6.20: Range pulse response (autocorrelation function (ACF)) for scatterer in $\mathbf{P}_5$ at time $t_{a,0}$: single sensor in red; two sensors combined in black [dB].

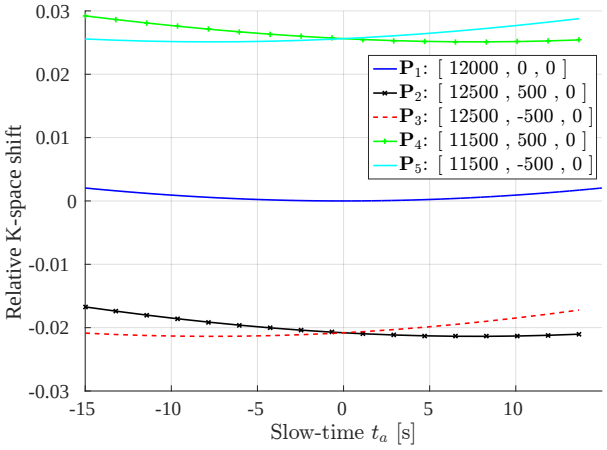

Fig. 6.21: Relative K-space shift for 5 point-like scatterers over entire acquisition: rectilinear trajectories case.

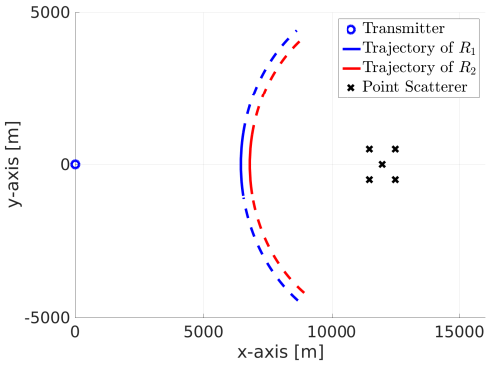

Fig. 6.22: Sample case study geometry for multi-PCL SAR with circular trajectories (top view). The position of the transmitter is marked by a circle, the crosses mark the positions of the scatterers.

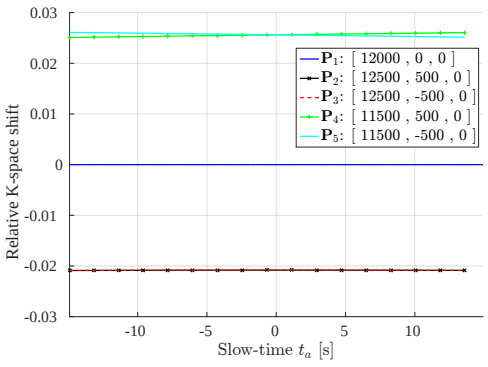

Fig. 6.23: Relative K-space shift for 5 point-like scatterers over entire acquisition: circular trajectories case.

Chapter 7

Conclusions and Future Work

7.1 Summary

As stated in the introduction of this work, the goal of this thesis was to contribute to research on passive radar on mobile platforms. The focus was on the negotiation of the limitations and impact given by the time-varying content inherent in the signal structure. Specifically, the goal of this work was to address: (i) the continuous wave operation that is intrinsic in the DVB-T passive radar and tends to provide a very limited dynamic range in the bistatic range-Doppler map; (ii) the spread of the signal sidelobes through the whole range-Doppler map caused by the platform motion. Both effects were addressed to result from the conventional processing approach, namely the matched filtering for range compression followed by a dedicated clutter suppression stage. It was detected, that this processing is the main limitation and issue in the processing for passive radar on moving platforms. By mathematical and simulated analyses it was demonstrated, how this processing shows severe limitations in the clutter suppression and in the capability to detect moving targets. To address this key point, an alternative approach was suggested. This approach involves substituting the matched filter in the range compression with a reciprocal filter in order to achieve a time-invariant impulse response. It was demonstrated that this approach achieves together with a dedicated clutter cancellation stage theoretically an ideal clutter cancellation, since it allows to restore the paradigm of equivalent observations of a scene by along-track displaced receiving antennas.
Both statements and the effectiveness of the suggested approach were investigated and proven by means of measurement campaigns and real data evaluation. The remarkable results in terms of clutter suppression and target detection clearly demonstrated the enhancement of the suggested approach compared to the conventional processing.

These findings mean key points for the passive radar research community, as by knowledge of this effect and application of the suggested approach, the signal processing is drastically improved in terms of clutter suppression and target detection. In this work limitations for practical implementations were as well addressed, among which there are the re-establishing of the DPCA condition, and missing channel calibration. In order to re-establish the DPCA condition, it was suggested to use a third-party device, which acquires precise position and velocity data for motion compensation, and by this a STAP scheme was created.
The missing calibration was addressed by means of exploitation of the direct signal in different calibration techniques, and the effectiveness of the approach was investigated.
Furthermore, a technique which exploits the MV power spectrum estimation was presented, which is able to further improve the clutter suppression.
It was shown by data evaluation, that the knowledge of the transmitted signal is crucial for the processing, as a non-ideal reference signal can severely impede the performance of the processing. This is an area of future research.
Further topics that were addressed refer to the reception of so-called CCI, which is the simultaneous reception of another waveform transmitted on the same frequency as the exploited waveform, and can be regarded as a broadband noise jamming, so that the objectives of the passive radar system (target detection and imaging) are severely impeded. In this work, it was the very first time, that this effect has been shown on real data by comparing the processing results on the evaluated data before and after the suppression of the CCI.
Furthermore, a technique for range resolution improvement in PCL SAR was presented, which exploits two (or more) spatially distributed receiving platforms.
Overall, the results of this research, especially the suggested approach of cascading a reciprocal filtering stage with the DPCA stage for clutter suppression, mean a substantial improvement in terms of clutter suppression and provide important knowledge for the passive radar community.

7.2 Future Work

During this work key points and areas of further research were identified, which are important to increase the performance of passive radar on moving platforms.

Dependence on the reference signal It was demonstrated, that the RpF enables an ideal clutter suppression. However, for the RpF to work, knowledge of the reference signal is a crucial factor. If this is not known, a time-invariant impulse response can not be achieved. Instead, and as has been shown for the MF, residuals after range compression and Doppler filtering remain all over the

range-Doppler map limiting target detection. One reason that limits reference signal estimation might be due to the relative velocity of the receiver towards the transmitter itself. While transmission formats such as DAB or DVB-T are quite resistant to fading, which arises due to the movement, provided the SNR is sufficient, this might not be the case if other signals of opportunity are exploited, e.g. DVB-T2 as the carrier spacing in DVB-T2 is closer than compared to DVB-T. This can very likely lead to ICI in signals received on a moving platform. As it therefore might not always be possible to acquire a clean copy of the reference signal, further research needs to focus on an alternative method for the processing and to improve reference signal estimation.
Reference signal estimation could be improved by exploiting multiple surveillance antennas.

Digital calibration methods If the receiving system is not carefully calibrated, residuals will remain after clutter suppression. It was shown that digital calibration methods, e.g. by exploiting the direct signal, provide the possibility to overcome this limitation. However, if the direct signal (or the signal, which is used for calibration), is received from the arrays backlobe, or through RAM, the estimated phase and amplitude values for digital calibration show a random behaviour and can not be used for calibration, as the phase and amplitude of the clutter returns compensated by the estimated values differ in both receiving antennas. A possibility to improve this further might be in further improving the exploitation of the MV power spectrum estimation.

Co-channel interference As the acquired data from the air-borne measurements have shown, the simultaneous reception of signals with a different content, emitted by transmitters on the same frequency as the IO and possibly very distant to the receiver, can drastically decrease the performance of a passive radar on an air-borne platform. The simultaneous reception, i.e. the CCI, can be regarded as a wideband noise jammer, as the reference signal estimation is impeded, very likely even made impossible. For this reason the noise level can drastically increase and limit the dynamic range, which is directly resulting from the, but also results from the non-stationary impulse-response after range compression.
Effort must be put into this research area on numerous levels: the available space for the front-end, i.e. the receiving antennas might be limited if the PCL system is mounted on a ULA or a UAV. Therefore there might not be enough degrees of freedom to cancel the CCI spatially. Research effort must be steered towards an improved receiving system with the flexibility and adaptivity to receive the direct signal without CCI reception. In the same way, the focus must as well be steered towards improved signal processing methods, which refer to CCI suppression and

reference signal estimation. For this reason, there is wide field of necessary research.

Foliage penetration capability The evaluation of the data from the ground-borne trial has shown, that among the clutter returns received with the highest power are that ones, which are backscattered from forests and foliage. It was so far not possible to achieve the expected overall clutter cancellation, despite having almost ideal conditions, namely a clean copy of the reference signal, and fulfilled DPCA condition. As it is said, that frequencies in the UHF band have foliage penetration capability, the experience with this data shows, that there might be a limitation for passive radar, which could potentially be addressed to the great elevation angle. Next research steps need to focus on this, in order to detect the limitations and to improve the suppression of foliage clutter.

Range resolution The range resolution is given by the bandwidth of the transmitted signal. For improved localisation purposes and higher resolution of SAR images, the bandwidth provided by DVB-T is not sufficient. A solution could be to sample simultaneously two (or more) DVB-T channels, which are adjacent to each other. However, they need to be emitted by the same IO, otherwise coherency is not given. It might be the case, that one IO transmits two or more adjacent DVB-T channels, but this does not occur often.
A solution which might be easier to establish is the reception of the same DVB-T channel on spatially separated receivers. While it was shown in simulations, that this is a feasible method [1], in a real environment it is more difficult to fulfil the strict requirements of receiver synchronisation, coordination and flight trajectory. Therefore there is potential for further research on this topic, considering as well that constellations of low-cost light weight receivers are likely to be an appealing surveillance system solution in the near future.

Chapter 8

Appendix

8.A Matched filter: Mean value and variance evaluation

The signal transmitted signal $s[l]$ can be assumed to follow a normal distribution with zero mean and variance σ_s^2: $\mathcal{CN}(0, \sigma_s^2)$. Assuming an observation time $T_{\text{obs}} = Lf_S$, where L defines the number of samples and f_S defines the sampling frequency, the autocorrelation $c[m]$ of $s[l]$ can be defined as:

$$c[m] = \sum_{l=0}^{L-1} s[l]s^*[l+m] \tag{8.1}$$

The mean value of $c[m]$ can be calculated as:

$$E\{c[m]\} = E\{\sum_{l=0}^{L-1} s[l]s^*[l+m]\} = \sum_{l=0}^{L-1} E\{s[l]s^*[l+m]\} = L\sigma^2\delta[m] \tag{8.2}$$

The variance of $c[m]$ is given as:

$$\text{Var}\{c[m]\} = E\{|c[m]|^2\} - (E\{c[m]\})^2 \tag{8.3}$$

where

$$E\{|c[m]|^2\} = E\Big\{\Big|\sum_{l=0}^{L-1} s[l]s^*[l+m]\Big|^2\Big\} = E\Big\{\sum_{l=0}^{L-1}\sum_{p=0}^{L-1} s[l]s^*[l+m]s^*[p]s[p+m]\Big\} \tag{8.4}$$

$$= \sum_{l=0}^{L-1}\sum_{p=0}^{L-1} E\{s[l]s^*[l+m]s^*[p]s[p+m]\} \tag{8.5}$$

which can be evaluated for two cases $m = 0$ and $m \neq 0$:

$m = 0$:

$$\begin{aligned} \Rightarrow E\{|s[l]|^2|s[p]|^2\} &= E\{\left(|s_R[l]|^2 + |s_I[l]|^2\right)\left(|s_R[p]|^2 + |s_I[p]|^2\right)\} \\ &= \begin{cases} \sigma^4 & l \neq p \\ 2\sigma^4 & l = p \end{cases} = \sigma^4 + \sigma^4\delta[l-p] \end{aligned} \tag{8.6}$$

$m \neq 0$:

$$\Rightarrow E\{s[l]s^*[l+m]s^*[p]s[p+m]\} = \begin{cases} 0 & l \neq p \\ \sigma^4 & l = p \end{cases} = \sigma^4\delta[l-p] \tag{8.7}$$

This leads then to:

$$\begin{aligned} E\{|c[m]|^2\} &= \sum_{l=0}^{L-1}\sum_{p=0}^{L-1}(\sigma^4\delta[m] + \sigma^4\delta[l-p]) = L^2\sigma^4\delta[m] + \sum_{l=0}^{L-1}\sigma^4 \\ &= L^2\sigma^4\delta[m] + L\sigma^4 \end{aligned} \tag{8.8}$$

With (8.3) the variance can be estimated as:

$$\mathrm{Var}\{c[m]\} = L^2\sigma^4\delta[m] + L\sigma^4 - L^2\sigma^4\delta[m] = L\sigma^4 \tag{8.9}$$

8.B Matched filter: output power evaluation

The output power $P_C^{(0)}[l,m]$ for a particular range-Doppler bin at range index r and Doppler frequency index k after matched filtering is estimated as follows:

$$\begin{aligned}
P_C^{(0)}[l,m] = &\sum_{n}^{N}\sum_{m}^{N}\sum_{r=1}^{N_R}\sum_{p=1}^{N_R}\int_{\Phi_r}\int_{\Phi_p} E_{A,s(t)}\big\{A_r(\alpha)A_p^*(\alpha') \\
&\cdot (g_n[l-l_{\tau_r}] - g_{n-K}[l-l_{\tau_r}]) \\
&\cdot \big(g_m[l-l_{\tau_p}] - g_{m-K}[l-l_{\tau_p}]\big)^*\big\} \\
&\cdot \exp\left(2\pi j\frac{v_P}{\lambda}\cos\alpha(n-K)T\right) \\
&\cdot \exp\left(-2\pi j\frac{v_P}{\lambda}\cos\alpha'(m-K)T\right) \\
&\cdot \exp\left(-2\pi j\frac{m}{NT}nT\right)\exp\left(2\pi j\frac{m}{NT}mT\right)d\alpha d\alpha' \\
= &\sum_{n}^{N}\sum_{m}^{N}\sum_{r=1}^{N_R}\int_{\Phi_r} E_A\{|A_r(\alpha)|^2\} \\
&\cdot E_{s(t)}\left\{(g_n[l-l_{\tau_r}] - g_{n-K}[l-l_{\tau_r}])\,(g_m[l-l_{\tau_r}] - g_{m-K}[l-l_{\tau_r}])^*\right\} \\
&\cdot \exp\left(2\pi j\left(\frac{m}{NT} - \frac{v_P}{\lambda}\cos\alpha\right)(n-m)T\right)d\alpha
\end{aligned}$$

where $g_i[l] = s_i[l-iL] * h_i^{(\mathrm{MF})}[l] = \kappa\mathrm{IDFT}\{|S_i[m]|^2\}$ defines the impulse response after matched filtering of symbol i in time domain. N defines the number of symbols taken into account for coherent integration.
Let us consider the term:

$$\begin{aligned}
&E_{s(t)}\left\{(g_n[l-l_{\tau_r}] - g_{n-K}[l-l_{\tau_r}])\left(g_m[l-l_{\tau_r}] - g_{m-K[l-l_{\tau_r}]}\right)^*\right\} = \\
&= E_{s(t)}\big\{g_n[l-l_{\tau_r}]g_m^*[l-l_{\tau_r}] - g_n[l-l_{\tau_r}]g_{m-K}^*[l-l_{\tau_r}] - g_{n-K}[l-l_{\tau_r}]g_m^*[l-l_{\tau_r}] \\
&\quad + g_{n-K}[l-l_{\tau_r}]g_{m-K}^*[l-l_{\tau_r}]\big\} \\
&= E_{s(t)}\{g_n[l-l_{\tau_r}]g_m^*[l-l_{\tau_r}]\} - E_{s(t)}\{g_n[l-l_{\tau_r}]g_{m-K}^*[l-l_{\tau_r}]\} \\
&\quad - E_{s(t)}\{g_{n-K}[l-l_{\tau_r}]g_m^*[l-l_{\tau_r}]\} + E_{s(t)}\{g_{n-K}[l-l_{\tau_r}]g_{m-K}^*[l-l_{\tau_r}]\}
\end{aligned}$$

This can be evaluated in following way:

case $m = n$

$$\begin{aligned}
&= E_{s(t)}\{|g_n[l-l_{\tau_r}]|^2\} - E_{s(t)}\{g_n[l-l_{\tau_r}]\}E_{s(t)}\{g_{n-K}^*[l-l_{\tau_r}]\} \\
&\quad - E_{s(t)}\{g_{n-K}[l-l_{\tau_r}]\}E_{s(t)}\{g_n^*[l-l_{\tau_r}]\} + E_{s(t)}\{|g_{n-K}[l-l_{\tau_r}]|^2\} \\
&= 2E_{s(t)}\{|g_n[l-l_{\tau_r}]|^2\} - 2\left|E_{s(t)}\{g_n[l-l_{\tau_r}]\}\right|^2 \\
&= 2\mathrm{Var}\{g_n[l-l_{\tau_r}]\}
\end{aligned}$$

case $m = n + K$

$$
\begin{aligned}
&= E_{s(t)}\{g_n[l-l_{\tau_r}]\}E_{s(t)}\{g^*_{n+K}[l-l_{\tau_r}]\} - E_{s(t)}\{|g_n[l-l_{\tau_r}]|^2\} \\
&\quad - E_{s(t)}\{g_{n-K}[l-l_{\tau_r}]\}E_{s(t)}\{g^*_{n+K}[l-l_{\tau_r}]\} + E_{s(t)}\{g_{n-K}[l-l_{\tau_r}]g^*_n[l-l_{\tau_r}]\} \\
&= \left|E\{g_n[l-l_{\tau_r}]\}\right|^2 - E\left\{\left|g_n[l-l_{\tau_r}]\right|^2\right\} - \left|E\{g_n[l-l_{\tau_r}]\}\right|^2 + \left|E\{g_n[l-l_{\tau_r}]\}\right|^2 \\
&= -\mathrm{Var}\{g_n[l-l_{\tau_r}]\}
\end{aligned}
$$

case $m = n - K$

$$
\begin{aligned}
&= E_{s(t)}\{g_n[l-l_{\tau_r}]\}E_{s(t)}\{g^*_{n-K}[l-l_{\tau_r}]\} - E_{s(t)}\{g_n[l-l_{\tau_r}]\}E_{s(t)}\{g^*_{n-2K}[l-l_{\tau_r}]\} \\
&\quad - E_{s(t)}\{|g_{n-K}[l-l_{\tau_r}]|^2\} + E_{s(t)}\{g_{n-K}[l-l_{\tau_r}]g^*_{n-K}[l-l_{\tau_r}]\} \\
&= \left|E\{g_n[l-l_{\tau_r}]\}\right|^2 - \left|E\{g_n[l-l_{\tau_r}]\}\right|^2 - E\{|g_n[l-l_{\tau_r}]|^2\} + \left|E\{g_n[l-l_{\tau_r}]\}\right|^2 \\
&= -\mathrm{Var}\{g_n[l-l_{\tau_r}]\}
\end{aligned}
$$

All other cases

$$
\begin{aligned}
&= \left|E\{g_n[l-l_{\tau_r}]\}\right|^2 - \left|E\{g_n[l-l_{\tau_r}]\}\right|^2 - \left|E\{g_n[l-l_{\tau_r}]\}\right|^2 + \left|E\{g_n[l-l_{\tau_r}]\}\right|^2 \\
&= 0
\end{aligned}
$$

$$
\begin{aligned}
P_C^{(0)}[l,m] = &\sum_n^N \sum_m^N \sum_{r=1}^{N_R} \int_{\Phi_r} E_A\{|A_r(\alpha)|^2\} \\
&E_{s(t)}\left\{\left(g_n[l-l_{\tau_r}] - g_{n-K}[l-l_{\tau_r}]\right)\left(g_,[l-l_{\tau_r}] - g_{m-K}[l-l_{\tau_r}]\right)^*\right\} \\
&\cdot \exp\left(2\pi j\left(\frac{m}{NT} - \frac{v_P}{\lambda}\cos\alpha\right)(n-m)T\right) d\alpha \\
= &\sum_{r=1}^{N_R} \int_{\Phi_r} \sum_n^N \sigma^2_{Cr}(\alpha)\Bigg(\underbrace{2\mathrm{Var}\{g_n[l]\}}_{(I)} - \mathrm{Var}\{g_n[l]\}\exp\Big(\underbrace{2\pi j\left(\frac{m}{NT} - \frac{v_R}{\lambda}\cos\alpha\right)}_{(II)}\Big) \\
&- \mathrm{Var}\{g_n[l]\}\exp\Big(\underbrace{-2\pi j\left(\frac{m}{NT} - \frac{v_R}{\lambda}\cos\alpha\right)}_{(III)}\Big)\Bigg) d\alpha
\end{aligned}
$$

where the factors labelled with (I), (II), and (III) result from the cases $n = m$, $m = n + K$, and $m = n - K$. This can be further simplified by using $2\cos(x) =$

$\exp(jz) + \exp(-jz)$:

$$\begin{aligned}
P_C^{(0)}[l,m] =& \sum_{r=1}^{N_R} \int_{\Phi_r} \sum_{n}^{N} \sigma_{Cr}^2(\alpha) \mathrm{Var}\{g_n[l]\} \big(2 - \exp\left(2\pi j \left(\frac{m}{NT} - \frac{v_P}{\lambda}\cos\alpha\right) KT\right) \\
& - \exp\left(2\pi j \left(\frac{m}{NT} - \frac{v_P}{\lambda}\cos\alpha\right) KT\right)\big) d\alpha \\
=& N\mathrm{Var}\{g_0[l]\} \sum_{r=1}^{N_R} \int_{\Phi_r} \sigma_{Cr}^2(\alpha) \left\{2 - 2\cos\left(2\pi \left(\frac{m}{NT} - \frac{v_P}{\lambda}\cos\alpha\right) KT\right)\right\} d\alpha \\
=& 4N\mathrm{Var}\{g_0[l]\} \sum_{r=1}^{N_R} \int_{\Phi_r} \sigma_{Cr}^2(\alpha) \sin^2\left(\pi \left(\frac{m}{NT} - \frac{v_P}{\lambda}\cos\alpha\right) KT\right) d\alpha
\end{aligned}$$

or equivalently, with $KT = \frac{d}{v_P}$

$$= 4N\mathrm{Var}\{g_0[l]\} \sum_{r=1}^{N_R} \int_{\Phi_r} \sigma_{Cr}^2(\alpha) \sin^2\left(\pi \left(\frac{m}{NT} KT - \frac{d}{\lambda}\cos\alpha\right)\right) d\alpha \tag{8.10}$$

8.C Output power for the MF for omnidirectional antennas and homogeneous clutter

Assumptions:

- Omnidirectional antennas
- Homogenous clutter within each range cell

Under these assumptions, $\sigma_{Cr}^2(\alpha) = \sigma_{Cr}^2$. The angular integration interval is in the range of $\Phi_r = [0, \pi]$. Starting from (8.10), the output power $P_C^{(0)}[l, m]$ can be evaluated as:

$$\begin{aligned} P_C^{(0)} =& 4N\mathrm{Var}\{g_0[l]\} \sum_{r=1}^{N_R} \sigma_{Cr}^2 \int_0^{\pi} \sin^2\left(\pi\left(\frac{m}{NT} - \frac{v_R}{\lambda}\cos\alpha\right)\right) d\alpha \\ =& 4N\mathrm{Var}\{g_0[l]\} \sum_{r=1}^{N_R} \sigma_{Cr}^2 \int_0^{\pi} \frac{1}{2} - \frac{1}{2}\cos\left(2\pi\left(\frac{m}{NT} - \frac{v_R}{\lambda}\cos\alpha\right)\right) d\alpha \end{aligned}$$

using $A = 2\pi\frac{m}{NT}KT$ and $B = 2\pi\frac{v_R}{\lambda}KT$:

$$\begin{aligned} =& 4N\mathrm{Var}\{g_0[l]\} \sum_{r=1}^{N_R} \sigma_{Cr}^2 \left(\frac{\pi}{2} - \frac{1}{2}\int_0^{\pi} \cos\left(A - B\cos\alpha\right)\right) \\ =& 4N\mathrm{Var}\{g_0[l]\} \sum_{r=1}^{N_R} \sigma_{Cr}^2 \left(\frac{\pi}{2} - \frac{1}{2}\cos A \int_0^{\pi} \cos\left(B\cos\alpha\right) d\alpha - \frac{1}{2}\sin A \int_0^{\pi} \sin\left(B\cos\alpha\right) d\alpha\right) \\ =& 4N\mathrm{Var}\{g_0[l]\} \sum_{r}^{N_R} \sigma_{Cr}^2 \left(\frac{\pi}{2} - \frac{1}{2}\cos A \int_0^{\pi} \cos\left(B\cos\alpha\right) d\alpha\right) \end{aligned}$$

using (8.12):

$$= 4N\mathrm{Var}\{g_0[l]\} \sum_{r=1}^{N_r} \sigma_{Cr}^2 \left(\frac{\pi}{2} - \frac{\pi}{2}\cos(A) J_0(B)\right)$$

Re-substituting A and B gives:

$$P_C^{(0)}[l, m] = 2N\mathrm{Var}\{g_0[l]\}\left(\sum_{r=1}^{N_R} \sigma_{Cr}^2\right)\pi \left(1 - \cos\left(2\pi\frac{m}{NT}KT\right) J_0\left(2\pi\frac{d}{\lambda}\right)\right) \quad (8.11)$$

Bessel function:

$$
\begin{aligned}
J_\alpha(x) &= \sum_{m=0}^{\infty} \frac{(-1)^m}{m!\Gamma(m+\alpha+1)} \left(\frac{x}{2}\right)^{2m+\alpha} = \frac{1}{\pi}\int_0^\pi \exp(jx\cos\phi)d\phi \\
J_\alpha(x) &= J_\alpha(-x) \text{ for } \alpha = 2n,\ n = 0, 1, 2, \ldots \\
&\Rightarrow \int_0^\pi \cos(z\cos\phi)d\phi = \frac{1}{2}\int_0^\pi \exp(jz\cos\phi)d\phi + \frac{1}{2}\int_0^\pi \exp(-jz\cos\phi)d\phi \\
&= \int_0^\pi \exp(jz\cos\phi)d\phi \\
&= \pi J_\alpha(z),\ \text{for } \alpha = 2n,\ n = 0, 1, 2, \ldots
\end{aligned}
\tag{8.12}
$$

8.D Noise contribution

It is assumed, that as input to the correlation and processing stage two uncorrelated random noise signals (i.e. one for the leading antenna (LA), and one for the trailing antenna (TA)) $r_N^{(\mathrm{LA/TA})}$ with normal distribution $\mathcal{CN}(0, \sigma_N^2)$ are used. Furthermore, a DVB-T signal as filter $h[l]$ for the compression stage exists.
The range compressed outputs can be generally written as:

$$x_N^{(\mathrm{LA})}[l, n-K] = \sum_{m=0}^{L-1} r_{N(n-K)}^{(\mathrm{LA})}[m] h_{n-K}[l-m]$$
$$x_N^{(\mathrm{TA})}[l, n] = \sum_{m=0}^{L-1} r_{N(n-K)}^{(\mathrm{TA})}[m] h_n[l-m]$$

The output of the clutter cancellation stage is:

$$y_N[l,n] = x_N^{(\mathrm{TA})}[l,n] - x_N^{(\mathrm{LA})}[l,n-K] = \sum_{m=0}^{L-1} r_{Nn}^{(\mathrm{TA})}[m] h_n[l-m] - \sum_{m=0}^{L-1} r_{N(n-K)}^{(\mathrm{LA})}[m] h_{n-K}[l-m]$$

Applying the Doppler processing stage gives:

$$z_N[l,m] = \sum_{n}^{N} y_N[l,n] \exp(-2\pi j \frac{m}{NT} nT)$$

The output power for the noise input only can be estimated as:

$$P_N^{(0)}[l,m] = E\{|z_N[l,m]|^2\} = E\left\{ \sum_{n}^{N} \sum_{m}^{N} y_N[l,n] y_N^*[l,m] \exp(-2\pi j \frac{m}{NT}(n-m)T) \right\}$$
$$= \sum_{n}^{N} \sum_{m=0}^{N} E\{y_N[l,n] y_N^*[l,m]\} \exp(-j2\pi f_D (n-m)T)$$

where

$$
\begin{aligned}
E\{y_N[l,n]y_N^*[l,m]\} =& E\Big\{ \left(\sum_{q=0}^{L-1} r_{Nn}^{(\mathrm{TA})}[q] h_n[l-q] - \sum_{q=0}^{L-1} r_{N(n-K)}^{(\mathrm{LA})}[q] h_{n-K}[l-q] \right) \\
& \cdot \left(\sum_{p=0}^{L-1} r_{Nm}^{(\mathrm{TA})}[p] h_m[l-p] - \sum_{p=0}^{L-1} r_{N(m-K)}^{(\mathrm{LA})}[p] h_{m-K}[l-p] \right)^* \Big\} \\
=& E\left\{ \sum_{q=0}^{L-1} \sum_{p=0}^{L-1} r_{Nn}^{(\mathrm{TA})}[q] h_n[l-q] r_{Nm}^{*(\mathrm{TA})}[p] h_m^*[l-p] \right\} \\
& + E\left\{ \sum_{q=0}^{L-1} \sum_{p=0}^{L-1} r_{N(n-K)}^{(\mathrm{LA})}[q] h_{n-K}[l-q] r_{N(m-K)}^{*(\mathrm{LA})}[p] h_{m-K}^*[l-p] \right\} \\
=& \sum_{q=0}^{L-1} E\left\{ \left| r_{Nn}^{(\mathrm{TA})}[q] \right|^2 \right\} E\left\{ |h_n[l-q]|^2 \right\} \\
& + \sum_{q=0}^{L-1} E\left\{ \left| r_{N(n-K)}^{(\mathrm{LA})}[q] \right|^2 \right\} E\left\{ |h_{n-K}[l-q]|^2 \right\} \\
=& \sigma_N^2 \sum_{q=0}^{L-1} E\left\{ |h_n[l-q]|^2 \right\} + \sigma_N^2 \sum_{q=0}^{L-1} E\left\{ |h_{n-K}[l-q]|^2 \right\}
\end{aligned}
$$

Thus:

$$
\begin{aligned}
P_N^{(0)}[l,m] &= \sigma_N^2 \sum_{n}^{N} \left(\sum_{q=0}^{L-1} E\left\{ \left| h_n[l-q] \right|^2 \right\} + \sum_{q=0}^{L-1} E\left\{ |h_{n-K}[l-q]|^2 \right\} \right) \\
&= 2\sigma_N^2 \sum_{n}^{N} \sum_{q=0}^{L-1} E\left\{ |h_n[l-q]|^2 \right\} \\
&= 2\sigma_N^2 N \sum_{q=0}^{L-1} E\left\{ |h_0[l-q]|^2 \right\}
\end{aligned}
$$

The expression $E\{|h_0[l]|^2\}$ can be further evaluated considering the specific case for the MF and the RpF:

Matched filter case:

$$
\begin{aligned}
h_m[l] = \kappa s_m^*[-l] \rightarrow E\{|h_m[l]|^2\} &= E\{\kappa^2 |s_m[-l]|^2\} = \kappa^2 \sigma^2 \\
P_N^{(0)}[l,p] &= 2\sigma_N^2 N \kappa^2 \sigma^2 L
\end{aligned}
$$

Reciprocal filter case:

$$
\begin{aligned}
h_m[l] &= \kappa \mathrm{IDFT}\{S_m[p]^{-1}\} \\
&\Rightarrow \sum_{q=0}^{L-1} E\{|h_0[l-q]|^2\} = E\left\{\sum_{q=0}^{L-1} |h_0[l-q]|^2\right\} = E\left\{\frac{1}{L}\sum_{p=0}^{L-1} |H_0[p]|^2\right\} \\
&= \frac{\kappa^2}{L} E\left\{\sum_{p=0}^{L-1} |S_0[p]|^{-2}\right\} = \frac{\kappa^2}{L}\sum_{p=0}^{L-1} E\{|S_0[p]|^{-2}\} \\
&= \kappa^2 \frac{L}{\sigma^2}\frac{L}{L} \\
P_N^{(0)}[l,p] &= 2\sigma_N^2 N \frac{\kappa^2 L}{\sigma^2}
\end{aligned}
$$

The constant factor κ can be used to provide unitary noise at the output of the compression stage:

Matched filter:

$$\kappa_{\mathrm{MF}}^2 = \frac{1}{2LN\sigma_N^2\sigma^2}$$

Reciprocal filter:

$$\kappa_{\mathrm{RpF}}^2 = \frac{\sigma^2}{2LN\sigma_N^2}$$

Bibliography

[1] P. Wojaczek and D. Cristallini, "Optimal trajectories for range resolution improvement in multi-PCL SAR," *AEU - International Journal of Electronics and Communications*, vol. 73, pp. 173 – 182, 2017. [Online]. Available: http://www.sciencedirect.com/science/article/pii/S1434841117300821

[2] P. Wojaczek, F. Colone, D. Cristallini, and P. Lombardo, "to be published: Reciprocal filter-based STAP for passive radar on moving platforms," *IEEE Transactions on Aerospace and Electronic Systems*, 2018.

[3] P. Wojaczek, F. Colone, D. Cristallini, P. Lombardo, and H. Kuschel, "The application of the reciprocal filter and DPCA for GMTI in DVB-T - PCL," in *International Conference on Radar Systems (Radar 2017)*, Oct 2017, pp. 1–5.

[4] P. Wojaczek, A. Summers, and D. Cristallini, "Preliminary experimental results of STAP for passive radar on a moving platform," in *2018 22nd International Microwave and Radar Conference (MIKON)*, May 2018, pp. 589–592.

[5] P. Wojaczek and D. Cristallini, "The influence of channel errors in mobile passive radar using DVB-T illuminators of opportunity," in *19th International Radar Symposium IRS 2018*, Jun 2018.

[6] P. Wojaczek, A. Summers, D. Cristallini, I. Walterscheid, P. Lombardo, and F. Colone, "Results of airborne PCL under CCI conditions using DVB-T illuminators of opportunity," in *International Conference on Radar (Radar2018)*, Aug 2018.

[7] C. Underwood, M. Cherniakov, M. Antoniou, M. Gashinova, A. Stove, S. Hristov, G. Atkinson, H. Kuschel, P. Wojaczek, and D. Cristallini, "PASSAT: Passive imaging radar constellation for near-persistent earth observation," in *68th International Astronautical Congress (IAC)*, Sep 2017, pp. 1–11.

[8] M. Antoniou, A. G. Stove, H. Ma, H. Kuschel, D. Cristallini, P. Wojaczek, C. I. Underwood, A. Moccia, A. Renga, G. Fasano, and M. Cherniakov, "to

be published: Passive SAR satellite constellation for near-persistent earth observation: Prospective and issues," *IEEE Aerospace and Electronics Systems Magazine*, 2018.

[9] I. Walterscheid, P. Wojaczek, D. Cristallini, and A. Summers, "Challenges and first results of an airborne passive SAR experiment using a DVB-T transmitter," in *12th European Conference on Synthetic Aperture Radar (EUSAR 2018)*, Jun 2018.

[10] H. D. Griffiths and C. J. Baker, "Passive coherent location radar systems. part 1: performance prediction," *IEE Proceedings - Radar, Sonar and Navigation*, vol. 152, no. 3, pp. 153–159, June 2005.

[11] N. Willis, *Bistatic Radar*. SciTech Publishing, Inc., 2005.

[12] *Digital Video Broadcasting (DVB); Framing structure, channel coding and modulation for digital terrestrial television*, European Telecommunications Standards Institute (ETSI), 650 Route des Lucioles, F-06921 Sophia Antipolis Cedex - France, October 2015. [Online]. Available: https://www.etsi.org/deliver/etsi_en/300700_300799/300744/01.06.02_60/en_300744v010602p.pdf

[13] D. Tse and P. Viswanath, *Point-to-point communication: detection, diversity, and channel uncertainty*, 1st ed., D. Tse and P. Viswanath, Eds. Cambridge University Press, May 2005.

[14] *ETSI TR 102 401 V1.1.1 – Digital Video Broadcasting (DVB); Transmission to Handheld Terminals (DVB-H); Validation Task Force Report*, ETSI, 650 Route des Lucioles F-06921 Sophia Antipolis Cedex - FRANCE, May 2015.

[15] A. Partizian, *Airborne Pulse-Doppler Radar*, W. L. Melvin and J. A. Scheer, Eds. SciTech Publishing, Inc., 2013.

[16] D. Poullin, "Passive detection using digital broadcasters (DAB, DVB) with COFDM modulation," *IEE Proceedings - Radar, Sonar and Navigation*, vol. 152, no. 3, pp. 143–152, June 2005.

[17] C. Berthillot, A. Santori, O. Rabaste, D. Poullin, and M. Lesturgie, "BEM reference signal estimation for an airborne passive radar antenna array," *IEEE Transactions on Aerospace and Electronic Systems*, vol. 53, no. 6, pp. 2833–2845, Dec 2017.

[18] W. L. Melvin, "A STAP overview," *IEEE Aerospace and Electronics Systems Magazine*, vol. 19, no. 1, pp. 19–35, Jan 2004.

[19] W. Melvin, *Clutter Suppression Using STAP*. SciTech Publishing, Inc., 2012.

[20] R. C. DiPietro, "Extended factored space-time processing for airborne radar systems," in *[1992] Conference Record of the Twenty-Sixth Asilomar Conference on Signals, Systems Computers*, Oct 1992, pp. 425–430 vol.1.

[21] G. W. Stimson, H. D. Griffiths, C. J. Baker, and D. Adamy, *Introduction to airborne radar*. SciTech Publishing, Inc., 2014.

[22] M. A. Richards, *Doppler Processing*, M. A. Richards, J. A. Scheer, and W. A. Holm, Eds. SciTech Publishing, Inc., 2010.

[23] X. Neyt, J. Raout, M. Kubica, V. Kubica, S. Roques, M. Acheroy, and J. G. Verly, "Feasibility of STAP for passive GSM-based radar," in *2006 IEEE Conference on Radar*, April 2006, pp. 6 pp.–.

[24] J. Brown, "FM airborne passive radar," Ph.D. dissertation, University College London, 2013.

[25] J. Brown, K. Woodbridge, H. Griffiths, A. Stove, and S. Watts, "Passive bistatic radar experiments from an airborne platform," *IEEE Aerospace and Electronics Systems Magazine*, vol. 27, no. 11, pp. 50–55, November 2012.

[26] B. Dawidowicz, K. S. Kulpa, M. Malanowski, J. Misiurewicz, P. Samczynski, and M. Smolarczyk, "DPCA detection of moving targets in airborne passive radar," *IEEE Transactions on Aerospace and Electronic Systems*, vol. 48, no. 2, pp. 1347–1357, April 2012.

[27] B. Dawidowicz, P. Samczynski, M. Malanowski, J. Misiurewicz, and K. S. Kulpa, "Detection of moving targets with multichannel airborne passive radar," *IEEE Aerospace and Electronics Systems Magazine*, vol. 27, no. 11, pp. 42–49, November 2012.

[28] G. Bournaka, M. Ummenhofer, D. Cristallini, J. Palmer, and A. Summers, "Experimental study for transmitter imperfections in DVB-T based passive radar," *IEEE Transactions on Aerospace and Electronic Systems*, vol. 54, no. 3, pp. 1341–1354, June 2018.

[29] J. Palmer, M. Ummenhofer, A. Summers, G. Bournaka, S. Palumbo, and D. Cristallini, "Receiver platform motion compensation in passive radar," *IET Radar, Sonar Navigation*, vol. 11, no. 6, pp. 922–931, 2017.

[30] M. Cherniakov, *Ambiguity Function Correction in Passive Radar: DTV-T Signal*, M. Cherniakov, Ed. John Wiley & Sons, Ltd, 2008.

[31] P. Lombardo and F. Colone, *Advanced Processing Methods for Passive Radar Systems*, W. L. Melvin and J. A. Scheer, Eds. SciTech Publishing, Inc., 2012.

[32] F. Colone, D. Langellotti, and P. Lombardo, "DVB-T signal ambiguity function control for passive radars," *IEEE Transactions on Aerospace and Electronic Systems*, vol. 50, no. 1, pp. 329–347, January 2014.

[33] M. Glende, "PCL-signal-processing for sidelobe reduction in case of periodical illuminator signals," in *2006 International Radar Symposium*, May 2006, pp. 1–4.

[34] F. Colone, D. W. O'Hagan, P. Lombardo, and C. J. Baker, "A multistage processing algorithm for disturbance removal and target detection in passive bistatic radar," *IEEE Transactions on Aerospace and Electronic Systems*, vol. 45, no. 2, pp. 698–722, April 2009.

[35] G. Gassier, G. Chabriel, J. Barrère, F. Briolle, and C. Jauffret, "A unifying approach for disturbance cancellation and target detection in passive radar using OFDM," *IEEE Transactions on Signal Processing*, vol. 64, no. 22, pp. 5959–5971, Nov 2016.

[36] J. E. Palmer, H. A. Harms, S. J. Searle, and L. Davis, "DVB-T passive radar signal processing," *IEEE Transactions on Signal Processing*, vol. 61, no. 8, pp. 2116–2126, April 2013.

[37] C. Schwark and D. Cristallini, "Advanced multipath clutter cancellation in OFDM-based passive radar systems," in *2016 IEEE Radar Conference (RadarConf)*, May 2016, pp. 1–4.

[38] J. Heckenbach, H. Kuschel, J. Schell, and M. Ummenhofer, "Passive radar based control of wind turbine collision warning for air traffic PARASOL," in *2015 16th International Radar Symposium (IRS)*, June 2015, pp. 36–41.

[39] S. Searle, L. Davis, and J. Palmer, "Signal processing considerations for passive radar with a single receiver," in *2015 IEEE International Conference on Acoustics, Speech and Signal Processing (ICASSP)*, April 2015, pp. 5560–5564.

[40] J. H. G. Ender, "Space-time adaptive processing for synthetic aperture radar," *IEE Colloquium on Space-Time Adaptive Processing (Ref. No. 1998/241)*, pp. 6/1–618, 1998.

[41] U. Nickel, "On the influence of channel errors on array signal processing methods," *AEÜ - International Journal of Electronics and Communications*, vol. 47, no. 4, pp. 209–219, 1993.

[42] W. D. Wirth, "Joint application of autocalibration, superresolution and blind multipath estimation with an experimental array," *IET Signal Processing*, vol. 5, no. 4, pp. 426–432, July 2011.

[43] M. Malanowski and K. Kulpa, "Digital beamforming for passive coherent location radar," in *2008 IEEE Radar Conference*. IEEE, 2008, pp. 1–6. [Online]. Available: http://ieeexplore.ieee.org/document/4720988/

[44] B. Knoedler and R. Zemmari, "Self-calibration of a passive radar system using GSM base stations," in *2015 IEEE Radar Conference (RadarConf)*, Oct 2015, pp. 411–416.

[45] C. Gierull, "Digital channel balancing of alongtrack interferometric SAR data," Defence Research and Development Canada, Tech. Rep., 2003.

[46] J. L. Garry, C. J. Baker, and G. E. Smith, "Evaluation of direct signal suppression for passive radar," *IEEE Transactions on Geoscience and Remote Sensing*, vol. 55, no. 7, pp. 3786–3799, July 2017.

[47] Z. Zhao, X. Wan, Q. Shao, Z. Gong, and F. Cheng, "Multipath clutter rejection for digital radio mondiale-based HF passive bistatic radar with OFDM waveform," *IET Radar, Sonar Navigation*, vol. 6, no. 9, pp. 867–872, December 2012.

[48] R. Klemm, Ed., *Principles of Space-Time Adaptive Processing*, 3rd ed. The Institution of Engineering and Technology IET, 2006.

[49] J. Guerci, Ed., *Space-Time Adaptive Processing for Radar*, 1st ed. Artech House, 2003.

[50] B. D. Carlson, "Covariance matrix estimation errors and diagonal loading in adaptive arrays," *IEEE Transactions on Aerospace and Electronic Systems*, vol. 24, no. 4, pp. 397–401, July 1988.

[51] J. Ward, "Space-Time Adaptive Processing for Airborne Radar," Lincoln Laboratory, Massachusetts Institute of Technology, Technical report, 1994.

[52] W. C. Barott and B. Himed, "Cochannel interference in ATSC passive radar," in *2015 IEEE Radar Conference*, May 2015, pp. 1270–1275.

[53] *ETSI EN 302 755 V1.4.1 – Digital Video Broadcasting (DVB); Frame structure channel coding and modulation for a second generation digital terrestrial television broadcasting system (DVB-T2)*, ETSI, 650 Route des Lucioles F-06921 Sophia Antipolis Cedex - FRANCE, July 2015.

[54] P. Frölind, A. Gustavsson, A. Haglund, R. Ragnarsson, and L. M. H. Ulander, "Analysis of a ground target deployment in an airborne passive SAR experiment," in *2017 IEEE Radar Conference (RadarConf)*, May 2017, pp. 0273–0278.

[55] D. Gromek, K. Kulpa, and P. Samczyński, "Experimental results of passive SAR imaging using DVB-T illuminators of opportunity," *IEEE Geoscience and Remote Sensing Letters*, vol. 13, no. 8, pp. 1124–1128, Aug 2016.

[56] M. Graziano and M. D'Errico, "Novel constellation design method for spaceborne/airborne bistatic SAR systems," *IEEE Transactions on Aerospace and Electronic Systems,*, vol. 50, no. 3, pp. 2082–2095, July 2014.

[57] D. Cristallini, D. Pastina, and P. Lombardo, "Exploiting MIMO SAR potentialities with efficient cross-track constellation configurations for improved range resolution," *IEEE Transactions on Geoscience and Remote Sensing*, vol. 49, no. 1, pp. 38–52, Jan 2011.

[58] A. Liu, G. Liao, Q. Xu, and L. Ma, "An improved array-error estimation method for constellation SAR systems," *IEEE Geoscience and Remote Sensing Letters,*, vol. 9, no. 1, pp. 90–94, Jan 2012.

[59] D. Cristallini, P. Wojaczek, and M. Ummenhofer, "Range resolution improvement for multiple PCL radar systems on moving platforms," in *2015 IEEE Radar Conference*, Oct 2015, pp. 394–399.

[60] I. Walterscheid, J. Klare, A. R. Brenner, J. H. G. Ender, and O. Loffeld, "Challenges of a bistatic spaceborne/airborne SAR experiment," in *Proc. EUSAR 2006*, 2006.

[61] R. Bamler and P. Hartl, "Synthetic aperture radar interferometry," *Inverse Problems*, vol. 14, no. 4, pp. R1–R54, 1998.

[62] C. Prati and F. Rocca, "Improving slant-range resolution with multiple SAR surveys," *IEEE Transactions on Aerospace and Electronic Systems*, vol. 29, no. 1, pp. 135–143, Jan 1993.

[63] S. Guillaso, A. Reigber, L. Ferro-Famil, and E. Pottier, "Range resolution improvement of airborne SAR images," *IEEE Geoscience and Remote Sensing Letters*, vol. 3, no. 1, pp. 135–139, Jan 2006.

[64] W. L. Melvin and J. A. Scheer, Eds., *Principles of Modern Radar: Advanced Techniques*. SciTech Publishing, Inc., 2012.

Acronyms

ADS–B Automatic Dependent Surveillance – Broadcast.

DVB-S Digital Video Broadcasting Satellite.

DVB-T2 Digital Video Broadcasting – Second Generation Terrestrial.

DVB-T Digital Video Broadcasting – Terrestrial.

ADC Analog-to-digital Converter.

AF Ambiguity Function.

AIS Automatic Identification System.

ATSC Advanced Television Standards Committee (System A).

AWGN Additive White Gaussian Noise.

BER Bit Error Rate.

BPSK Binary Phase-shift Keying.

CCI Co-channel Interference.

CPC Continual Pilot Carriers.

CPI Coherent Processing Interval.

CTF Channel Transfer Function.

CW Continuous Waveform.

DAB Digital Audio Broadcasting.

DFT Discrete Fourier Transform.

DLC Delay Line Canceler.

DPCA Displaced Phase-Center Antenna.

DSI Direct Signal Interference.

DTT Digital Terrestrial Television.

DVB Digital Video Broadcasting.

ECA Extensive Cancellation Algorithm.

ECA-C Extensive Cancellation Algorithm By Carrier.

ECA-CD Extensive Cancellation Algorithm By Carrier And Doppler Shift.

FFI Norwegian Defence Research Establishment – *Forsvarets forskningsinstitutt*.

FFT Fast Fourier Transform.

FM Frequency Modulation.

GSM Global System For Mobile Communications.

ICI Intercarrier Interference.

ICM Internal Clutter Motion.

IDFT Inverse Discrete Fourier Transform.

IF Intermediate Frequency.

IFFT Inverse Fast Fourier Transform.

IO Illuminator Of Opportunity.

ISI Intersymbol Interference.

LA Leading Antenna.

LOS Line Of Sight.

LTE Long-Term Evolution.

MF Matched Filter.

MFN Multi-frequency Network.

MTI Moving Target Indication.

OFDM Orthogonal Frequency-division Multiplexing.

PCL Passive Coherent Location.

PRBS Pseudorandom Binary Sequency.

PRF Pulse Repition Frequency.

PRI Pulse Repition Interval.

PSLR Peak-to-sidelobe Ratio.

PSR Passive Radar And Anti-Jamming Techniques.

QAM Quadrature Amplitude Modulation.

QPSK Quadrature Phase-Shift Keying.

RAM Radiation-absorbent Material.

RF Radio Frequency.

RpF Reciprocal Filter.

RX Receiver.

SAR Synthetic-aperture Radar.

SCR Single Canceller Response.

SFN Single Frequency Network.

SNR Signal-to-noise Ratio.

SPC Scattered Pilot Carriers.

STAP Space-time Adaptive Processing.

TA Trailing Antenna.

TX Transmitter.

UHF Ultra High Frequency.